Recent Advances in the Measurement of Rare-Earth Metal Transition Probabilities Using Laser-Induced Plasmas

By

Russell Allan Putnam

A Thesis
Submitted to the Faculty of Graduate Studies
through the **Department of Physics**
in Partial Fulfillment of the Requirements for
the Degree of **Master of Science**
at the University of Windsor

Windsor, Ontario, Canada

2014

Recent Advances in the Measurement of Rare-Earth Metal Transition Probabilities Using Laser-Induced Plasmas

By

Russell Allan Putnam

APPROVED BY:

_____

Dr. I. Samson
Department of Earth and Environmental Sciences

_____

Dr. W. Kedzierski
Department of Physics

_____

Dr. S. Rehse, Advisor
Department of Physics

December 3, 2014

DECLARATION OF ORIGINALITY

I hereby certify that I am the sole author of this thesis and that no part of this thesis has been published or submitted for publication.

I certify that, to the best of my knowledge, my thesis does not infringe upon anyone's copyright nor violate any proprietary rights and that any ideas, techniques, quotations, or any other material from the work of other people included in my thesis, published or otherwise, are fully acknowledged in accordance with the standard referencing practices. Furthermore, to the extent that I have included copyrighted material that surpasses the bounds of fair dealing within the meaning of the Canada Copyright Act, I certify that I have obtained a written permission from the copyright owner(s) to include such material(s) in my thesis and have included copies of such copyright clearances to my appendix.

I declare that this is a true copy of my thesis, including any final revisions, as approved by my thesis committee and the Graduate Studies office, and that this thesis has not been submitted for a higher degree to any other University or Institution.

ABSTRACT

Laser-induced plasmas are easy to produce high-temperature sources (~50,000 K) of highly-excited atoms and ions for use in atomic spectroscopy experiments. Emission from the plasma, when dispersed in a high-resolution échelle spectrometer, can be used to measure the relative intensity of all emission lines from hundreds of thermally-populated energy levels. Our recent work has focused on measuring the relative intensities of emission lines from neutral, singly-ionized, and doubly-ionized species of rare-earth metals due to their significant importance to astronomers and astrophysicists for their over-abundances in "chemically peculiar" and galactic halo stars. Experimental parameters have been extensively studied to characterize plasma emission for these species at various observation times after the laser pulse, at various background pressures, various laser pulse energies, and various target compositions. Recent work has consisted of incorporating an optical parametric oscillator to resonantly excite specific energy levels within the plasma, increasing emission line intensity and eliminating line blending.

ACKNOWLEDGEMENTS

Firstly, I would like to thank my advisor, Dr. Steven Rehse. He has been a tremendous help throughout my time as an undergraduate and graduate student. He has spent countless hours teaching me, guiding me, and answering all my questions whenever I asked. For all of this, I am very grateful.

I would also like to thank my laboratory mates for their help and encouragement (Derek G., Andrew D., Dan T., Dylan M., Anthony P., and Vlora R.) who have worked with me at various times throughout my research at the University of Windsor. As well, I would like to thank my friends throughout my undergraduate and graduate studies, Andrew, Geoff, Jon, and many others.

And lastly, my family and girlfriend, Tina, for their unconditional support, patience, and encouragement.

TABLE OF CONTENTS

LIST OF TABLES

LIST OF FIGURES

LIST OF APPENDICES

CHAPTER 1: Introduction

1.1 Motivation

The focus of this work is to make atomic measurements on atoms and ions produced in a laser-induced plasma. This work is motivated by an astrophysics application where there is currently a lack of accurate atomic data. This atomic data, in particular accurate experimentally-measured lanthanide (rare-earth metal) transition probabilities, are frequently requested by some astrophysicists [1]. The lanthanides are observed in the spectra from galactic halo and "chemically peculiar" (CP) [2, 3] stars and accurate transition probabilities are required to determine the lanthanide abundances in those stars.

Accurately determining lanthanide abundances in these stars will help astrophysicists better understand the supernovae nucleosynthesis process in which elements heavier than iron are formed. In some cases, over-abundances of lanthanides relative to iron are observed and accurate atomic data is required to correct discrepancies in the calculated abundances [3, 4]. Lanthanides are of such importance that a new database was created for reporting lanthanide atomic data such as transition probabilities (Database on Rare-earths at Mons University, DREAM). This work focuses on four lanthanides: neodymium (Nd), gadolinium (Gd), samarium (Sm), and praseodymium (Pr).

1.1.1 Nucleosynthesis

There are multiple types of nucleosynthesis. Galactic nucleosynthesis is the process in which elements heavier than hydrogen are formed in celestial bodies. This work focuses on atoms that are formed in one specific type of galactic nucleosynthesis, supernovae nucleosynthesis. Supernovae nucleosynthesis is the process in which elements heavier than iron are formed during the death of stars. These elements can only be formed in supernovae due to the amount of energy required for their production [5]. In supernovae nucleosynthesis there are two process that can occur for production of elements heavier than iron, the s(low)-process and r(apid)-process. The r-process and s-process occur by neutron capture

and differ by the neutron capture rate as their name implies. The r-process results from a high rate of neutron capture and forms a very neutron rich isotope that will decay via beta-minus decay to a stable isotope with the same atomic weight. This r-process is rapid due to the neutron capture occurring at a higher rate than the beta decay. Multiple neutrons will be absorbed before beta decay occurs and thus the formation of new atoms does not need to follow any specific pattern for production of heavy elements. This leads into the discussion of the s-process, where the neutron capture occurs at a much slower rate than the beta-minus decay and thus only one neutron is captured before the beta-minus decay occurs (if the beta-minus decay will result in a stable isotope). In the s-process, the production of heavy elements must follow a specific path due to beta-minus decay occurring before secondary neutron capture. The lanthanide elements provide a convenient test system because they form a contiguous series of highly similar heavy (high-Z) elements. By accurately measuring the stellar abundances (reflective of what was formed in the supernovae nucleosynthesis) of many such heavy elements these processes can be better understood and modeled.

1.2 Laboratory Astrophysics

High-resolution absorption spectra from stars are becoming increasingly available [4]. In the absorption spectra of certain stars, absorption lines from lanthanide ions are observed. In order to determine the abundance of these lanthanides in the stellar photosphere, the transition probabilities of the observed lines are required as the “strength” of the observed line is dependent on the abundance (amount present in the star) and transition probability. In order to experimentally determine an accurate transition probability a branching fraction (or “branching ratio”) and an excited state lifetime are needed. Of course, because the atoms present in the stars are identical to the atoms in the laboratory on Earth, branching fractions and radiative lifetime measurements acquired in a laboratory experiment can be used to calculate absolute transition probabilities which can then be applied to interpret absorption spectra from stars to accurately determine the observed lanthanide abundances.

1.2.1 Branching Fractions

In order to calculate a transition probability a branching fraction is required. A branching fraction indicates the probability for an atom in an excited state to decay via a specific spontaneous emission decay route (one transition) relative to the probability of decaying along all possible decay routes (all allowed transitions.) The sum of all the branching fractions for all the allowed transitions out of an excited state must equal one, as the total probability for decay is one. All transitions do not have equal probability of occurring and thus branching fraction measurements are required in order to determine the "strength" of the various transitions out of an excited state. Put another way, the relative branching fractions determine the number of atoms that will decay via one transition or another in a collection of atoms. Figure 1 shows an energy level diagram for singly-ionized neodymium showing the eight allowed transitions to lower energy levels from the 6p $^6K_{9/2}$ upper energy level at 23229.99 cm^{-1}. This particular level was studied extensively in this thesis. Each of the eight transitions has some probability of occurring determined by the transition branching fractions. Thus for each upper energy level, all branching fractions must be reported. This implies that to make such measurements, all transitions must be observed. Equation 1.1 shows how a branching fraction is defined.

$$\beta_{ji} = \frac{A_{ji}}{\sum A_{ji}} \tag{1.1}$$

A branching fraction for a transition from an upper state *j* to a lower state *i*, β_{ji}, is equal to the Einstein *A*-coefficient for spontaneous emission of that transition, A_{ji}, divided by the sum of all Einstein *A*-coefficients for transitions exiting the upper energy level and ending in different lower levels, *i*. The Einstein *A*-coefficient, A_{ji}, represents the probability per unit time (s^{-1}) that an atom in state *j* will decay spontaneously to state *i*. Equation 1.2 shows how a branching fraction may be determined.

$$\beta_{ji} = \frac{I_{ji}}{\sum I_{ji}} \tag{1.2}$$

The branching fraction β_{ji} of the transition from state *j* to state *i* is also equal to the transition's observed relative emission intensity, I_{ji}, divided by the sum of all

observed relative emission intensities from all transitions exiting the upper energy level j and ending in different lower levels i. In this thesis, by measuring all the I_{ji} from an excited state, I will directly determine the branching fractions β_{ji} of all decay transitions starting in that upper state j. Equation 1.3 shows how the radiative lifetime of the upper state j, which is denoted τ_j, is related to the Einstein A-coefficients for spontaneous emission.

$$\tau_j^{-1} = \sum_i A_{ji} \tag{1.3}$$

A radiative lifetime can be thought of as the time an atom will remain in a given upper energy level before it decays. More accurately, it is the inverse of the sum of the Einstein A-coefficients (which are transition rates) for all the transitions out of an upper energy level. Combing equations 1.1 and 1.3 then gives us Equation 1.4.

$$\frac{\beta_{ji}}{\tau_j} = A_{ji} \tag{1.4}$$

Therefore, an experimentally determined transition probability for spontaneous emission (Einstein A coefficient) can be determined by dividing an experimentally determined branching fraction with an experimentally measured

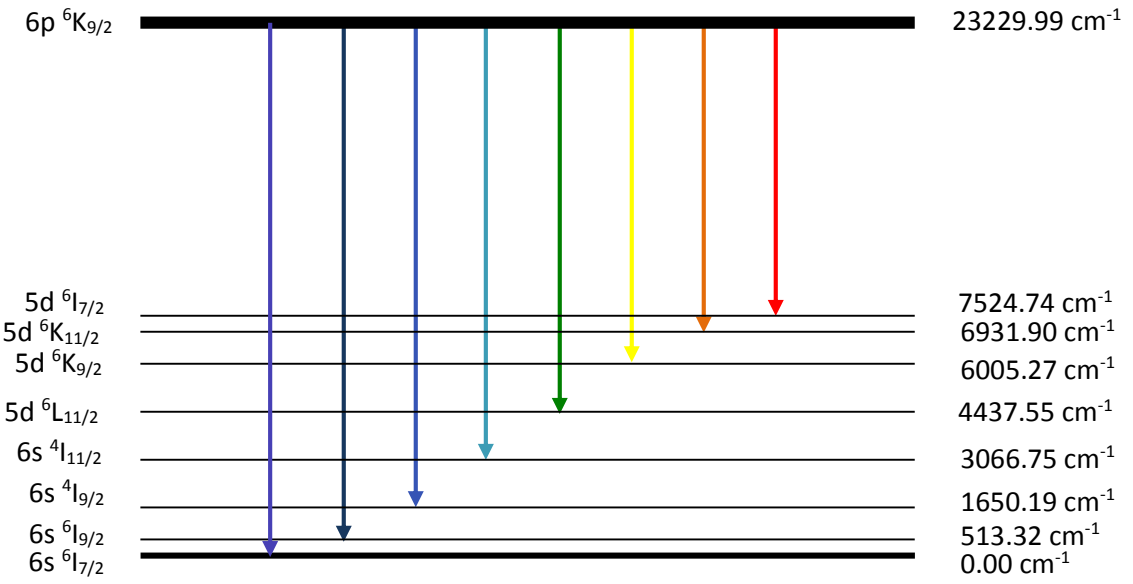

Figure 1.1 Singly-ionized neodymium energy level diagram showing the eight lower energy levels which have allowed spontaneous emission transitions from the 6p $^6K_{9/2}$ upper energy level at 23229.99 cm^{-1}.

upper state lifetime. In this thesis, only the branching fractions β_{ji} will be measured. We will utilize the experimental lifetimes of others to calculate transition probabilities. In some studies the product g_jA_{ji} or just gA is reported, where g_j is the multiplicity, or number of degenerate energy levels, of the upper state j. In other studies, and of more use to astronomers, an oscillator strength (gf value or more typically log gf) is reported. An oscillator strength is the number of classical oscillations equivalent to one real atom for a given transition.

$$A_{ji} = \frac{2\pi e^2}{m_e c \varepsilon_0 \lambda^2} \frac{g_i}{g_j} f_{ji} \tag{1.5}$$

Equation 1.5 shows how an Einstein A-coefficient is defined in terms of the oscillator strength, f_{ji}, the upper and lower energy levels degeneracies, g_j and g_i, the transition wavelength, λ, the mass of the electron, m_e, the speed of light, c, the electron charge e, and the permittivity of free space, ε_0.

1.2.2 Experimental Determinations of Branching Fractions

Laboratory astrophysics measurements, specifically branching fraction measurements, are determined by a number of different methods such as: laser-induced plasmas, fast ion-beam laser experiments, and hollow cathode discharge lamps combined with Fourier Transform Spectroscopy (FTS) [4]. Laser-induced plasmas are produced by a high-energy pulsed laser that excites atoms and ions from a solid target. The excited atoms and ions in the plasma will decay to a lower energy state releasing photons and the resulting elemental emission is observed. This allows for quick and easy production of highly-excited atoms and ions and thus allows for transition probability measurements on hundreds of excited states and various ionization species all at once. In the fast ion-beam method, ions are created by an ion-vapour source and accelerated towards a perpendicular or co-linear tunable laser beam. The laser frequency is adjusted to populate a specific upper energy level and emission is observed from the chosen energy level. This allows for measurement of one energy level at a time and only allows for measurement of energy levels within the tunable laser's frequency range. Hollow cathode discharge lamps measurements are conducted by creating a large voltage across the cathode and anode. Atoms are ionized and accelerated towards the cathode. The ions impact the cathode and cause

ejection and ionization of ions from the cathode material. These ions (from the cathode) become excited and decay to lower energy states. The resulting ion emission, combined with interferometry and FTS, allows the determination of transition probabilities. A list of previous work is included and discussed in more detail in Chapter 6.

The use of laser-induced plasmas for this purpose has been proposed as a relatively new technique for transition probability measurements due to its ability (with limited sample preparation) to quickly and easily highly-excite atoms and ions and thus observe branching fractions on various species all with no change to the experimental setup. With only the change of a solid lanthanide target measurements on multiple lanthanides (including various ionization states, neutral - I, singly-ionized - II, and doubly-ionized - III) can be completed in a time span of a few minutes.

1.3 Laser-Induced Breakdown Spectroscopy

This work will entail the use of laser-induced breakdown spectroscopy (LIBS) to make accurate atomic measurements. LIBS involves the focusing of a high-energy pulsed laser onto a target, which creates a weakly-ionized plasma to act as a source of highly-excited atoms and ions. LIBS rapid production of highly-excited atoms and ions allows for measurement and determination of atomic data. LIBS has just begun to be used for atomic measurements [6]. One of the benefits to using LIBS for atomic measurements is the ease of production of highly-excited atoms which in other techniques is not possible due to the energy required to populate a highly-excited state. A thorough description of LIBS is provided in Chapter 2.

LIBS can also be used to make radiative lifetime measurements. An experiment for radiative lifetime measurements was initiated during the atomic measurement work conducted in this thesis but will not be reported due to only proof-of-concept work being completed (this will be a future student's project). To make a radiative lifetime measurement with a laser-induced plasma the light from the plasma is collimated and sent through a beam splitter. The two collimated beams of light from the plasma pass through narrow bandpass filters in which only photons from one specific transition may pass through each filter. For a radiative lifetime

measurement the filters are chosen to only allow light from a transition entering and a transition exiting an upper energy level to pass through. Using single-photon counting devices, photons resulting from the transition entering and exiting the level can be observed. Using fast-timing electronics and pulse analysis, the time between start and stop pulses (photon observations) are measured and the experiment is repeated to determine a radiative lifetime of an excited state under investigation.

1.4 Scope of Thesis

The scope of this work is to improve an existing experimental apparatus and analysis technique to increase the accuracy of our transition probability measurements as well as making new measurements of neutral and doubly-ionized species by optimizing experimental parameters.

In Chapter 2 I discuss laser-induced breakdown spectroscopy theory to provide a better understanding of how atomic measurements may be made on a laser-induced plasma. I will also describe several relevant effects that it is necessary to understand when using a laser-induced plasma for such atomic measurements. In Chapter 3 I discuss the experimental setup and the new components I designed and implemented to improve light collection. In Chapter 4 I discuss experimental parameter optimization to increase observed emission from specific species in the plasma, which results in an improved measurement of emission lines and the observation of previously unobservable emission lines. In Chapter 5 I discuss the data and error analysis of the spectroscopic data for measurement of transition probabilities. In Chapter 6 I report and discuss transition probability measurements made on our laser-induced plasmas. In Chapter 7 I introduce and discuss a new method, laser-induced breakdown spectroscopy – laser-induced fluorescence (LIBS-LIF), for atomic measurements to minimize and alleviate certain problems associated with atomic measurements on laser-induced plasmas. In Chapter 8 I summarize the work presented in this thesis and discuss future work. In Appendix A I list programs used for automated data analysis.

References

[1] Sneden, C., Lawler, J. E., & Cowan, J. J. (2002). Galactic cosmochronometry from radioactive elements in the spectra of very old metal-poor stars. *Physica Scripta*, *2002*(T100), 15.

[2] Wahlgren, G. M. (2002). The lanthanide elements in stellar and laboratory spectra. *Physica Scripta*, *2002*(T100), 22.

[3] Lawler, J. E., Bilty, K. A., & Den Hartog, E. A. (2011). Atomic transition probabilities of Gd I. *Journal of Physics B: Atomic, Molecular and Optical Physics*, *44*(9), 095001.

[4] Biémont, É. (2005). Recent advances and difficulties in oscillator strength determination for rare-earth elements and ions. *Physica Scripta*, *2005*(T119), 55.

[5] Carroll, B. W., & Ostlie, D. A. An introduction to modern astrophysics, 2007.

[6] Xu, H. L., Persson, A., Svanberg, S., Blagoev, K., Malcheva, G., Pentchev, V., ... & Mayo, R. (2004). Radiative lifetime and transition probabilities in Cd I and Cd II. *Physical Review A*, *70*(4), 042508.

CHAPTER 2: Laser-Induced Breakdown Spectroscopy

Laser-induced breakdown spectroscopy (LIBS) is a time-resolved spectroscopy of optical emission from a weakly-ionized (~10%) plasma generated by a high-energy pulsed laser. LIBS can be used as a qualitative and quantitative analysis technique on a variety of substrates (LIBS works equally as well on solids, liquids, and gases) as has been described in great detail in a number of recent authoritative books [1-4]. LIBS can be used for a wide variety of applications ranging from bacterial discrimination to explosive identification by measuring the atomic composition of the material [5, 6]. This chapter will give an introduction to LIBS and discuss some of the key concepts in laser-induced plasma spectroscopy.

2.1 Plasma Production (Nanosecond Laser Regime)

When a high-energy nanosecond laser pulse is incident on a target, it acts to vaporize and atomize the target, followed by ionization and excitation of the created cloud of atoms. I used a Nd:YAG laser with a pulse duration of 10 ns and a wavelength of 1064 nm. Any wavelength could be used for LIBS as long as the wavelength is sufficiently absorbed by the target [1]. A pulsed laser is ideal for LIBS as it provides sufficient energy fluence to cause the breakdown [1] (atomization and liberation of electrons) of the target material. I will only discuss the nanosecond regime for plasma production since it was the only plasma production method used for my thesis (other regimes that exist are femtosecond and picosecond laser plasma production).

The high-energy fluence of the laser pulse causes melting and vaporization of the target material on a picosecond time scale. A small portion of a target material is ablated, which results in a crater a few microns deep and about a hundred microns in diameter (depending on the focused size of the laser pulse). The ablated material forms a cloud of atoms/molecules/fragments above the surface of the target. The cloud of atoms absorbs the remaining energy of the laser pulse through inverse bremsstrahlung and multiple photon excitations resulting in the rapid excitation and ionization of the atoms, creating a dense, but weakly-ionized plasma. Figure 2.1

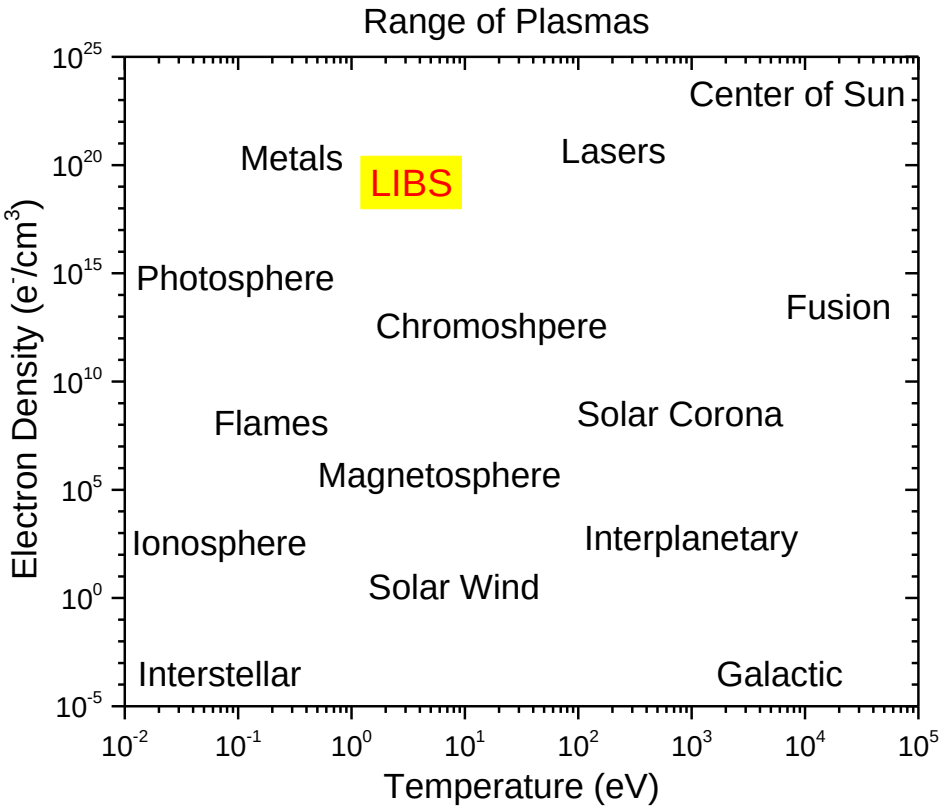

Figure 2.1 Plasma regimes characterized by electron density and temperature with laser-induced plasmas near the mid-range of temperature and high-end of electron density in comparison to other the other types of plasmas seen in this figure [7].

shows the parameters for laser-induced plasmas compared to other common plasmas. Figure 2.2 schematically shows the laser-induced plasma formation process just described. The time from incident laser pulse to ionization of atoms is tens of nanoseconds and the temperature of the plasma at formation can exceed 50,000 K [2]. The plasma is elongated in the direction of the incident laser pulse due to the absorption of the laser pulse as shown in Figure 2.3 which is a photograph taken in our lab. The vaporized atoms travel outwards at supersonic speeds, which results in the formation of a shockwave. Over the first few hundred nanoseconds of plasma evolution, continuum emission dominates and no useful information can be obtained from the light emitted from the plasma. As the plasma cools, electrons recombine with ions and the atoms and ions decay to lower energy states. Ionized and then neutral emission from the ions and atoms in the plasma may be observed over the following

tens of microseconds. The plasma consists of free electrons, ions, atoms, and molecules in varying ratios depending on the time evolution of the plasma to be discussed in Section 2.2.

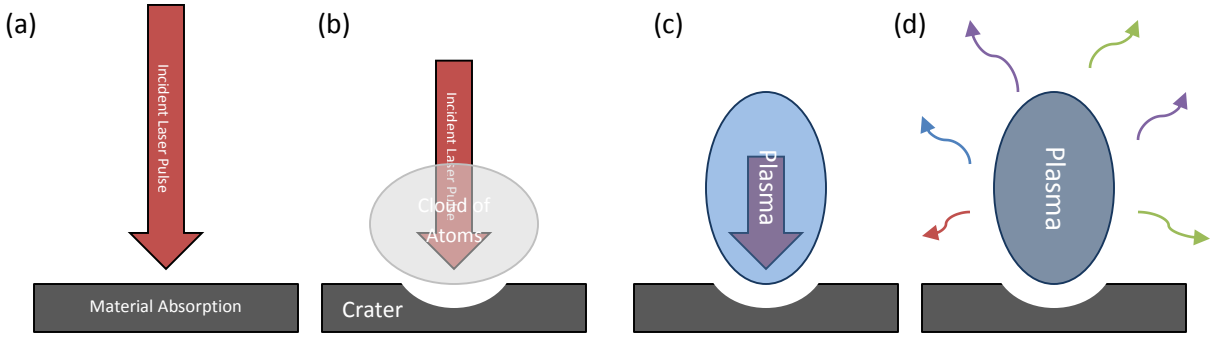

Figure 2.2 A LIBS plasma production schematic. (a) Shows the laser pulse incident on a target material. The target will absorb the laser energy causing melting, heating and vaporization. (b) The incident laser pulse has now ablated a small portion of the target material and produced a cloud of atoms above the target that will absorb the remaining energy of the laser pulse. (c) The plasma has now formed, it is very hot and dense, and the final energy of the laser pulse is absorbed. A shockwave and continuum emission is produced at formation of the plasma. (d) After a few hundred nanoseconds continuum emission has decreased and element-specific atomic and ionic emission is observed [1].

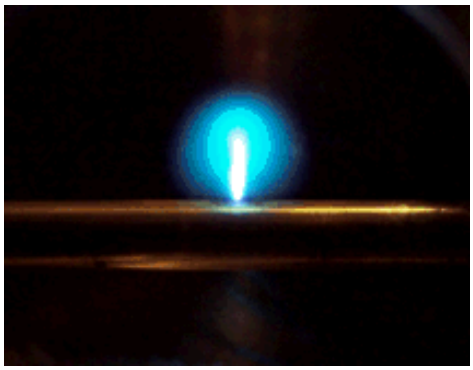

Figure 2.3 A laser-induced plasma on a metal target inside a vacuum chamber displaying the elongation of the plasma in the direction of the incident laser pulse (the laser was incident from above in this picture orientation).

2.2 Plasma Evolution

The plasma is very hot and very dense at its formation and continuum emission dominates for the first few hundred nanoseconds, as previously mentioned. This results in large background emission and no useful information is observed from the plasma. As the plasma begins to cool, background emission decreases and ionic emission can be observed. The ionization states observed as the plasma evolves can be estimated using the Saha-Boltzmann equation (Equation 2.1). This equation characterizes the fraction of atoms in each ionization state as a function of temperature, T, and electron density, N_e, both of which evolve in time. $N_{I,k}$ and $N_{A,j}$ are the number of atoms per unit volume in the kth and jth energy levels in corresponding ionization states I and A, m_e is the mass of an electron, k_B is the Boltzmann constant, h is Planck's constant, $g_{I,k}$ and $g_{A,j}$ are the multiplicity for the kth and jth energy levels in the I and A ionization states, χ_Z is the ionization potential, and E_k and E_j are the energies of the kth and jth levels. A constant N_e of 10^{24} cm^{-3} was used to produce a graph that approximated the fraction of atoms in a given ionization state as a function of temperature for the first few ionization states of neodymium (Figure 2.4). This calculation allowed for comparison of our plasma temperature and observed ionization states in various spectra. Changing our observation time after plasma formation allowed us to observe different plasma temperatures and thus compare the observed spectra to Figure 2.4.

$$\frac{N_{I,k}}{N_{A,j}} = \frac{1}{N_e}\frac{2(2\pi m_e k_B T)^{3/2}}{h^3}\frac{g_{I,k}}{g_{A,j}} exp\left[\frac{-(\chi_Z + E_k - E_j)}{k_B T}\right] \qquad (2.1)$$

Figure 2.5 shows a Nd III, Nd II, and Nd I LIBS spectrum obtained at various plasma temperatures by varying the observation time of the plasma. In our lanthanide targets, from 0.5 to 1 microsecond after the laser pulse doubly-ionized emission (e.g. from Nd III) is observed from the plasma with an average plasma temperature of approximately 15,000 K. Looking at Figure 2.4 and Figure 2.5, the black spectrum in Figure 2.5 corresponds to what is seen in Figure 2.4 for the fraction of atoms in the singly and doubly-ionized states at a temperature of approximately 15,000 K. As the plasma cools, singly-ionized emission (from Nd II) is observed to

dominate from 1 to 3 microseconds with a plasma temperature of approximately 12,000 K. At 12,000 K in Figure 2.4 we see singly-ionized species dominate with minimal doubly-ionized and neutral atoms present. This again correlates with what is observed in the red spectrum in Figure 2.5 with the majority of observed emission resulting from Nd II. The plasma continues to cool and electrons recombine with ions to form neutral atoms and neutral emission (from Nd I) increases in the plasma from 3 to 13 microseconds with a plasma temperature of approximately 8,000 K at 3 microseconds. This is again seen in Figure 2.5 in the blue spectrum that contains some Nd II emission and mostly Nd I emission by observing the plasma until 13 microseconds. This correlates with the calculation in Figure 2.4 since 8,000 K is approximately the crossover point at which Nd I becomes the dominant species. At 13 microseconds Nd I must dominate since the plasma is observed to be approximately 4,000 K.

Beyond 13 microseconds emission from the plasma becomes unobservable with our atomic measurement setup. Molecular emission would be observed in most LIBS plasmas from approximately 7 microseconds onwards [2], but due to our plasma consisting of only one lanthanide species and argon gas no molecular emission was observed. An argon gas environment is used for plasma formation to increase ionic and atomic emission by creating a hotter and denser plasma in comparison to air. The increase in emission also results in an increased single-to-noise ratio when ablating targets in argon [2].

2.3 Factors Effecting Plasma Emission

There are key factors that need to be considered when atomic measurements are to be made in a laser-induced plasma. In order to determine the population of atoms in a given energy level the plasma needs to be in local thermodynamic equilibrium (LTE). LTE is an approximation to true thermodynamic equilibrium and allows the plasma to be characterized by a single value of electron density (N_e) and electron temperature (T_e). Knowing these two critical parameters allows one to be able to calculate the velocity distribution of species, ionization populations, and

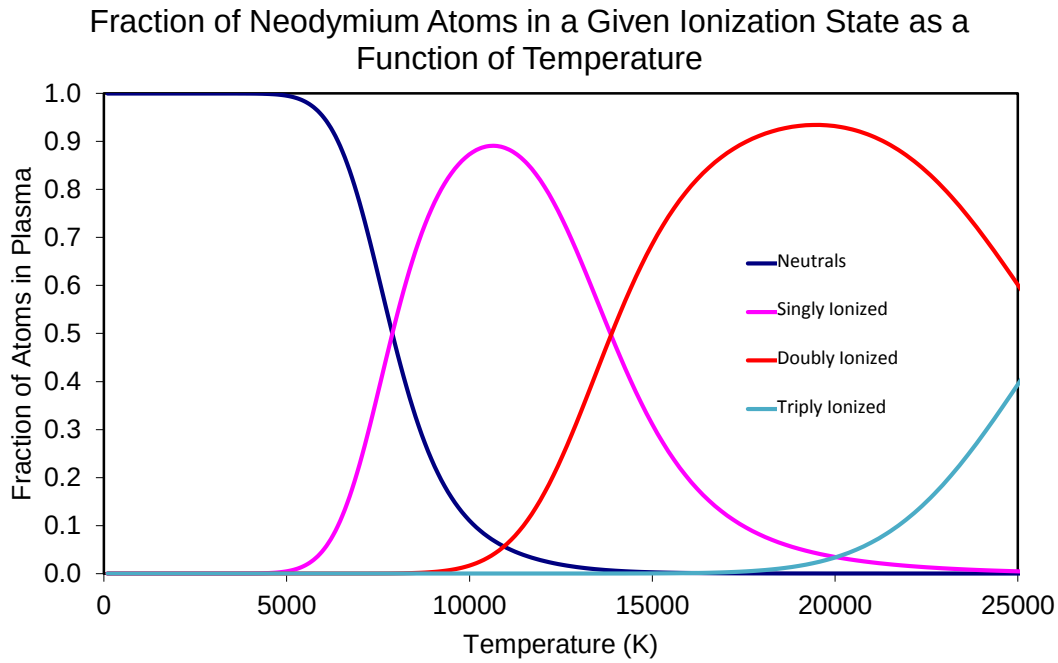

Figure 2.4 Using the Saha-Boltzmann equation one can see the relative number of neodymium atoms and ions at different plasma temperatures, which agreed with our observed spectra at various delay times after plasma production. Changing the delay time allowed us to observe different temperatures and thus what ionization state(s) were present in the spectrum. This graph also demonstrates why it is most effective to only observe one ionization state at a time and thus optimize parameters for only that ionization state. The temperature at which certain ionization states are present depends on the electron density of the plasma as well as the ionization energies of the states as seen in Equation 2.1. This graph was calculated using neodymium atomic values and an N_e of 10^{24} cm^{-3}.

radiation distributions in the plasma [1]. The electron temperature and density also determine Stark effects (such as the broadening or shifting of emission lines), optical thinness, and collisional de-excitation [1], which could affect the measured branching fractions. Since the N_e and T_e of the plasma are evolving with time, the plasma needs to be observed only in conditions of LTE to make atomic measurements.

Emission lines can be Stark-shifted and/or Stark-broadened if the electron density is large. A large electron density results in strong local electric fields and the shifting and splitting of observed energy levels. With a very large electron density broad emission lines are observed that decrease the accuracy of results as well as

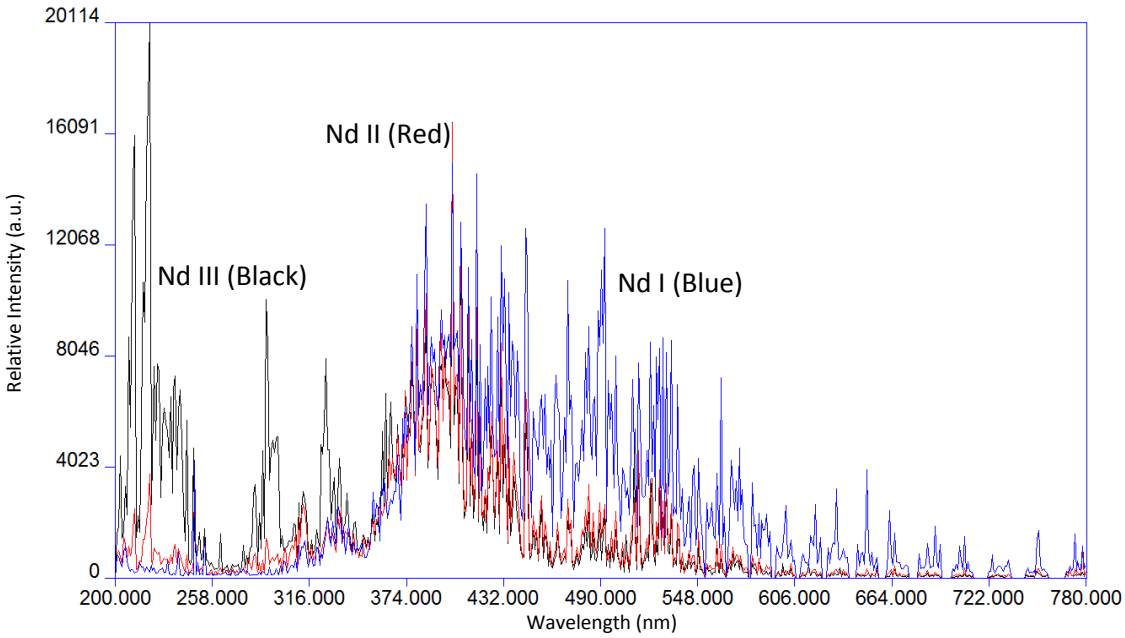

Figure 2.5 An Nd III, Nd II, and Nd I spectrum obtained at various plasma temperatures by varying the observation time of the plasma. These plasma spectra were not obtained at the same time and have been overlaid and scaled for clarity. The Nd III emission (black) was observed very shortly after plasma formation while the Nd II (red) and the Nd I (blue) spectra were observed at later times. This shows roughly the fraction of each ionization state present at different plasma temperatures and also demonstrates the decrease in plasma temperature with time. This is discussed more in Chapter 4.

contributing to multiple other problems that will be discussed in Chapter 4 (i.e. the blending of emission lines which renders them unresolvable).

An optically thin plasma is required to make atomic measurements. To be considered "optically thin" all photons emitted from an excited energy level via spontaneous decay must not be reabsorbed by another atom before leaving the plasma. Thus, in an optically thick regime not all photons emitted via spontaneous emission are observed and the resulting measured branching fractions could be incorrect since the absorption of photons (and thus the measured "emission") is dependent on the transition strength.

Being in a regime where no collisional de-excitation occurs is also imperative. If the ions and atoms are not spontaneously decaying, but are de-exciting due to collisions between atoms, branching fractions cannot be measured, as the observed

emission will again change based on the plasma density and temperature. In a regime of LTE and optical thinness the electron density and temperature will allow for atomic measurements. A good test for optical thinness that is traditionally used in LIBS, although not in my experiment, is the oxygen test, where the intensities of each of the emission lines in the oxygen triplet at 777 nm are compared to each other. The intensity of the three emission lines are fixed in a ratio of 7:5:3 and any deviation of the ratios indicates that the plasma is not in a regime of optical thinness, or non-collisional de-excitation. This test could not be used for our studies since all measurements were obtained in argon gas as previously mentioned but observing how lanthanide emission lines in a given energy levels are changing with various pressures could be conducted (which is the same test).

References

[1] Miziolek, A. W., Palleschi, V., & Schechter, I. (Eds.). (2006). *Laser-induced breakdown spectroscopy (LIBS)* (pp. 127-136). Cambridge: Cambridge University Press.

[2] Singh, J. P., & Thakur, S. N. (Eds.). (2007). *Laser-induced breakdown spectroscopy*. Elsevier.

[3] Cremers, D. A., Yueh, F. Y., Singh, J. P., & Zhang, H. (2006). *Laser-Induced Breakdown Spectroscopy, Elemental Analysis*. John Wiley & Sons, Ltd.

[4] Radziemski, L. J., & Cremers, D. A. (1989). Laser-induced plasmas and applications.

[5] Cremers, D. A., & Chinni, R. C. (2009). Laser-induced breakdown spectroscopy—capabilities and limitations. *Applied Spectroscopy Reviews*, *44*(6), 457-506.

[6] Pasquini, C., Cortez, J., Silva, L., & Gonzaga, F. B. (2007). Laser induced breakdown spectroscopy. *Journal of the Brazilian Chemical Society*, *18*(3), 463-512.

[7] Peratt, A. L. (1996). Advances in numerical modeling of astrophysical and space plasmas. *Astrophysics and space science*, *242*(1-2), 93-163.

CHAPTER 3: Experimental Apparatus

Our laser-induced breakdown spectroscopy setup for atomic measurements consisted of a high-energy pulsed laser, various optical components, vacuum chamber, spectrometer, and computer. This chapter will describe the setup and component design of the LIBS experimental apparatus for atomic measurements. Figure 3.1 shows an overview of the LIBS experimental setup consisting of the aforementioned components to be described in detail in the following sections. This chapter will also discuss an optical parametric oscillator (OPO) that was used for a hyphenated LIBS technique that is discussed in Chapter 7.

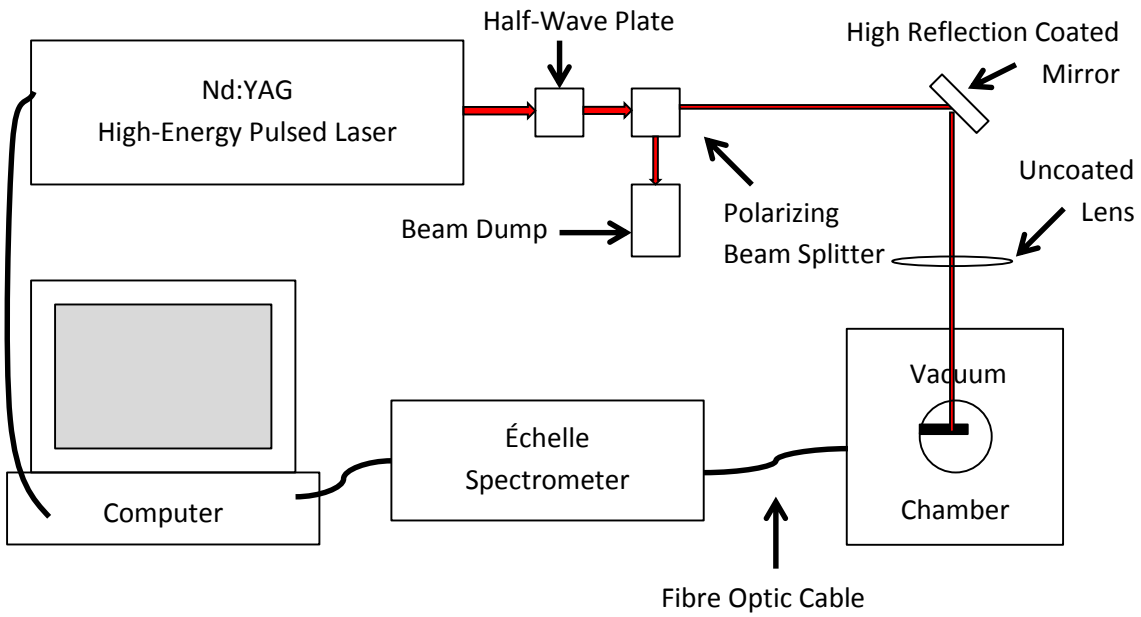

Figure 3.1 An overview schematic of the experimental setup for our atomic measurements apparatus. The setup contains a high-energy pulsed infrared laser, energy attenuating optics, directing and focusing optics, vacuum cube, optical fiber, échelle diffraction grating spectrometer, and control computer.

3.1 High-Energy Pulsed Laser

A neodymium-doped yttrium aluminum garnet (Nd:YAG) pulsed laser (Quanta Ray LAB-150, Spectra Physics) was used to produce the laser-induced plasma. The Nd:YAG laser has a 10 ns pulse duration, 10 Hz repetition rate, and operates at its fundamental frequency with a wavelength of 1064 nm. The laser outputs a maximum

energy of 650 mJ per pulse. This pulse duration and energy results in a large peak power. For our atomic measurements the laser pulse energy is attenuated down to 30 mJ per pulse through the use of a rotatable half-wave plate and polarizing beam splitter (Glan-Taylor calcite polarizer). See Figure 3.2. With a laser pulse energy of 30 mJ focused to a roughly circular spot with a diameter of 100 μm, an irradiance of 10^{10} W/cm^2 is achieved. This irradiance is in agreement with previously published breakdown threshold irradiances [1]. A half-wave plate rotates the polarization of linearly polarized light incident upon it. It has two different indices of refraction along perpendicular directions (fast and slow axes) arising from the crystal lattice structure. The properties of a half-wave plate are such that when the light exits the crystal the polarization component of light parallel to the slow axis is one half wavelength retarded relative to the polarization component of light parallel to the fast axis. By careful choice of the orientation of the crystal the linear polarization of the incident laser pulse can be rotated by any angle through this induced phase shift between the two polarization components of light.

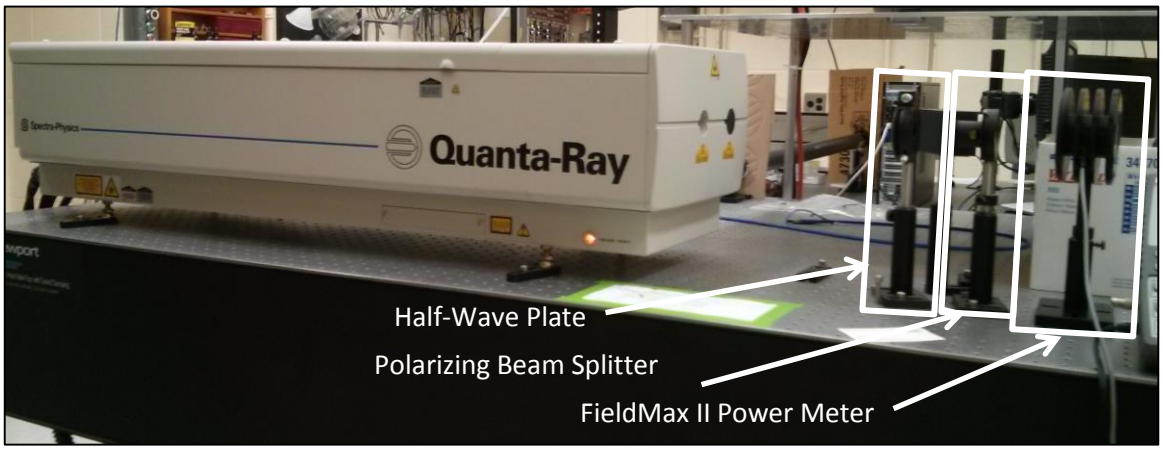

Figure 3.2 Spectra Physics Quanta Ray high-energy pulsed laser with half-wave plate, polarizing beam splitter, and power meter.

A polarizing beam splitter is placed after the half-wave plate that only transmits the vertical (p-polarized) polarized component of light and reflects the horizontally (s-polarized) polarized component. By rotating the half wave plate appropriately the polarization of the laser light is rotated sufficiently so that only 30 mJ per pulse (as measured by an optical power meter, Coherent FieldMax II) is vertically polarized and thus transmitted through the polarizing beam splitter. The

beam splitter directs the remaining energy of the laser pulse into a beam dump. The polarization of the beam is insignificant for production of the plasma and is only important in the energy attenuation of the beam. The laser pulse is directed into a vacuum chamber using high-damage threshold 1064 nm high-reflection dielectric-coated mirrors (>99.9% of the 1064 nm light is reflected). The laser light is focused with an uncoated 75 mm diameter plano-convex lens with a focal length of 175 mm. The focused laser light passes through a 1064 nm anti-reflection coated vacuum window into the vacuum chamber and onto the target. A computer, with a fast-pulse generator that runs the spectrometer and analysis software (to be described in Section 3.3), controls the timing and firing of the laser.

3.2 Vacuum Chamber

The target is contained inside a vacuum cube of volume 3500 cm^3. Each side of the vacuum cube has a 6-inch circular ConFlat (CF) vacuum flange with 2.75-inch CF flange openings in the center for optical access (except for the bottom side which has a blank 6-inch flange). See Figure 3.3. As mentioned in Section 3.1, attached to the front of the chamber is a 2.75-inch flange with an AR coated window for transmitting the incident laser light. Attached to the back of the vacuum cube is a Pirani convection module pressure gauge (Kurt J. Lesker 300-series) monitoring the pressure inside the chamber calibrated for nitrogen gas. The pressure is monitored through the voltage required to keep a gold-plated tungsten filament at a constant temperature against thermal cooling by the gas environment. The vacuum chamber was filled with argon gas for increased light emission from the plasma. Since the pressure gauge is calibrated to nitrogen, the displayed pressure was converted to actual pressure using a piecewise function based on manufacture-calibrated specifications.

The vacuum chamber is evacuated with a mechanical vacuum pump (Varian DS-302). The pump is able to evacuate the chamber down to 3 mTorr (measured by two Varian thermocouple gauges), which is more than satisfactory for my research. The leak rate of the chamber after approximately 24 hours of pumping and then closing of all valves was 40 mTorr per hour, which is also satisfactory for my research.

Argon gas is slowly let into the chamber through a needle valve. With fine control of the shut off valve for the vacuum pump and needle valve for inflow of argon, the pressure is adjustable from 100 mTorr to atmosphere and is stable for hours at a time.

Attached to the top of the cube is a vacuum rotational feedthrough with a direct current (DC) motor mounted to the 6-inch flange. The target is screwed onto an 80-pitch screw drive driven by a hexagonal key (which is the DC motor drive shaft) inside the 80-pitch screw, see Figure 3.4. The screw turns within an 80-pitch sleeve

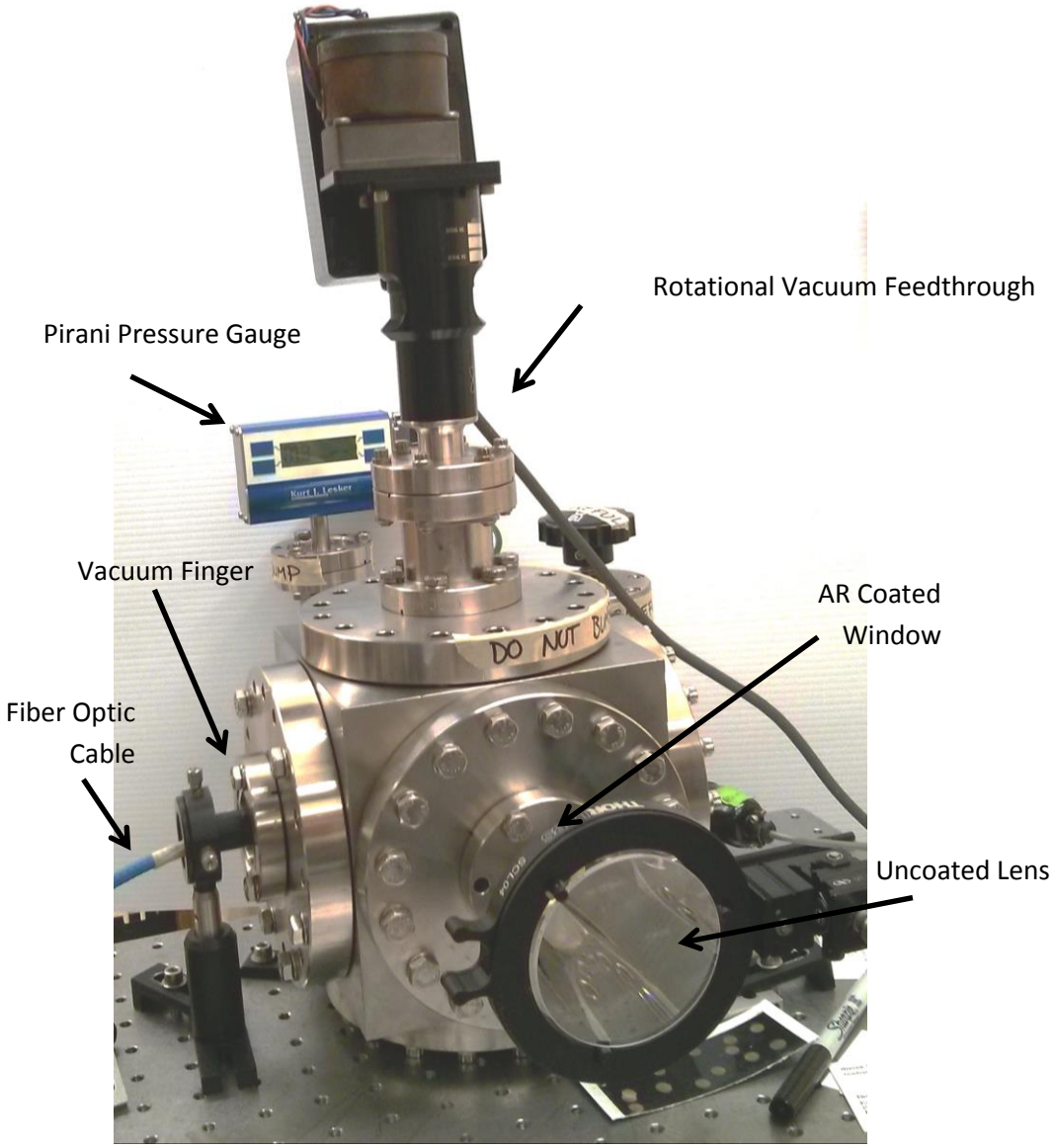

Figure 3.3 The vacuum cube with rotational feedthrough, AR coated window, uncoated lens, Pirani pressure gauge, vacuum finger, and fiber optic cable.

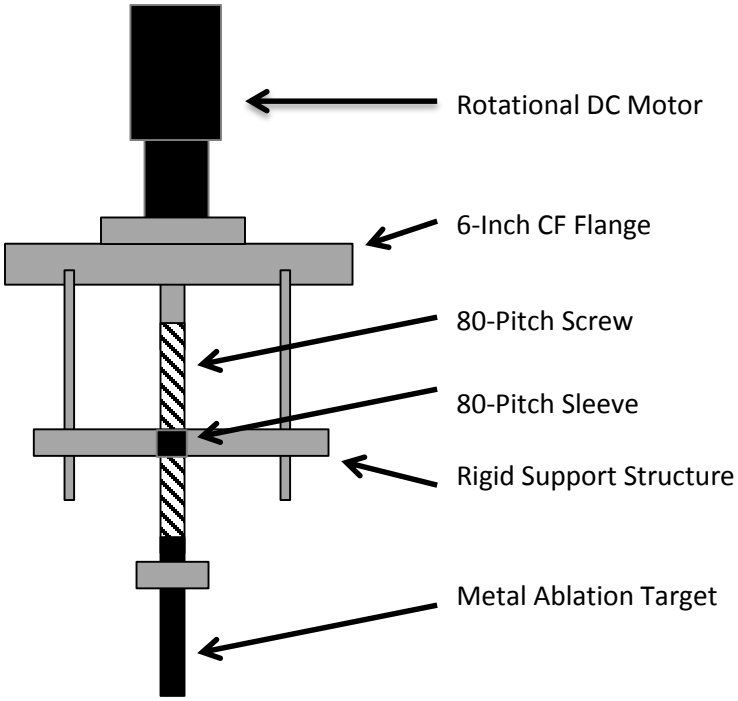

Figure 3.4 A schematic of the vacuum rotational feedthrough and target mounting system. A target is screwed onto the 80-pitch screw drive that passes through an 80-pitch screw sleeve that is driven by a rotational DC motor.

rigidly attached to a support structure inside the chamber. As the motor spins the target rotates and translates linearly, thus the fixed laser spark ablates the target in a helical pattern resulting in a new area of the target ablated with subsequent laser pulses. This is necessary to keep the laser from "drilling" a crater into the target. The vacuum feedthrough flange was mounted on top of the cube with a single 6-inch Viton O-ring for ease of removal when changing targets as well as access into the vacuum cube. The right side of the chamber has a regular 2.75-inch flange window (unused in the experiment) for viewing inside the chamber.

The left side of the vacuum cube has a modified 2.75-inch flange with an inset vacuum finger that extends into the vacuum chamber, see Figure 3.5. I designed this flange/finger for improved light collection. The vacuum finger has a 1-inch diameter stainless steel tube attach to the flange with a quartz window mounted at the end of the tube to allow for positioning of the fibre closer to the plasma. The center of a 2.75-

inch flange flat was bored out to a 1-inch diameter hole and a 1-inch diameter stainless steel tube was vacuum welded to the modified flange. The stainless steel tube protruded three and a half inches into the vacuum chamber from the inside surface of the modified flange. A custom-designed window holder was vacuum welded to the other end of the stainless steel tube. The window was inserted into the window holder and pressed against a rubber O-ring. A cover attached by screws into the end of the tube pressed the window against the O-ring and this formed a vacuum seal around the window. This allowed for cleaning and changing of the window at the end of the vacuum finger. The vacuum finger allowed for improved light collection by moving our optical fibre 9 centimetres closer to the plasma. Light is emitted isotropically from the plasma and therefore intensity drops approximately as one over the distance squared. Moving the optical fibre closer to the plasma allowed for capturing more light from the plasma and increased our sensitivity and accuracy by increasing the signal-to-noise ratio (SNR).

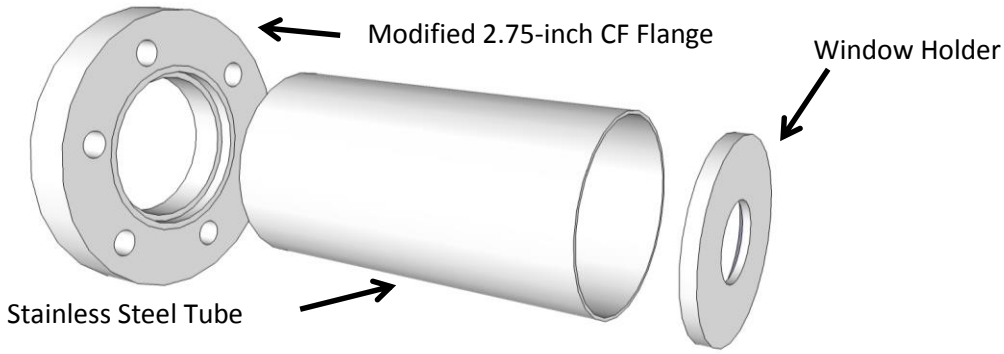

Figure 3.5 The vacuum finger design schematic with a modified bored out 2.75-inch CF flange, 1-inch diameter stainless steel tube, and vacuum sealable window holder.

3.3 Light Collection and Analysis

A 1-meter long UV-enhanced optical fibre is attached to an SMA connecter inside a 4-inch length, half-inch diameter tube positioned inside the vacuum finger. This allows the end of the fibre to be located millimetres from the quartz window at the end of the vacuum finger 20 mm from the plasma. The optical fibre is then attached to our échelle diffraction grating spectrometer. In our lab we have two spectrometers: an LLA Instruments ESA 3000 and LTB Aryelle Butterfly. Each

spectrometer has an échelle diffraction grating spectrograph and camera. All data was taken with the ESA 3000 spectrometer, which I will now explain in detail.

The ESA 3000 spectrometer consists of an échelle diffraction grating, dispersing prism, image intensifier, and charge coupled device (CCD). The light from the optical fibre is directed onto the échelle diffracting grating, a reflective surface with equally spaced grooves. The core of the optical fibre (600 micron diameter) acts as the entrance slit of this spectrometer. An échelle diffraction grating is characterized by a low groove density with a high angle of incidence optimized for high diffraction orders. In our échelle orders 29 to 129 are used and all overlap. The diffraction grating gives a 1-dimensional spread of light with longer wavelengths (infrared light up to 780 nm) contained in the lower orders and shorter wavelengths (ultraviolet (UV) light down to 200 nm) contained in the higher orders. The lower orders have a larger angular spread as well as a larger range of wavelengths; this results in decreased spectral resolution at the longer wavelengths. In fact, our spectrometer is optimized for high resolution in the ultraviolet. The manufacturer quotes spectrometer resolution as 0.005 nm at 200 nm and 0.019 nm at 780 nm. A cross-dispersing prism is used to separate the order overlap which results in a 2D spread of light, the 2 dimensions being order (which is also wavelength) and wavelength. The 2-dimensional array of light is then directed using a focusing mirror towards the image intensifier. See Figure 3.6 for the manufacturer-provided schematic of the optical path inside the échelle spectrometer.

The 2-dimensional array of light is incident on a circular image intensifier consisting of a photocathode, micro-channel plate, and phosphor screen. The photons diffracted and dispersed hit the photocathode and electrons are produced and accelerated towards the micro channel plate (MCP). The MCP then multiplies the number of electrons through a cascading event based on the voltage applied to the MCP. An amplification setting in the spectrometer software is used to vary the voltage applied to the MCP to control the number of electrons produced to use the full dynamic range of the phosphor screen without saturation. The increased number of electrons is then incident on a phosphor screen, which produces photons of one frequency proportional to the number of electrons incident on the screen. The

produced photons are then detected and recorded by a 2-dimensional 1024 by 1024 array (24 x 24 μm^2 pixel size) of charge-coupled devices (CCD).

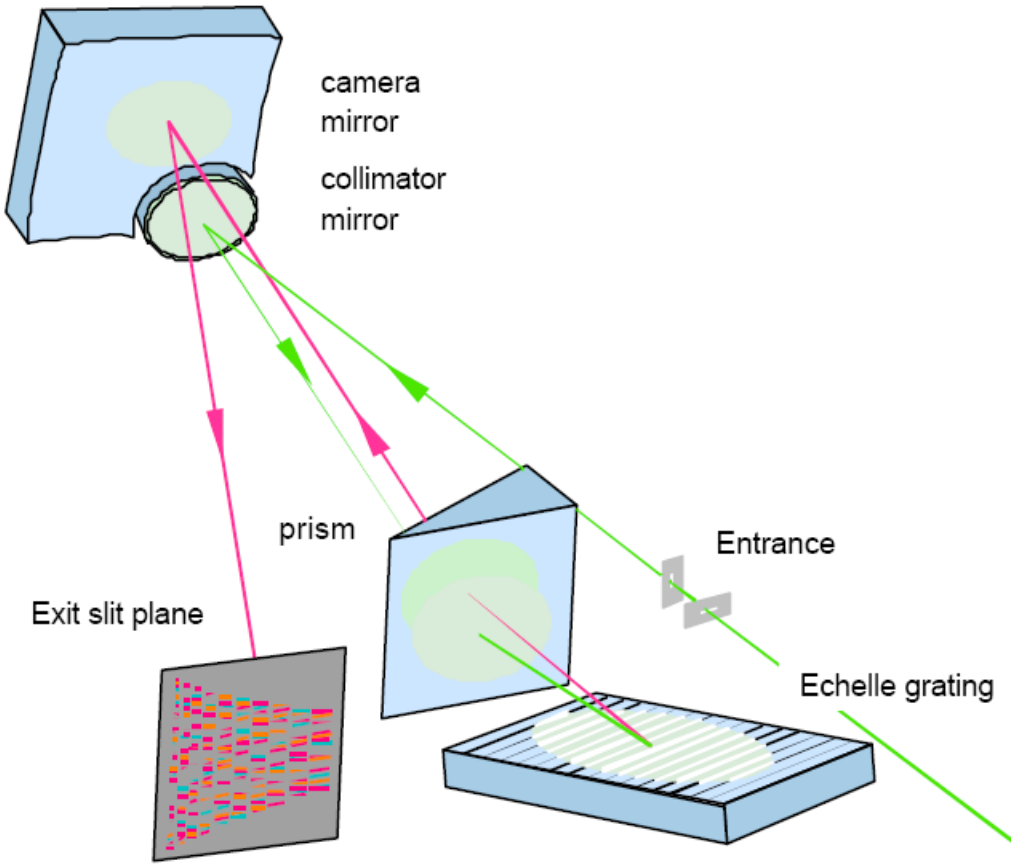

Figure 3.6 Schematic of our échelle diffraction grating spectrometer. The incident light is collimated with a mirror, directed through a prism, and then incident on the diffraction grating. The diffracted light is then cross-dispersed by a prism and is imaged onto the CCD in the exit slit plane [2].

Since the image of the entrance "slit" is circular and the CCD is square, a mapping of a circle to a square needs to be chosen. For optimal resolution in the ultraviolet regime, spectral gaps in the spectrometer resulted from the mapping of the image (circular) to the CCD array (square). At this optimal UV resolution, some light with longer wavelengths is dispersed and diffracted outside the CCD array; these are areas of missed light that we refer to as "spectral gaps," see Figure 3.7. Mapping could be chosen to direct all light onto the CCD array but this will reduce resolution by increasing the range of wavelengths incident on each CCD pixel. The 2-dimensional

CCD array pixel intensity values (proportional to incident photons) are the raw data. This 2D picture is known as an échellogram. The CCD array is readout by the computer that performs a spectral calibration to take into account the variation of the imaging systems response with wavelength and then stitches together all the échelle orders to produce a spectrum from the échellogram.

A computer controls the timing of the spectrometer with a fast pulse generator capable of nanosecond accuracy. TTL-pulses are sent from the pulse generator to control the flash-lamp and Q-switch of the high-energy pulsed laser as well as the image intensifier. In a graphical user interface (GUI) a gate delay is set to a desired time after plasma formation for observation. The gate delay sets the time between a TTL-pulse for Q-switch activation of the laser and a TTL-pulse for activation of the image intensifier. A gate width, which determines how long the camera intensifier window is "open" and thus how long the plasma is observed, is also set in the GUI. The nanosecond timing allows for any observation window length to be set anywhere in time. Typical gate delays are between 500 nanoseconds and 10 microseconds with gate widths ranging from 100's of nanoseconds to 20 microseconds. This timing is shown schematically in Figure 3.8.

3.4 Optical Parametric Oscillator

A second laser system, an optical parametric oscillator (OPO), was used in a hyphenated technique called LIBS-LIF (laser-induced breakdown spectroscopy – laser-induced fluorescence) as described in Chapter 7. An OPO is a high-energy tuneable pulsed laser with a continuously variable wavelength from approximately 400 to 700 nm. The OPO uses a non-linear optical crystal and a laser pump source to produce the range of wavelengths, see Figure 3.9.

A second Nd:YAG laser, identical to the one described in Section 3.1, was used as the pumping source for the OPO. The Nd:YAG laser used for pumping the OPO incorporated a third harmonic generating (THG) crystal. The THG crystal triples the frequency (non-linear frequency conversion) of the laser and thus the pump laser has a wavelength of 355 nm. The 355 nm Nd:YAG laser outputs 220 mJ per pulse into the OPO.

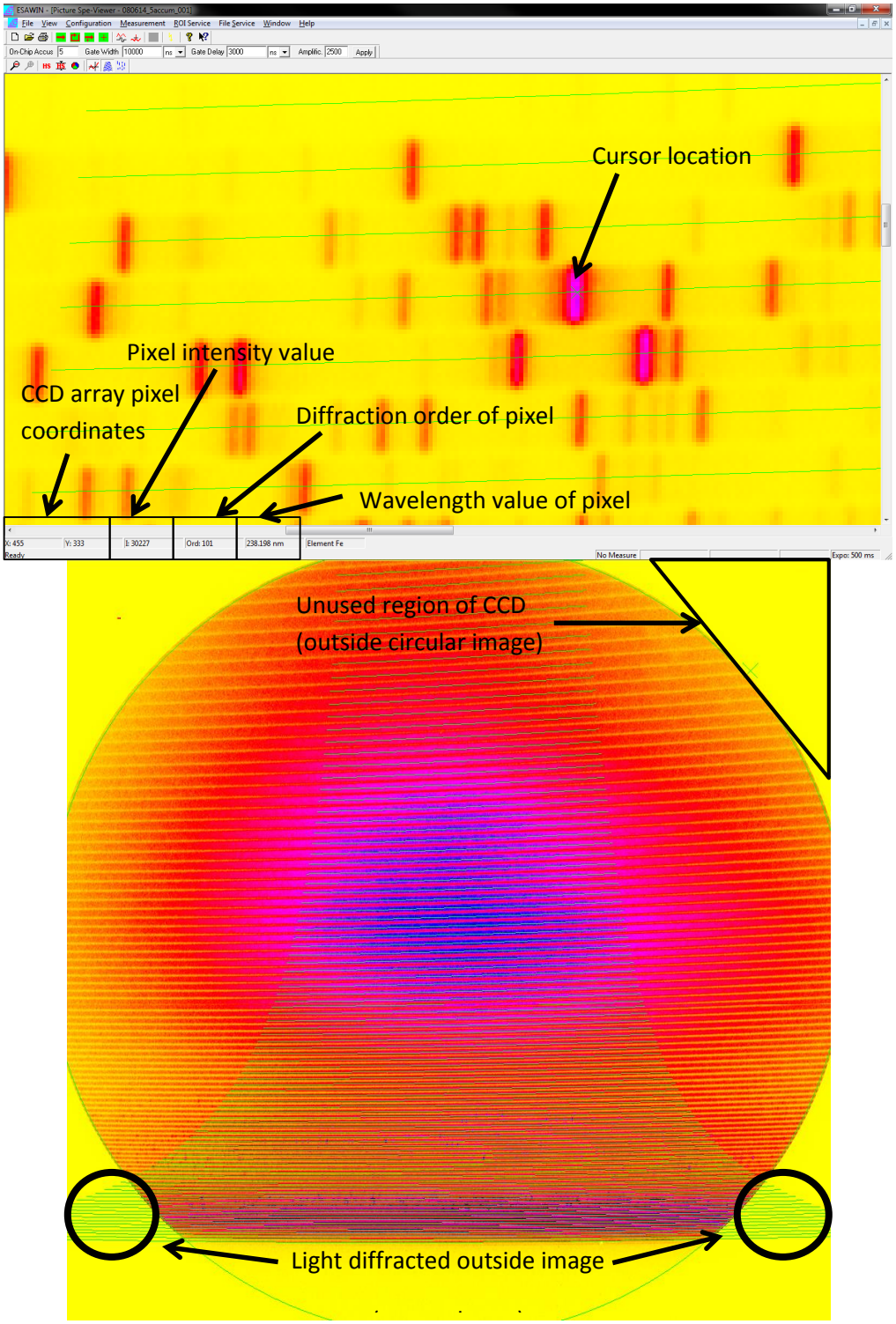

Figure 3.7 Top: A zoomed in region of an échellogram displaying various peaks and diffraction orders shown by the green lines. Bottom: An échellogram of a deuterium-tungsten lamp displaying the mapping of the diffraction pattern (green lines), circular image, and square CCD array.

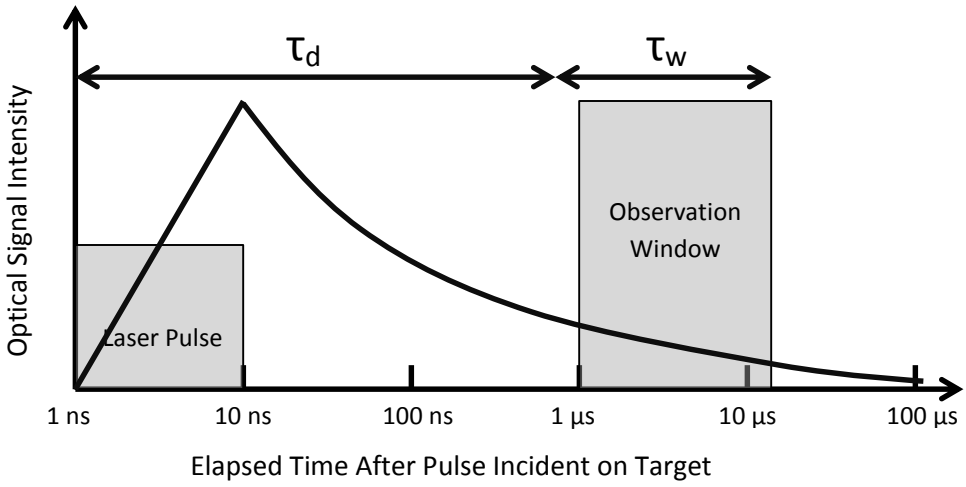

Figure 3.8 A timing diagram of the incident laser pulse, plasma evolution, and observation window characterized by delay time (τ_d) and gate width (τ_w).

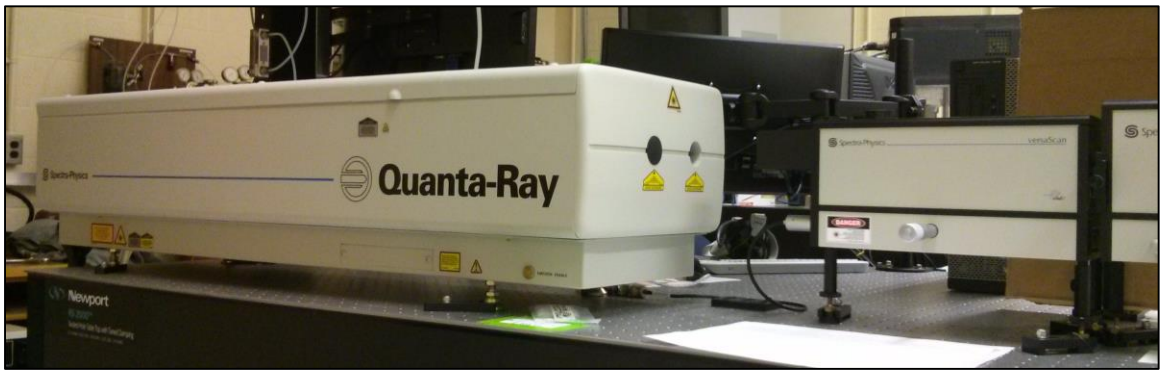

Figure 3.9 The frequency tripled Nd:YAG laser (left) used to pump the OPO (right).

The OPO also contains a non-linear crystal. A desired wavelength of light is produced based on the orientation of the incident laser light on the non-linear crystal. The crystal lattice will produce two beams, a signal and idler beam from the incident laser light. The frequency of the signal and idler will sum to the frequency of the pump laser light. The energy output by the OPO is dependent on wavelength and varies in the range from 10 to 100 mJ per pulse. The spectral width of the OPO pulse is 6 wavenumbers, which is sufficient for laser-induced fluorescence. The OPO beam is intrinsically highly divergent and not well collimated. The vertical beam divergence

is specified at <25 mrad and the horizontal beam divergence is specified at <1 mrad resulting in an elliptically shaped beam.

The OPO setup is shown in Figure 3.10. An iris set to a 1 cm beam diameter is placed 10 cm away from the OPO beam exit. This iris is used to block secondary beams exiting from the OPO as well as various reflections. A 1 OD (optical density) neutral-density half-inch circular filter is used to attenuate the beam down to one-tenth its initial energy. The initial OPO energy is much greater than what is required for our experiment as well as near the damage threshold for our optics. The beam is directed one meter down a thermoplastic polymer (ABS) containment tube towards a second iris that is manipulated based on experimental needs.

The beam then passes through a one-dimensional Keplerian telescope with two cylindrical lenses (plano-convex) to reduce the divergence the beam in the vertical direction. The second lens of this telescope was placed on a translation stage so that the lens position can be easily adjustable for optimal collimation of the beam in the far field. The beam was observed 10 metres from the second lens and the second lens was adjusted for optimal beam shape and collimation at this distance. 10 metres is longer than the beam path to the target, which made this distance satisfactory for observation of collimation. The OPO beam diameter is dependent on the focal length of the two lenses used in the Keplerian telescope. The focal length of the first cylindrical lens is 75.6 mm and the focal length of the second cylindrical lens is 110 mm.

The collimated beam is then directed to a second lens with aluminum-coated mirrors. The second lens is a spherical lens with a focal length of 50 cm. This lens is used to defocus the beam prior to it encountering the final focusing lens. This enlarges the size of the OPO beam at the plasma. This lens is needed as the OPO also must pass through the final focusing lens used to focus the 1064 nm Nd:YAG beam. Without this defocusing, the OPO beam is too small, a few hundreds of microns in diameter. The OPO beam needs to be similarly sized to the plasma at the target, which is a few millimetres. The beam is then directed with another Al-coated mirror towards a 70/30 visible beam splitter that overlaps the visible-wavelength OPO beam with the near-infrared Nd:YAG beam. The beam splitter reflects 70% of the visible

OPO beam (at a 45 degree angle of incidence) and transmits 70% of the infrared beam due to the visible-wavelength thin-film coating. The OPO and 1064 nm Nd:YAG beams are aligned collinear using this beam splitter and therefore had a collinear ablation/fluorescence geometry at the plasma. The OPO beam was approximately 1 by 3 mm in size at the plasma location.

The timing of the 355 nm Nd:YAG used for the pumping of the OPO was controlled using a delay generator (DG535, Stanford Instruments) synched to the flash-lamp output pulse of the 1064 nm Nd:YAG. This allowed both lasers to fire synchronously or with an adjustable delay set by the delay generator. The 1064 nm Nd:YAG laser was still controlled through the main spectrometer computer (with the fast-pulse generator), thus controlling the timing of both lasers and spectrometer.

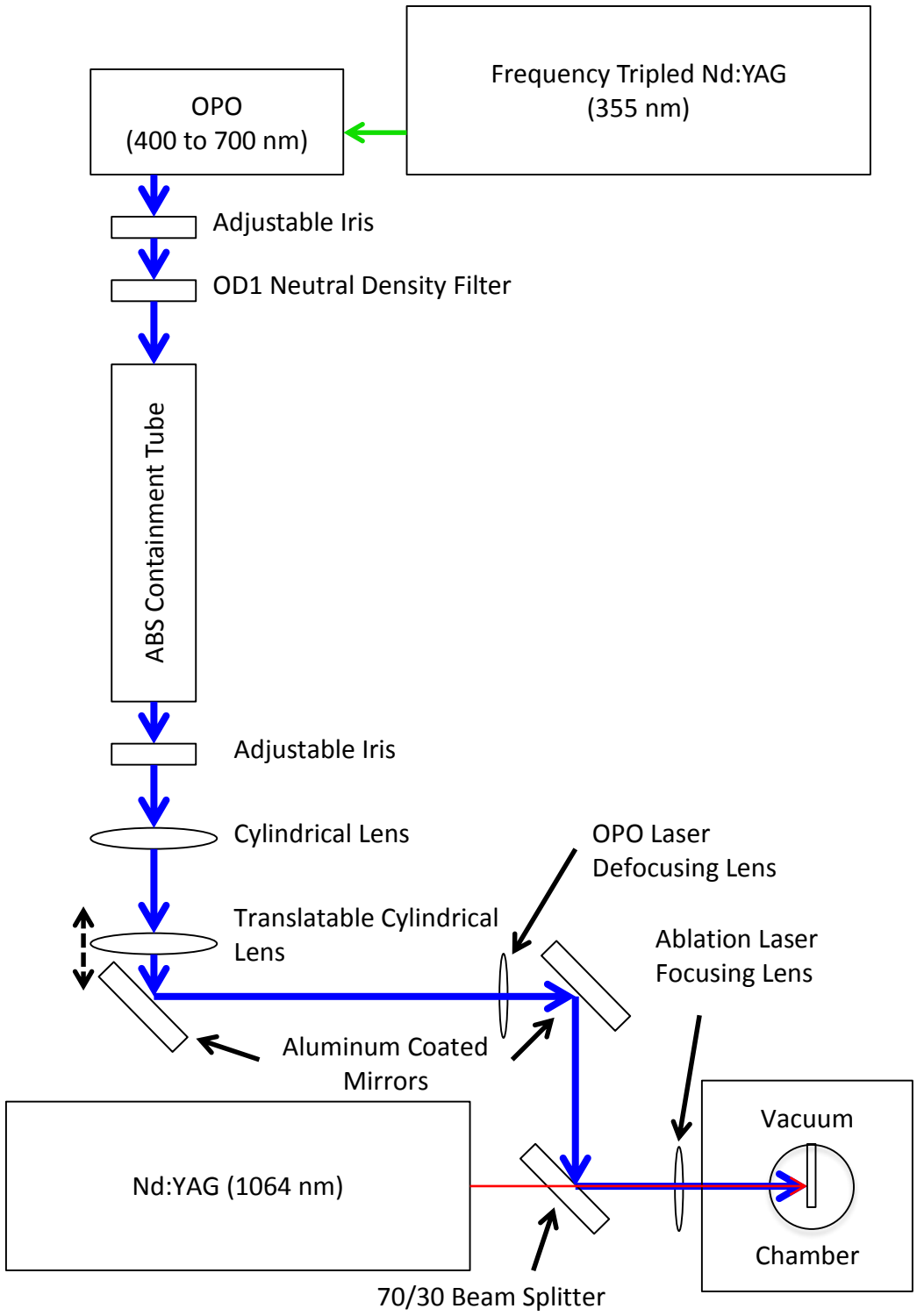

Figure 3.10 The LIBS-LIF experimental setup with a frequency tripled Nd:YAG excitation laser (355 nm), OPO (400 to 700 nm), various optical components, Nd:YAG (1064 nm) ablation laser, and vacuum chamber.

References

[1] Cremers, D. A., Yueh, F. Y., Singh, J. P., & Zhang, H. (2006). *Laser-Induced Breakdown Spectroscopy, Elemental Analysis*. John Wiley & Sons, Ltd.

[2] LLA Instruments GmbH (2005). Installation Guidelines - Echelle Spectra - Analyzer ESA300.

CHAPTER 4: Experimental Parameter Optimization to Improve Branching Fraction Accuracy

The majority of the work for my thesis consisted of optimizing experimental parameters to increase the accuracy of the branching fraction measurements as well as allowing the measurement of new, previously unmeasurable branching fractions. Improving the accuracy of the measurements was key since the motivation for the application in astrophysics was to address the problem of inaccurate or nonexistent data [1]. One significant problem with the current technique was the inability to make good measurements of less intense emission lines (small branches). Many less intense emission lines did not have a sufficient signal-to-noise ratio (SNR) and/or signal-to-background ratio (SBR) for accurate measurements. This resulted in a large uncertainty in the measurement of the integrated area under the curve of the peaks.

To increase the accuracy of branching fraction measurements, the SNR and SBR were carefully observed as experimental parameters were changed. It was also imperative to verify that the measured branching fractions did not change as the experimental parameters were changed. As well, the lineshape, full width half maximum (FWHM), and overlap of emission lines were key factors in determining the optimal regime in which to make measurements. The measurements obtained from the spectral data were the absolute intensities of the emission lines, which were determined from the integrated area under the curve calculated by the spectrometer software. This is further discussed in Chapter 5.

This chapter will discuss the effects on the measurements of varying observation time (gate delay and gate width) of the plasma, the effects that varying the argon pressure had on plasma formation and observation, and the effect of using different types of lanthanide targets. All parameter exploration studies were completed with neodymium due to the existence of good-accuracy results from several previous studies for comparison [2].

4.1 Plasma Observation Timing

The first parameters studied were the timing for observation of the plasma after its formation (gate delay time) and the length of time to observe the plasma (gate width time). The plasma evolved rapidly in time and the light emitted changed drastically over time which greatly affected the spectra obtained. The plasma was very hot (>50,000 K) and dense at formation and contained many highly excited and energetic atoms. Immediately after its formation no useful information could be obtained as discussed in Chapter 2. After a short delay, once the continuum emission had decreased, doubly-ionized lanthanide species were observed at delay times of 500 ns with a gate width of 500 ns (Figure 4.1). As the plasma cooled, expanded, and became less energetic, singly-ionized species became prevalent and dominated the plasma emission spectrum (Figure 4.2). The emission from the doubly-ionized species was nearly gone by about 1 μs and singly ionized species dominated from 1 to 3 μs. Singly-ionized absolute emission intensities were less intense than the doubly-ionized emission, and the MCP amplification voltage was considerably lower when observing doubly-ionized emission at 500 ns due to the number of photons emitted. After 5 μs the singly-ionized emission had decreased substantially and neutral atom emission had increased. Neutral atom emission dominated the plasma (Figure 4.3) until all emission has ceased or become unobservable, which was approximately 20 μs after formation. The neutral species absolute emission intensity was less intense than the singly-ionized and was therefore the least intense emission. The MCP amplification was raised considerably for neutral emission in comparison to the singly-ionized spectrum to use the full dynamic range of the imaging system. However, this also amplifies the noise. If one spectrum was obtained from 500 ns until 13000 ns after plasma formation and the MCP amplification was set appropriately so as to not saturate the imaging system, neutral emission would be so faint that accurate branching fractions would be impossible (the spectrum would near identical to Figure 4.1).

It was clear that there were three regimes of data that could be acquired, doubly-ionized, singly-ionized, and neutral atom emission. Lanthanides have very

complex atomic structure and therefore thousands of emission lines (seen in Figure 4.1-.3) that results in a "high density" of emission lines in the spectrum (Figure 4.4). In such areas of "high density" the emission lines begin to overlap resulting in two or more emission lines becoming unresolved and thus unmeasurable as seen in Figure 4.4 between 388.875 and 389.081 nm. Taking data in three different experimental regimes, one for doubly-ionized, one for singly-ionized, and one for neutrals, decreased the overlapping of lines and increased our ability to make measurements on emission lines that would ordinarily be overlapped if we had used only one measurement for all ionization states. By choosing the gate delay time and gate width time appropriately, emission from specific species was maximized while minimizing emission from the others. This reduced the density of emission lines in each spectrum as well as allowed the maximum emission from each ionization state. Frequently, singly-ionized and neutral emission lines would have center wavelengths separated by less than their FWHM resulting in overlapped and unresolved lines. This is shown in Figure 4.5. Since all emission lines from an upper energy level need to be measured in order to calculate branching fractions, having non-overlapping emission lines was vital.

Data was acquired from 0.5 to 1 μs for doubly-ionized atoms (Figure 4.1), 1 to 3μs for singly-ionized atoms (Figure 4.2), and from 3 to 13 μs for neutral atoms (Figure 4.3). The three regimes allowed for optimization of the MCP amplification voltage to use the full dynamic range of the imaging system, which also led to improved accuracy in the measurements. In no regime was there emission from only one ionization state, but it was possible to maximize the emission from the state of interest while minimizing the strength of emission from other ionization species. This allowed for an increase in the accuracy of measurements by minimizing emission line overlap. Molecular emission typically can be observed in LIBS plasmas at later delay times, but this was not observed in our spectra as a 99.9% Nd solid was used as the target and ablation was conducted in a pure argon atmosphere. This will be discussed more in Section 4.3.

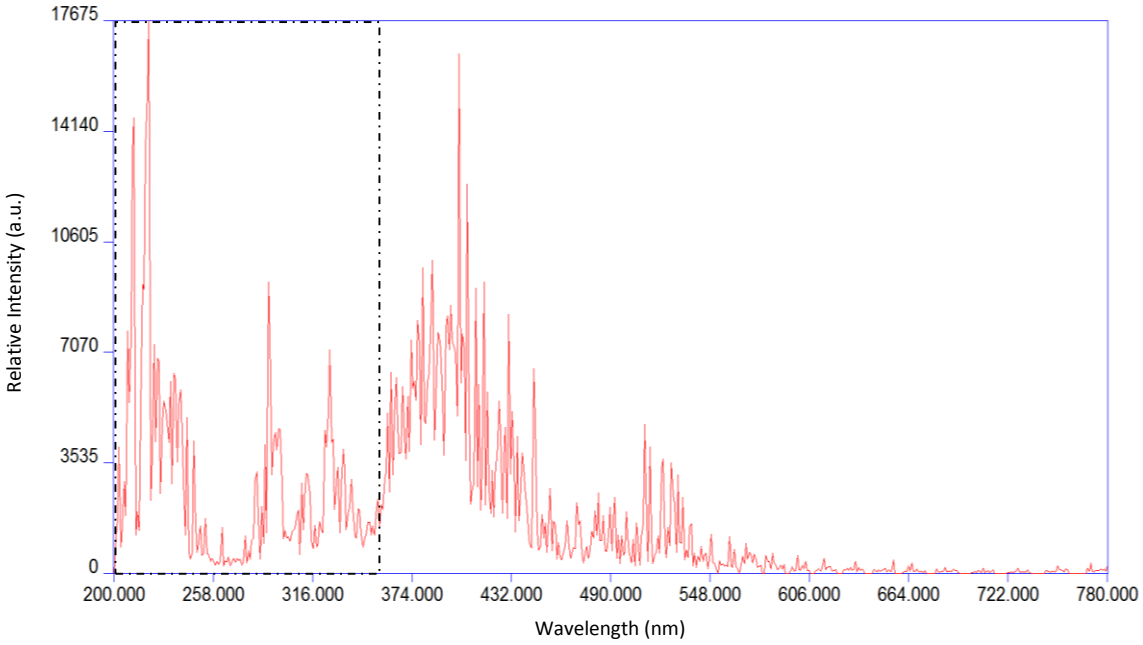

Figure 4.1 A doubly-ionized neodymium LIBS spectrum with a gate delay of 500 ns and gate width of 500 ns. The majority of the doubly-ionized emission lines are between 200 and 350 nm.

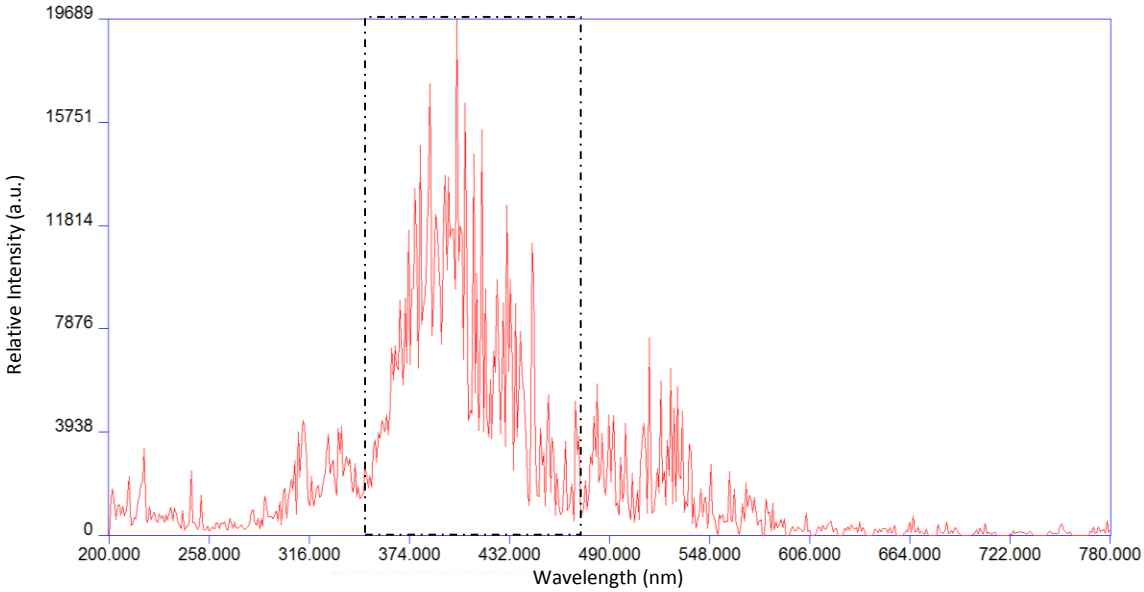

Figure 4.2 A singly-ionized neodymium LIBS spectrum with a gate delay of 1000 ns and gate width of 1000 ns. The majority of the singly-ionized emission lines are between 350 and 450 nm.

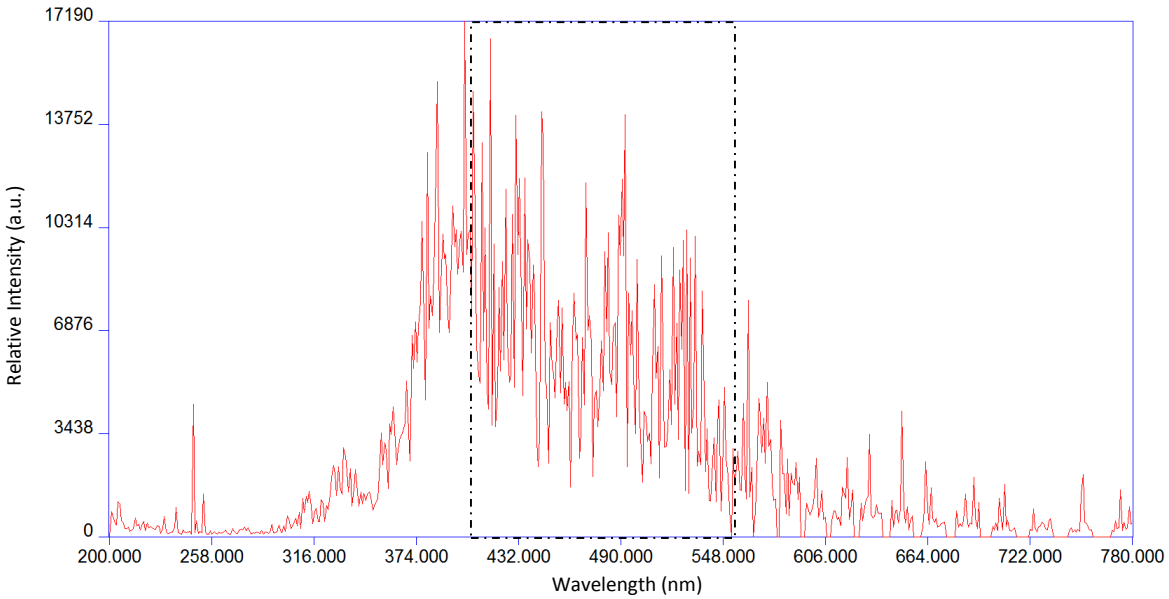

Figure 4.3 A neutral neodymium LIBS spectrum with a gate delay of 3000 ns and gate width of 10000 ns. The majority of the neutral emission lines are between 370 and 550 nm.

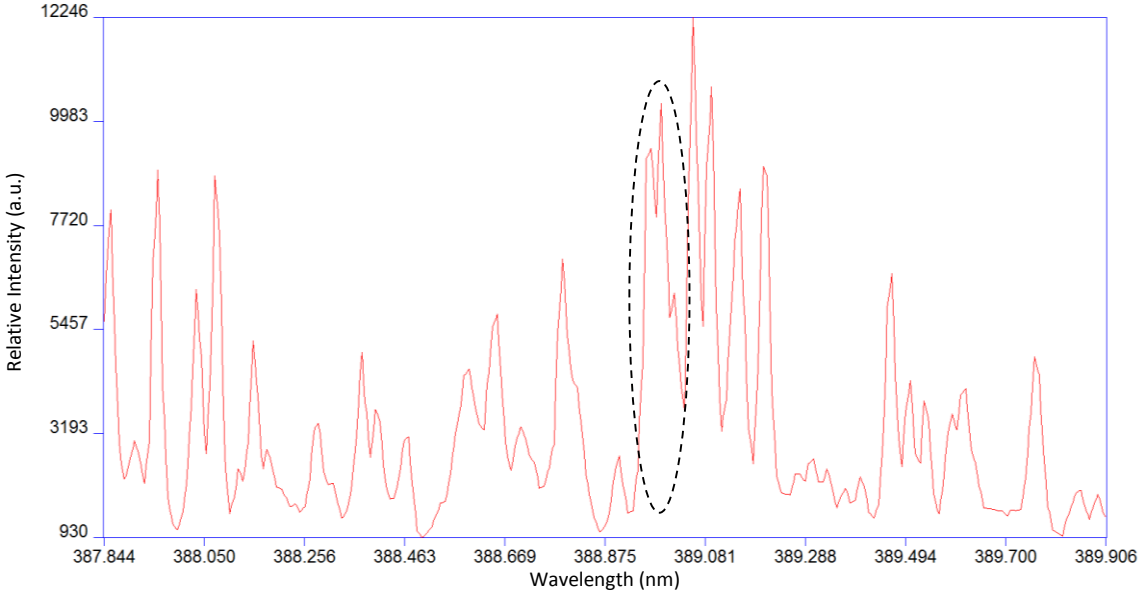

Figure 4.4 A "high density" (of emission lines) region of an Nd II spectrum showing overlap of multiple emission lines. The three emission lines between 388.875 nm and 389.081 nm (as well as others in this zoomed in region) are completely unresolved and unmeasurable. The x-axis is wavelength in nm and the y-axis is emission intensity in arbitrary units.

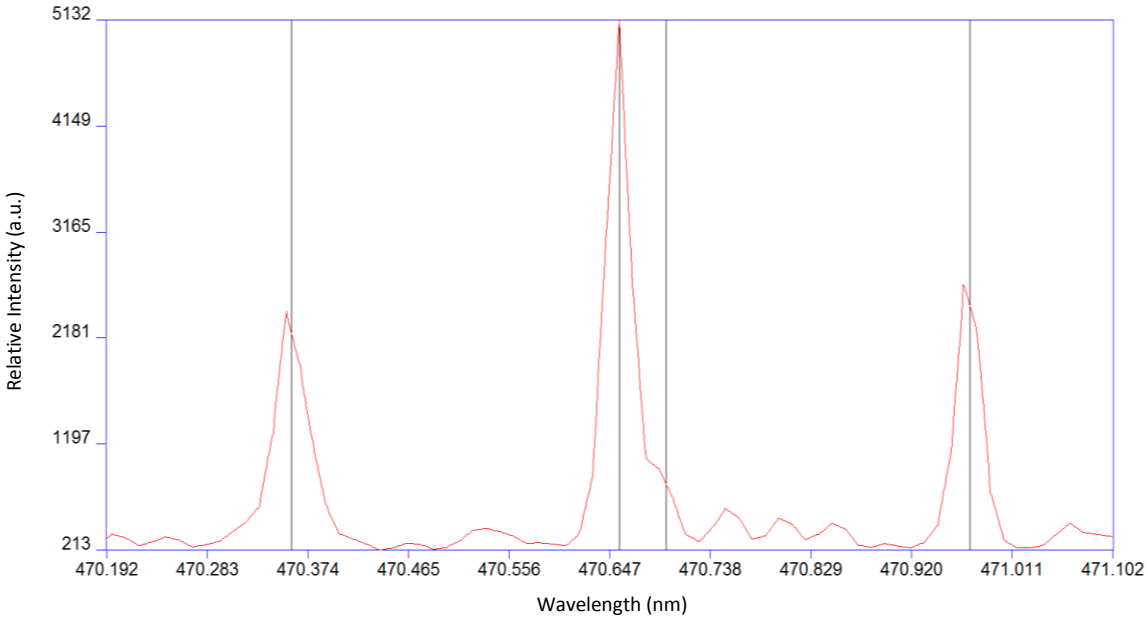

Figure 4.5 Overlap of emission lines from different ionization states. An Nd II line at 470.655 nm and a Nd I lines at 470.697 nm have overlapped and blended together. Since this spectrum was optimized for Nd II, the Nd I line was small enough that it did not affect the calculation of the Nd II line intensity and thus the Nd II emission line was measureable. The vertical black lines are markers for all Nd emission lines within the view range.

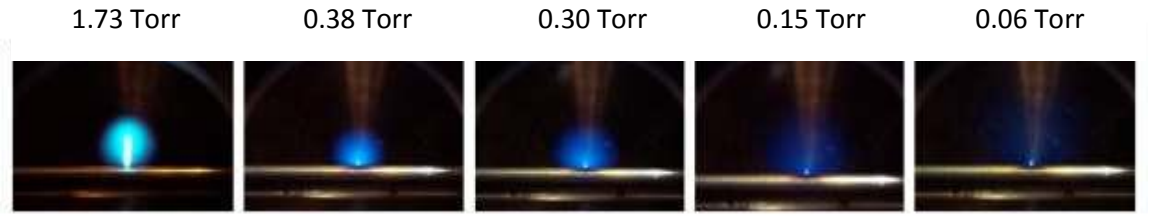

Figure 4.6 The plasma plume at various argon pressures. The laser is vertically incident from above on a steel target. The plasma is more diffuse at the lower pressure of 0.06 Torr compared to the hotter denser plasma at 1.73 Torr. This trend continues up to atmosphere [2].

4.2 Argon Pressure for Plasma Formation

As a LIBS plasma evolves in time it expands and cools. Changing the pressure of the gas surrounding the plasma will change how rapidly or how far the plasma expands and thus is directly related to the thermal evolution of the plasma. This also impacts the observation timing of the plasma as discussed in section 4.1. It is clear from human eye observation of the plasma that pressure has a great effect on the expansion of the plasma as seen in Figure 4.6.

At near-vacuum pressures of a few mTorr of argon the plasma appeared less dense and larger whereas at atmospheric pressures the plasma appeared to be very small, dense, and quite bright. The size of the plasma obviously greatly affects the electron density of the plasma during its evolution. As mentioned in Chapter 2, the Stark-broadening of lines is easily observable at the higher pressures due to the increase in electron density (Figure 4.7). The emission lines become broader and thus begin to blend together with neighbouring lines. This starts to become a large problem when the density of emission lines becomes high, as mentioned in Section 4.1. When lines broaden they may blend (overlap) together and become unresolvable. The blending of lines reduces the accuracy as well as making many lines unmeasurable depending on the severity of the overlap. Some lines could be manually fit if the blending is not too severe. A small overlapping of lines may result in an increased variation between spectra in the value of measured intensities, which in turn increases uncertainty in the measurement. A larger overlap typically makes both lines unmeasurable depending on the relative size of each emission line. If one line is considerably larger than the other, then only the small one will become unmeasurable (this can be seen in Figure 4.5 where only the small emission line is unmeasurable). It was apparent in our spectra that at lower pressures near vacuum the widths of the emission lines were limited by the imaging system as lowering the pressure below 1 Torr did not further decrease the emission line width, seen in Figure 4.8. Obtaining spectra at lower pressures was highly desirable due to the reduced blending and increase in spectral resolution of the emission lines. Again, this increased the accuracy and number of measurable lines.

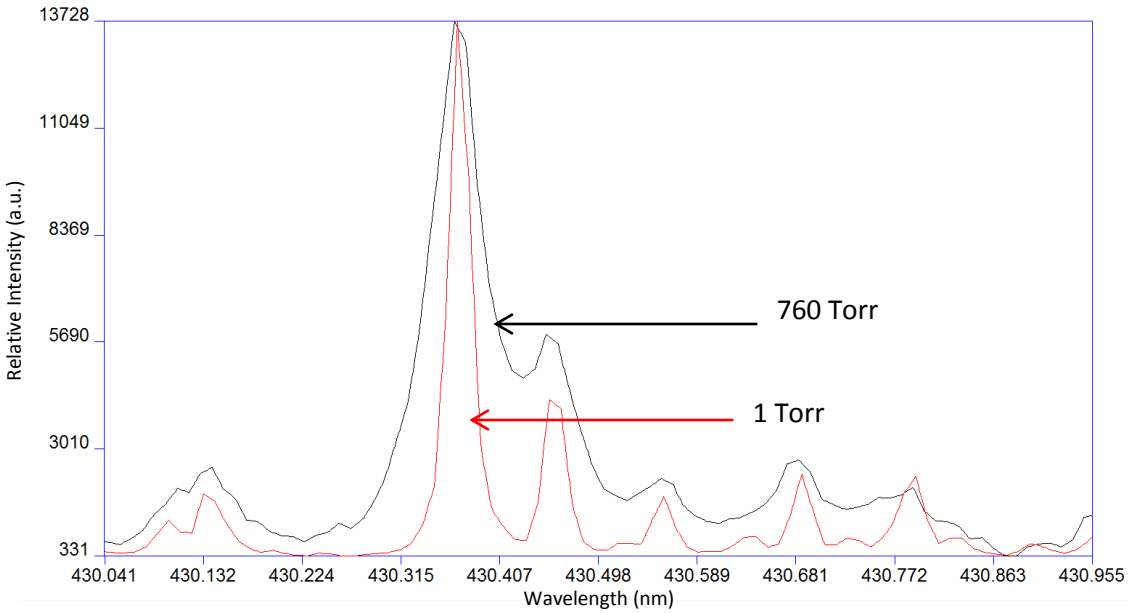

Figure 4.7 An emission line from an Nd II upper energy level at 430.357 nm at two different pressures. The red spectrum was obtained at a pressure of 760 Torr and the black spectrum was obtained at a pressure of 1 Torr. At atmospheric pressure the neighboring line to 430.357 nm has overlapped and become unresolvable but is clearly separated at 1 Torr.

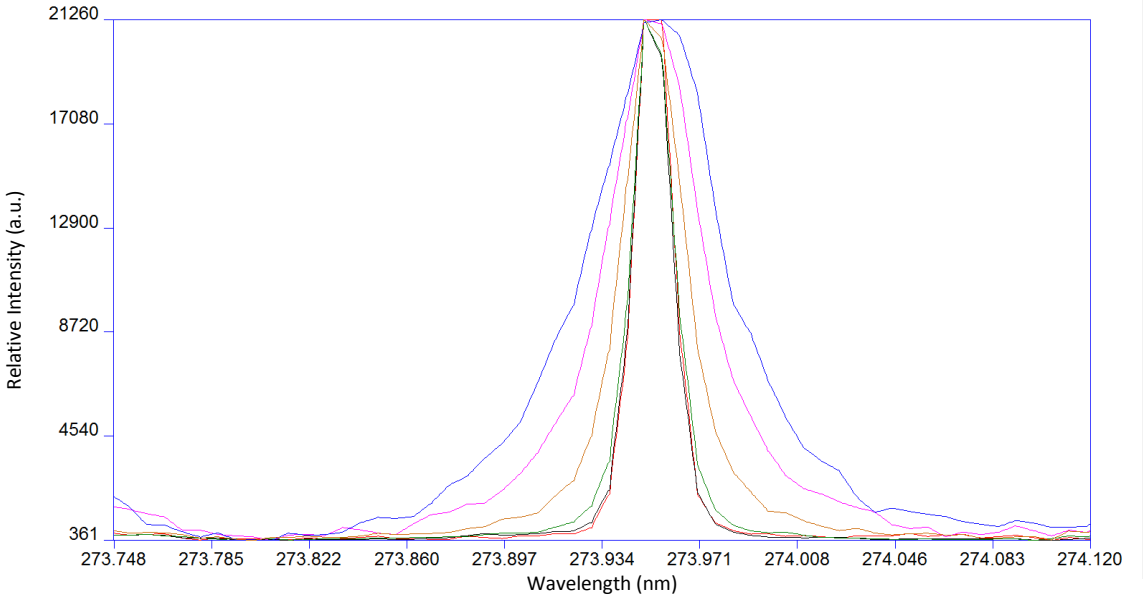

Figure 4.8 A singly-ionized iron emission line at various pressures. The FWHM does not decrease below 1 Torr and is limited by the resolution of the imaging system. The narrowest, three overlapping spectra emission lines are at 0.4 Torr (red), 0.7 Torr (black), and 1 Torr (green). The broader three lines are at 10 Torr (orange), 186 Torr (purple), and 513 Torr (blue).

It also needed to be verified that the measured branching fractions did not change with pressure in the chamber. Observed changes of branching fractions could result from the broadening of lines and/or the opacity of the plasma due to the pressure-related changes in size (and electron and ion density) of the plasma. Due to the broadening at higher pressures many smaller emission lines become unmeasurable as the pressure was increased towards atmosphere, which made branching fraction measurements impossible at these pressures. Interestingly, some authors describe atmospheric pressure LIBS measurements for absolute transition strengths [4]. However, it was observed that our branching fractions did not change at lower pressures and agreed with previous measurements performed with the same technique (LIBS) and with ion beam-laser experiments. See Figure 4.10. Since the measurements did not change with pressure and agreed with previous measurements within uncertainty it was also verified that the measurements were taken in a regime of optical thinness and no collisional de-excitation. This will be further discussed in Section 4.3. Therefore, measurements were taken at 1 Torr for optimal achievable emission line width.

4.3 Target Composition

As mentioned in Chapter 2, being in a regime of optical thinness and no collisional de-excitation is imperative to branching fraction measurements so that no photons are reabsorbed by the plasma and all energy levels have spontaneously decayed. Optical thickness and collisional de-excitation could result from a plasma that is too dense and too hot. Thus, the number of atoms or ions in the plasma (defined as N_{ion}, the plasma ion density) has a large role in determining the opacity of the plasma and the rate of collisional de-excitation. To reliably change N_{ion} by approximately an order of magnitude, two targets were prepared and used in the atomic measurement setup. One target was a pure 99.9% Nd solid and the other was a 10% (by weight) Nd powder/hot glue mixture (Figure 4.9). The 10% Nd by weight target proved to be problematic for making branching fraction measurements, as the emission lines were considerably smaller than when using the 99.9% solid target. All the smaller emission lines were unobservable, which resulted in almost no branching

fractions being calculated. Only a few of the upper energy levels with the strongest emission lines had branching fractions that were calculable (since all allowed transitions from of an upper energy level needs to be observed). The reduced emission from the upper energy levels also decreased the accuracy of the branching fractions that were calculable. Using the few upper energy levels with enough transitions visible, measurements were obtained using both targets. Branching fractions were obtained and compared with previous measurements performed with the same (LIBS) and different (beam-laser) techniques. It was verified that the measurements did not change and were consistent with previous measurements, seen in Figure 4.11. This demonstrated that changing the ion density by approximately a factor of 10 did not in any way impact our ability to measure relative intensities, which then allowed for measurements to be taken with the 99.9% Nd solid target and was advantageous due to its increased emission.

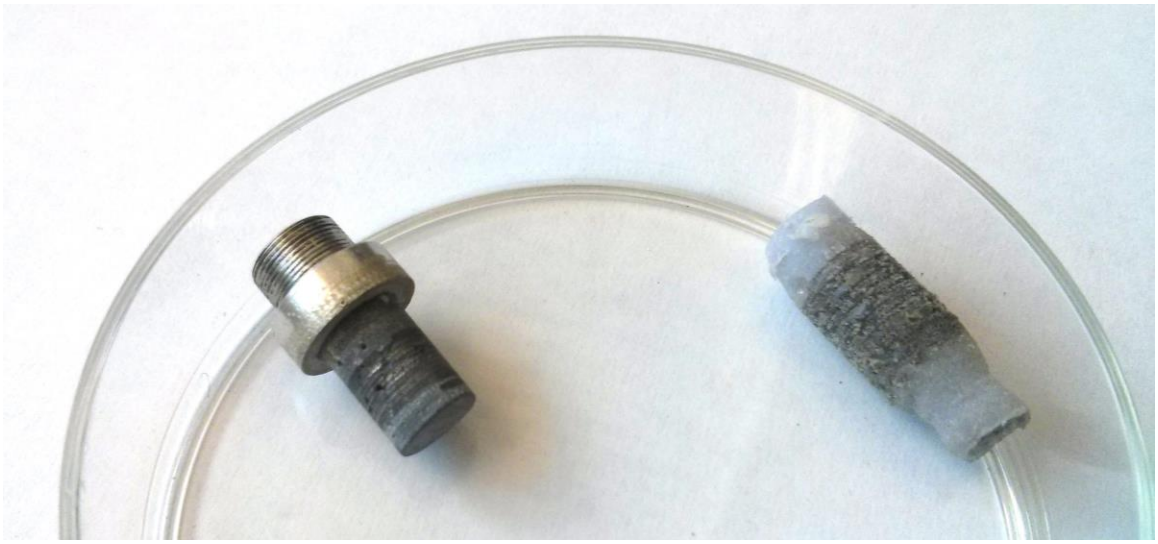

Figure 4.9 A solid 99.9%Nd target (left) and a 10% Nd by weight / hot glue mixture target (right). The helical ablation trails are clearly visible in both.

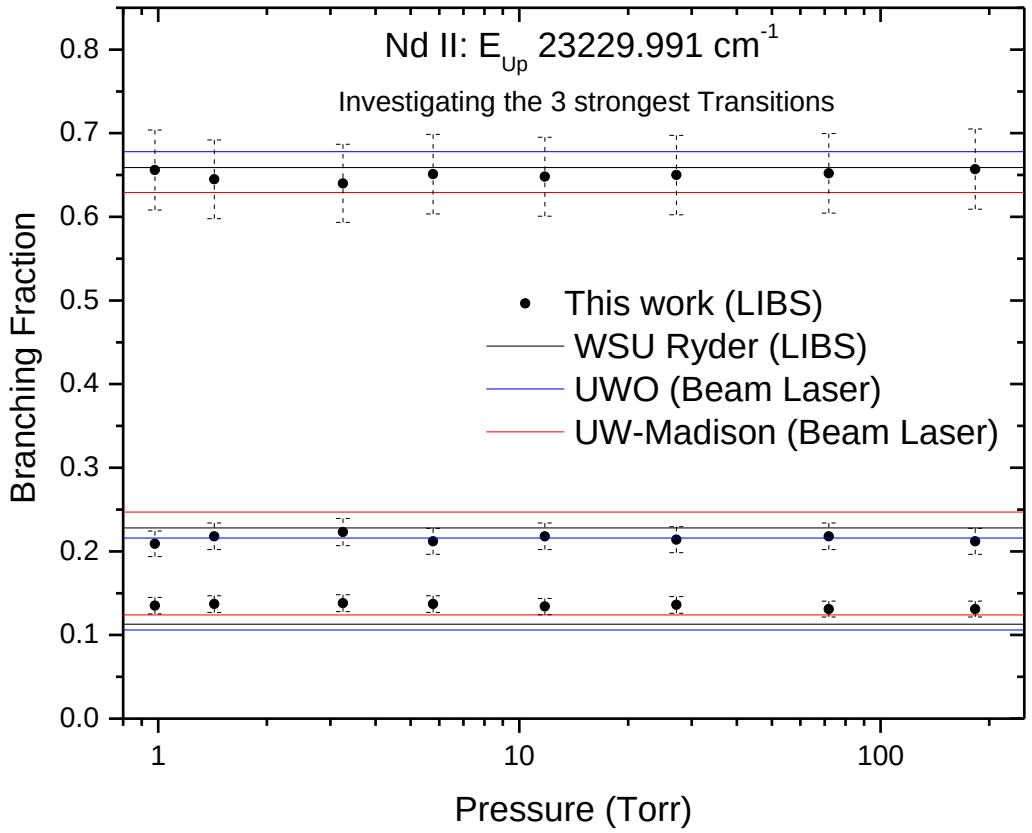

Figure 4.10 The relative strength of three branches from a single upper energy level in Nd II comparing LIBS measurements made at various pressures (data points) ranging from a few mTorr to atmosphere with previous measurements made at only one single pressure (measured value is a horizontal line). My measurements are black circles with associated error bars (error to be discussed in Chapter 5) compared to two beam laser experiments (UWO – blue line [2] and UW-Madison – red line [5]) and one LIBS experiment (WSU Ryder [3] – black). The measurements did not change with pressure and agreed with previous results.

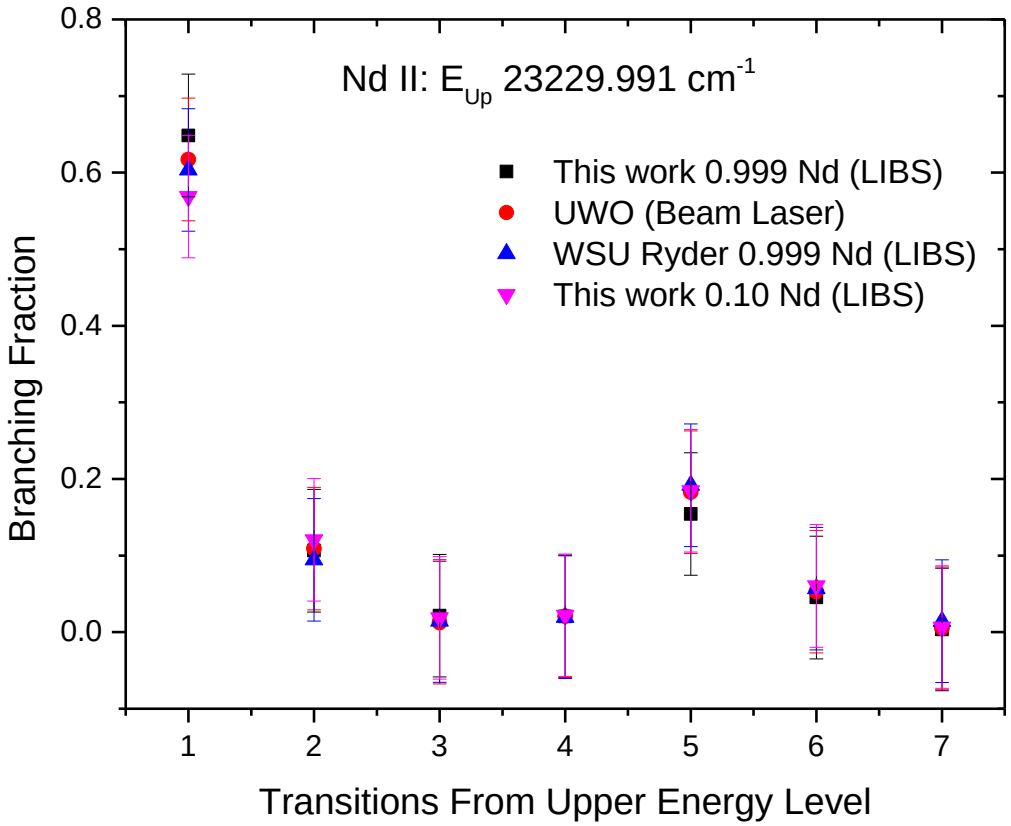

Figure 4.11 Measurements with a 99.9% Nd target and 10% Nd target (thus changing the ion density in the plasma) compared with previous measurements. The branching fractions did not change with a decrease in ion density and both agreed with previous measurements of a beam-laser study (UWO [2]) and previous LIBS measurements (WSU Ryder [3]).

References

[1] Lawler, J. E., Bilty, K. A., & Den Hartog, E. A. (2011). Atomic transition probabilities of Gd i. *Journal of Physics B: Atomic, Molecular and Optical Physics*, *44*(9), 095001.

[2] Li, R., Rehse, S. J., Scholl, T. J., Sharikova, A., Chatelain, R., Holt, R. A., & Rosner, S. D. (2007). Fast-ion-beam laser-induced-fluorescence measurements of branching fractions and oscillator strengths in Nd II. *Canadian Journal of Physics*, *85*(12), 1343-1379.

[3] Ryder, C. A. (2012). Oscillator strength measurements in singly-ionized, doubly-ionized, and neutral lanthanides and transition elements (Sm, Nd, Pr, Gd, Cu, and Fe) using laser-induced breakdown.

[4] Malcheva, G., Blagoev, K., Mayo, R., Ortiz, M., Xu, H. L., Svanberg, S., ... & Biémont, E. (2006). Radiative lifetimes and transition probabilities of astrophysical interest in Zr II. *Monthly Notices of the Royal Astronomical Society*, *367*(2), 754-762.

[5] Den Hartog, E. A., Lawler, J. E., Sneden, C., & Cowan, J. J. (2003). Improved laboratory transition probabilities for Nd II and application to the neodymium abundances of the Sun and three metal-poor stars. *The Astrophysical Journal Supplement Series*, *148*(2), 543.

CHAPTER 5: Data and Uncertainty Analysis

In this chapter I will describe the analysis of the LIBS spectral data that allowed for the atomic measurements as well as the uncertainty associated with our atomic measurement method.

5.1 Branching Fractions (Relative Intensities)

Our ESA3000 spectrometer mapped the wavelength range of 200 to 800 nm onto approximately 64,000 useful pixels. Thus each spectrum obtained had 64,000 pixel intensity values with a corresponding calibrated wavelength. In order to determine accurate branching ratios, the relative intensities for all the transitions from the energy level had to be measured simultaneously. The ESA3000 spectrometer software (ESAWIN) had a built in region of interest (ROI) functionality that allowed straightforward calculation of a background subtracted "area under the curve" for any specific spectral feature or several features at the same time. This ROI feature allowed for selection of multiple regions of interest in a spectrum with each region containing only a small sub-set of the full data; approximately 30 intensity values (pixels). For example, if an upper energy level had eight known decay transitions, then I would create a ROI file which only analyzed eight regions each containing 30 total pixels with the center of the pixel range aligned with the known center wavelength of the transition (Figure 5.1). Transition line centers were obtained from a built-in ESA library containing the NIST (National Institutes for Standards and Technology) atomic database [1]. I created ROI files for each upper energy level containing all the known allowed transitions exiting the energy level. Anticipated transitions were obtained from previous measurements and the Kurucz online database [2]. By allowing the ESA software to open the spectrometer raw data with the ROI file, ESA performed a peak finding algorithm on each 30 pixel region of interest, measured a linear background on either side of the peak, and then performed a numerical integration of the background-subtracted peak. A text file was then created that contained only the background subtracted integrated area under each peak (transition), which is the intensity of the transition. Also reported in the

text file was the center wavelength of the peak, the FWHM (in pixels) of the measured peak, and the background.

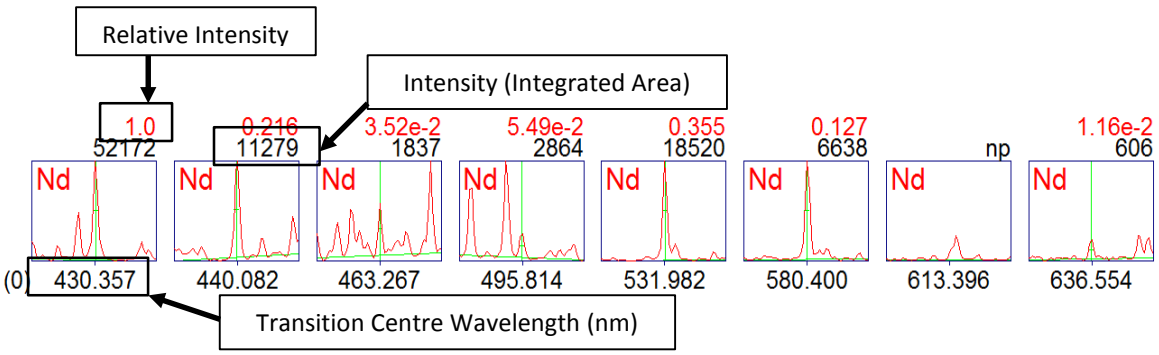

Figure 5.1 An ESAWIN ROI view for one set of branches. Eight regions of interest were identified in the Nd II spectrum containing the eight allowed transitions from the 23,229.991 cm^{-1} upper energy level. The 30 pixels around the known center wavelength of the transition are shown, so the peak is generally in the center of each spectral window. Above the window ESAWIN has calculated the background subtracted integrated area under the curve (intensity in arbitrary units) and the intensity of each peak relative to a user-defined peak (in this case the first peak at 430.357 nm). Below the window is the center wavelength in nanometres as listed in the NIST atomic database.

Using a MATLAB program [see Appendix A] each measured peak intensity (transition intensity) was placed into a Microsoft Excel file with an applied spectral correction factor (to be discussed in Section 5.2), which accounted for the wavelength-dependent attenuation in our system. Ten repeated measurements, each measurement containing the accumulated plasma emission from 100 laser pulses, were obtained for each experimental parameter set for Nd I, II, and III as discussed in Chapter 4. Intensity values were then averaged in the Excel sheet for each of the ten repeated measurements to obtain one intensity value for each transition. Thus each intensity value was determined from the emission of 1000 laser-induced plasmas. By comparing all emission lines from an upper energy level, branching fractions were calculated from the measured intensity of each emission line.

5.2 Measurement Uncertainty

5.2.1 Spectral Correction Factor

In making atomic measurements such as branching fractions, it is imperative that all wavelength dependence of the optical system is taken into account so that the number of photons measured at one wavelength will result in the same measured intensity value as the same number of photons emitted and observed at a different wavelength. The ESA3000 spectrometer has a built in spectral calibration that takes into account the wavelength dependence of the imaging system and optical fibre used to collect the light from the plasma. This spectral calibration was obtained using a calibrated deuterium-tungsten lamp, this was provided by the manufacturer to take into account wavelength-dependent factors. This wavelength calibration is applied to all data automatically.

Since all measurements were obtained inside a vacuum chamber, all light emitted from the plasma first passed through a UV-grade fused silica window that had wavelength-dependent absorption characteristics that needed to be taken into account. Although UV-grade fused silica has excellent transmission in the UV, and a fairly flat absorption curve, these effects were non-negligible. In order to determine the absorption characteristics across our wide range of wavelengths required for branching fraction measurements (the majority of the transitions were between 350 and 600 nm) we used a deuterium-tungsten lamp and compared spectra obtained with and without the window in place (Figure 5.2).

In these experiments, the deuterium-tungsten lamp output fibre was placed up against the UV-grade fused silica window with the spectrometer fibre aligned on the opposite side of the window. Ten repeated measurements were taken with and without the window in place, each with an observation time of 1.5 seconds (250 observations of 6 ms separated by 100 ms due to the ESA3000 control options). A spectral correction factor was calculated by taking the ratio of two averaged spectra. Ten spectra with the window in place were averaged and then divided by the average of ten spectra without the window in place. A piece-wise analytic function was fit to the ratioed data, which resulted in a spectral correction factor which could be

multiplied with our data at each wavelength to account for decreases in the observed emission due to absorption (Figure 5.3). As one can see from Figure 5.3 the UV transmission below 250 nm through our window was very poor, which resulted in a large spectral correction factor with a large uncertainty. Luckily, no emission lines reported in this study were below 250 nm and thus this area of the spectral correction factor could be ignored. The error in the analytic fit to the data was very small but as one can see there is some spread to the data around the fit. In order to take into account uncertainty in the spectral correction factor, an average deviation of the data from the analytic fit was calculated. The average deviation of the spectral ratios from the fit was 4.4%. The spectral correction was also conducted numerous times on multiple days to take into account day-to-day variations in the measured spectral correction factor. This day-to-day scatter (standard deviation) in the measured spectral correction factor was 3.0%.

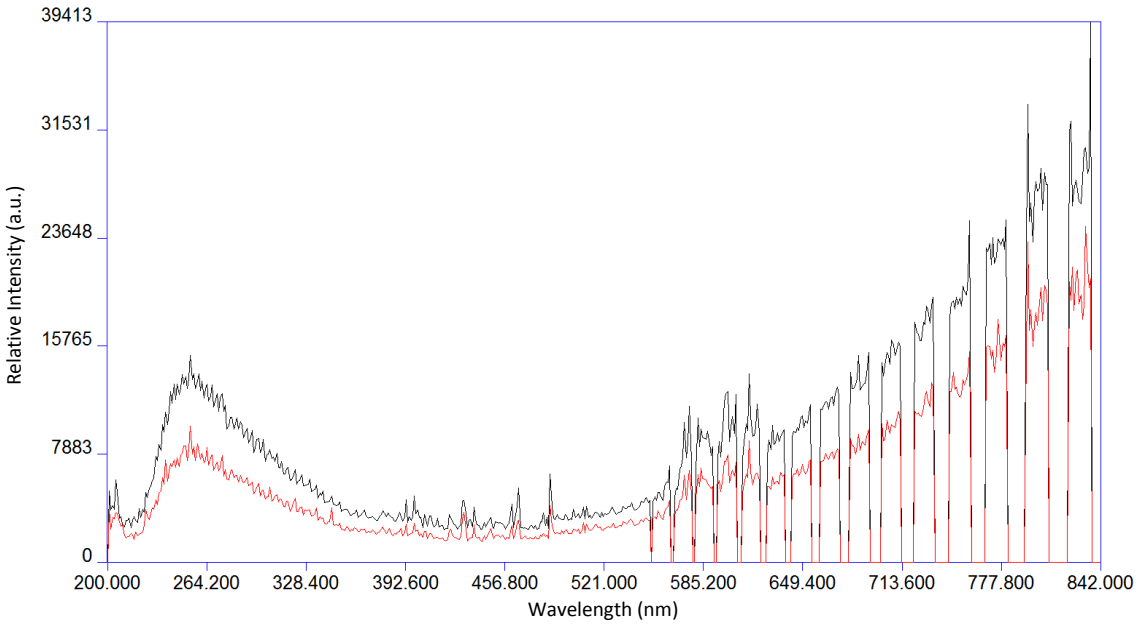

Figure 5.2 Deuterium-tungsten spectra obtained by our ESA3000 spectrometer with (red) and without (black) transmission through our UV-grade fused silica window. The difference between these two spectra can be used to determine a spectral correction factor for the wavelength-dependent attenuation of our system.

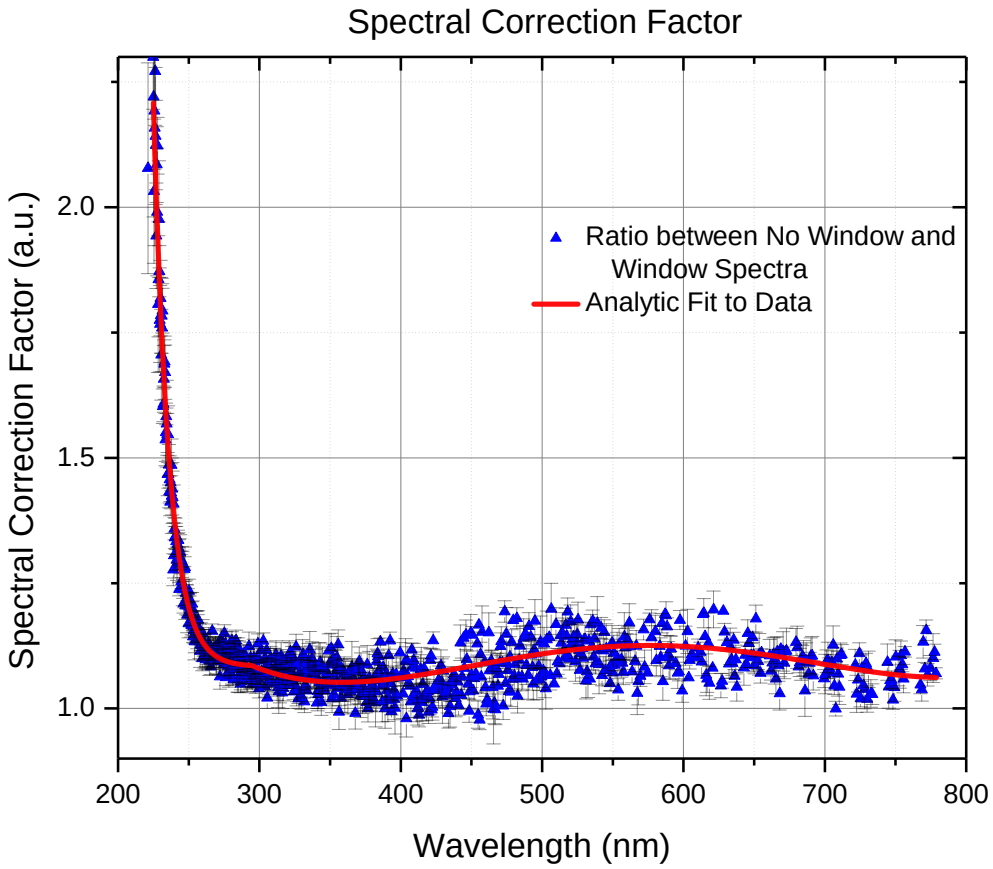

Figure 5.3 The ratio between spectra observed without and with transmission through our UV-grade fused silica window (blue data points) and the resulting spectral correction factor (red line) from an analytic fit to the ratio data. Error bars on the ratio data are the standard deviations of the twenty measured ratios.

5.2.2 Emission Line Uncertainty

There is an intrinsic shot-to-shot scatter in laser-induced plasma measurements as the plasma cannot be perfectly reproduced with every laser pulse due to a multitude of factors that go into creating a laser-induced plasma [3]. This results in a fluctuation in intensity values when repeatedly measuring each transition from an energy level. Ten repeated measurements were obtained and a standard deviation on the intensity values for each transition was calculated. Averaged intensity values were plotted against their fractional standard deviation values (Figure 5.4). From this graph it is easily seen that fractional uncertainty decreased as

the intensity value increased. This is expected as the number of photons observed increases the SNR and SBR, which results in a more reproducible measurement. In order to assign appropriate uncertainty to each intensity measurement it was decided to break all of our measurements up into three regions and to assign an intensity-dependent uncertainty to each group of data. Cut points were chosen to separate the intensity values into groups with intensity values below 2,000 a.u. (small), between 2,000 a.u. and 11,250 a.u. (medium), and above 11,250 a.u. (large). These cut-point values were chosen based on countless hours of reviewing the data, our knowledge of the ability to measure peaks with certain intensity values, and with the aid of Figure 5.4. Ultimately, the uncertainty chosen for each region was calculated with an upper limit approach. The scatter of the uncertainties in each group was measured and the uncertainty assigned to the region was picked so that only $1/e^2$ (~13.5%) of the fractional uncertainty measurements would lie above the cut-off. Thus, 86.5% of the measured fractional uncertainty values were below the uncertainty assigned to the region. 201 measurements were used to obtain these uncertainty values. Using this method, emission lines with intensity values below 2,000 a.u. were all assigned an intensity fractional uncertainty of 24.8%, intensity values between 2,000 and 11,250 a.u. were all assigned an intensity fractional uncertainty of 6.3%, and intensity values above 11,250 a.u. were all assigned an intensity fractional uncertainty of 2.8% (Table 5.1).

One might be tempted to think that because the fractional standard deviation shown in Figure 5.4 is a smoothly-varying function of intensity that it might be best to use some functional form for the uncertainty and then calculate an uncertainty for each intensity. This was investigated and rejected based on thousands more measurements on other elements not shown here. Also, the practical difficulties this would entail in applying this to the tens of thousands of measurements (only neodymium data is reported in my thesis) made on all elements rendered this impractical. Lastly, there is no convincing experimental reason why two intensity values quite close to each other should have different uncertainties and also no reason to use one function over another. This suggests a single value of uncertainty for all measurements, yet a quick analysis of Figure 5.4 shows that clearly large

intensities and small intensities must possess different uncertainties. Therefore this grouping of intensity values was chosen as a compromise.

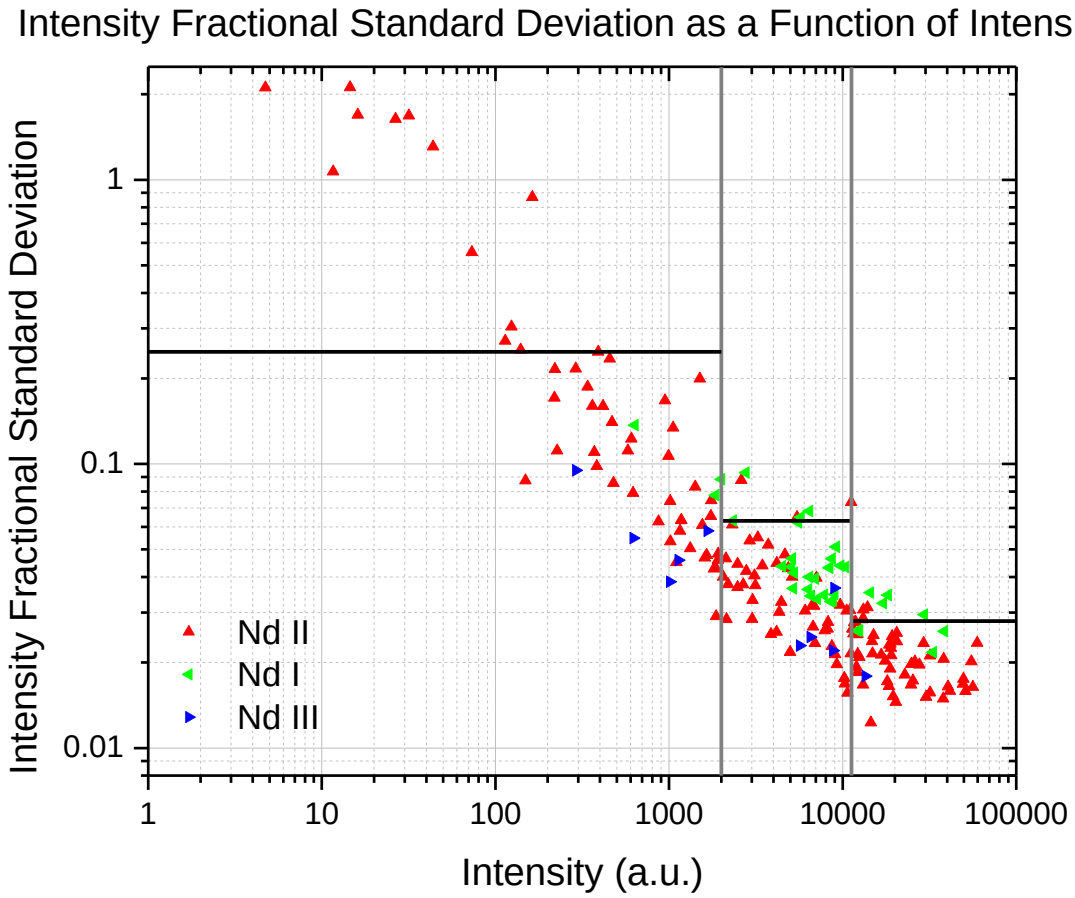

Figure 5.4 Calculated fractional standard deviation of all measured transitions from Nd I, II, and III plotted as a function of intensity. Fractional standard deviation decreased with increasing intensity and thus three groups were chosen for uncertainty assignment based on the measured intensity value. The three intensity groups are shown separated by thick vertical grey lines. The three intensity groups are designated "small intensities" (below 2,000 a.u.), "medium intensities" (between 2,000 a.u. and 11,250 a.u.), and "large intensities" (above 11,250 a.u.). The final fractional uncertainty assigned to each group is shown as a black horizontal line.

5.2.3 Total Uncertainty Budget

The sources of uncertainty described were added in quadrature to produce one final total branch uncertainty value shown in the uncertainty budget table (Table 5.1). Day-to-day scatter of the spectral correction factor was 3.0% and the average

deviation between the analytic fit and the spectral correction was 4.4%. These values were added in quadrature to obtain a 5.3% uncertainty based on our applied spectral correction factor. The three intensity uncertainty measurements based on the fluctuation in measured intensity values in repeated measurements obtained from the analysis of Figure 5.4 are listed in Table 5.1 as "Transition Intensity Uncertainty." This "Transition Intensity Uncertainty" was then added in quadrature with the systematic spectral correction factor uncertainty to calculate a total uncertainty for each of the three intensity groups.

Using the measured branching fractions, previously measured lifetimes, and multiplicity of each upper energy level, gA values for every observed transition were then calculated as described in Chapter 1. The uncertainty assigned to each of our gA measurements came from propagating the uncertainty on our measured branching fraction as shown in Table 5.1 and the reported uncertainty in the previously measured lifetimes.

Source of Uncertainty	**Uncertainty (%)**		
Spectral Correction Factor			
Day-To-Day Scatter		3.0	
Deviation Between Fit and Data		4.4	
Spectral Correction Factor Total		5.3	
Transition Intensity Group	*Small*	*Medium*	*Large*
Transition Intensity Uncertainty	24.8	6.3	2.8
Total Uncertainty	**25.4**	**8.2**	**6.0**

Table 5.1 Uncertainty budget showing the two uncertainties associated with the spectral correction factor added in quadrature for a total uncertainty in the spectral correction factor. The uncertainty for each transition intensity group was then added in quadrature with the uncertainty from the spectral correction factor to produce a total branch uncertainty dependent on each transition's intensity.

References

[1] Kramida, A., Ralchenko, Yu., Reader, J. and NIST ASD Team (2014). *NIST Atomic Spectra Database* (version 5.1), [Online]. Available: http://physics.nist.gov/asd [Wednesday, 5-Mar-2014 15:02:23 EST]. National Institute of Standards and Technology, Gaithersburg, MD.

[2] Kurucz, R. L. & Bell, B. (1995). *Atomic Line Data. Kurucz CD-ROM No. 23.* Cambridge, Mass.: Smithsonian Astrophysical Observatory.

[3] Singh, J. P., & Thakur, S. N. (Eds.). (2007). *Laser-induced breakdown spectroscopy*. Elsevier.

CHAPTER 6: Neodymium Transition Probability Measurements

Using our laser-induced breakdown spectroscopy setup for atomic measurements, I obtained relative intensity measurements on doubly-ionized, singly-ionized, and neutral neodymium. In this chapter, I present my measurements and results of neodymium transition probabilities. Data was taken on three other lanthanides (praseodymium, gadolinium, and samarium) but will not be presented in this thesis since the data will be used in future work (see Chapter 8).

6.1 Neutral Neodymium

6.1.1 Previous Neutral Neodymium Work

Currently, there is limited previous work on transition probability measurements in neutral neodymium (Nd I). In 1962, Corliss and Bozman [1] determined transition probabilities using arc discharge measurements. In 1973, Penkin and Komarovskii [2] determined relative intensities for Nd I. In 1980, Marek and Stahnke [3] determined 18 radiative lifetimes using delayed coincidence and laser-induced fluorescence. In 1982, Gorshkov et al. [4] determined 38 radiative lifetimes using pulsed-electron delayed coincidence. In 2004, Biémont et al. [5] determined 15 radiative lifetimes using time-resolved laser-induced fluorescence. Most recently, in 2011, Den Hartog et al. [6] determined 100 radiative lifetimes using a beam-laser ion source. The previously measured radiative lifetimes we used to determine our Nd I transition probabilities were from Den Hartog et al. unless otherwise noted. This limited amount of previous work offered very little for comparison of our determined transition probabilities.

6.1.2 Neutral Neodymium Results

Experimental parameters were optimized for neutral neodymium emission as discussed in Chapter 4. Each spectrum obtained consisted of 100 laser pulses, each on a different location on our neodymium target. The observation time of the plasma was 3 μs after formation and was 10 μs in length in argon gas at a pressure of 1 Torr. The majority of known energy levels in Nd I only have one transition, thus measuring

that transition and reporting the results provides no new information since previously measured lifetimes were used in our calculations (there are hundreds of energy levels with one transition in Nd I). Only energy levels with more than one transition are reported on although nearly all of the energy levels with only one transition were observed. In comparison with the previous LIBS work of Ryder [7], Ryder made transition probability measurements on 8 upper energy levels (containing more than one transition). With my new setup I made measurements on 16 upper energy levels. Not only was I able to measure twice the number of energy levels, but emission on all transitions increased substantially in Nd I which greatly improved our measurement accuracy on small emission lines. I increased plasma emission and light capture efficiency to sufficiently bring many emission lines to measurable levels and increased the accuracy of all emission lines. Comparison of our transition probabilities with previous works was virtually useless, as my calculations used more recent radiative lifetimes. I used the radiative lifetime measurements from Biémont et al. in 2011, whereas all previous transition probabilities were calculated using values from before 2011. This in turn skews the results for comparison with previous works. See Table 6.1 for a full list of Nd I results.

6.2 Singly-Ionized Neodymium

6.2.1 Previous Singly-Ionized Neodymium Work

In 1977, Maier and Whaling [8] determined 9 transition probabilities in Nd II by using determined radiative lifetimes from Andersen et al. [9] (1975). In 1984, Ward et al. [10] determined 8 radiative lifetimes. In 2001, Pinciuc et al. [11] determined 35 radiative lifetimes using a collinear beam-laser method with laser-induced fluorescence. In 2002, Scholl et al. [12] determined 13 lifetimes using beam-laser laser-induced fluorescence. In 2003, Xu at al. [13] determined 107 transition probabilities from 24 energy levels using laser-induced fluorescence. Again in 2003, Den Hartog et al. [14] determined transition probabilities for more than 700 transitions in 168 levels using time-resolved laser-induced fluorescence. In 2007, Biémont et al. [15] compared previously experimentally determined with calculated lifetimes from various theoretical methods. Again in 2007, Li et al. [16] determined

430 transition probabilities from 46 energy levels using fast-ion beam laser-induced fluorescence. This amount of previous work provides sufficient results for comparison with my transition probability measurements.

6.2.2 Singly-Ionized Neodymium Results

Experimental parameters were optimized for singly-ionized neodymium emission as discussed in Chapter 4. Each spectrum obtained consisted of 100 laser pulses, each on a different location on our neodymium target. The observation time of the plasma was 1 μs after formation and was 1 μs in length in argon gas at a pressure of 1 Torr. My results for Nd II are very similar to the results of Ryder as the Ryder experimental parameters were optimized for Nd II as well. With my improvements in the experimental apparatus, measurement of smaller emission lines greatly improved. This in turn improved the accuracy of all upper energy levels containing smaller emission lines since branching fractions are determined with the total sum of all the emission lines. Full results are listed in Table 6.2 along with comparison graphs between previous works seen below (Figure 6.1 and Figure 6.2). Figure 6.1 shows the agreement between my measured transition probabilities and the previous works of Ryder [7] and Li et al. [16]. Figure 6.2 is a histogram showing the deviation between Li et al. and this work's transition probabilities.

6.3 Doubly-Ionized Neodymium

6.3.1 Previous Doubly-Ionized Neodymium Work

The only experimentally determined data for Nd III was in 2002 with the measurement of radiative lifetimes in 5 energy levels by Zhang et al. [17] using laser-induced fluorescence. There is very little work in Nd III even in terms of known energy levels and transitions.

6.3.2 Doubly-Ionized Neodymium Results

In my measurement of Nd III, a tremendous number of new lines were observed, but current knowledge on upper energy levels and transitions in Nd III is very limited, and thus only known transitions from the DREAM database [18] were reported on. Many emission lines are currently unidentified (the unidentified lines could be higher ionization states as well, but no Nd IV, V, … lines have been previously

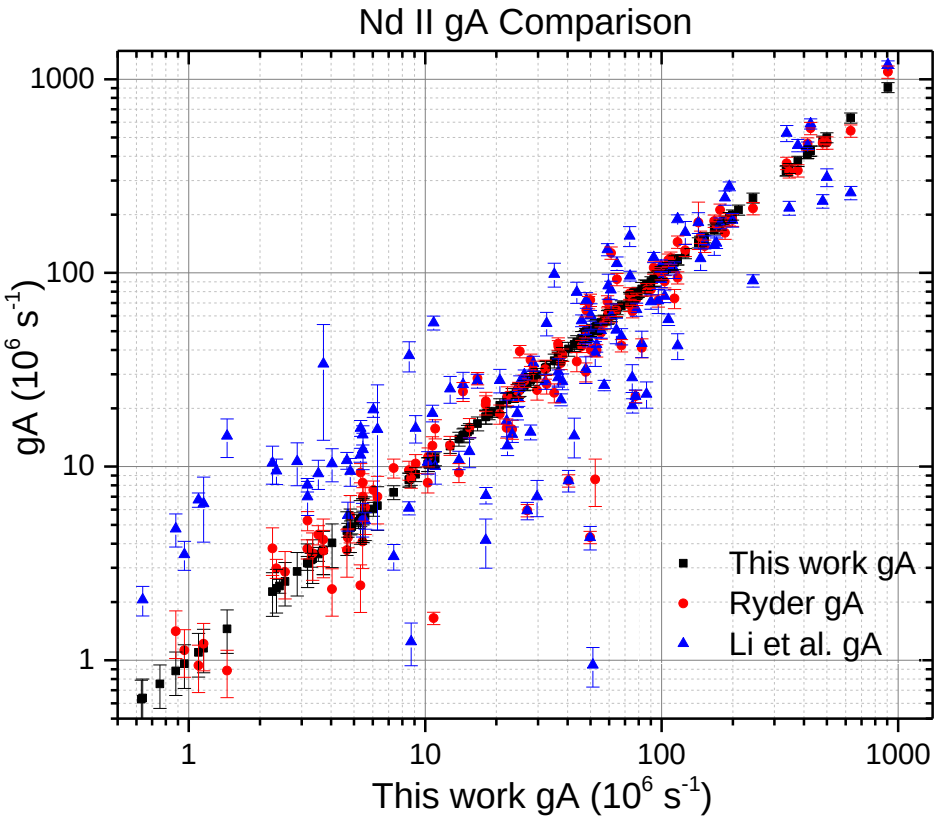

Figure 6.1 Comparison between this work's measured transition probabilities (gA values) and previous LIBS work of Ryder [7] and beam-laser work of Li et al. [16].

documented). Observed emission lines were substantial in size in comparison to the previous work by Ryder. This was evident from energy levels with two transitions where Ryder only observed the stronger of the two whereas I observed both transitions because of my increased light collection and optimized experimental conditions. This was observed in Nd I, Nd II, and Nd III comparisons with Ryder. Experimental parameters were optimized for doubly-ionized neodymium emission as discussed in Chapter 4. Each spectrum obtained consisted of 100 laser pulses, each on a different location on our neodymium target. The observation time of the plasma was 500 ns after formation and was 500 ns in length in argon gas at a pressure of 1 Torr. Ryder was only able to make a measurement on one upper energy level with more than one transition in Nd III. I was able to increase that number to 4 although the main limitation was the amount of known upper energy levels and transitions in

Nd III. No comparison with previous works was possible. Table 6.3 shows full results for Nd III measurements and transition probabilities.

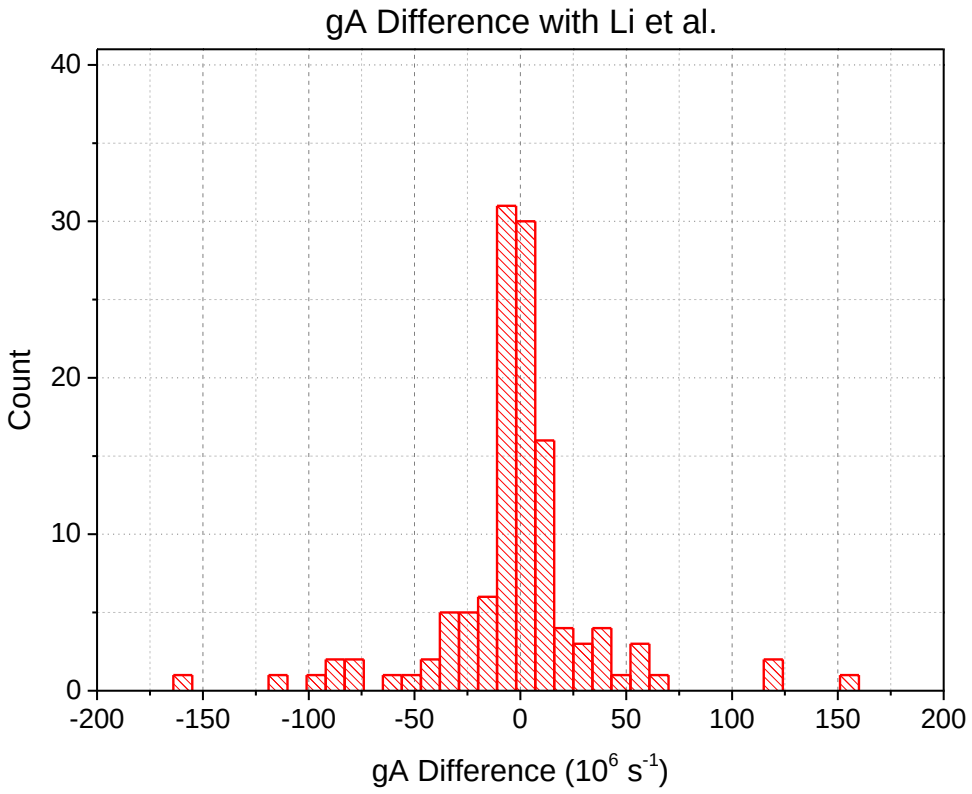

Figure 6.2 A histogram of transition probability differences between this work and Li et al. [16]. Percent gA difference was not used as this results in a skew of the data. Specifically, when small gA values are different between the two studies (which we know to be common as the accuracy of both studies decreased with small intensities) very large percent differences can result that are due to only small absolute gA differences. Percent differences also result in a skew of the histogram based on the fact that one cannot obtain a negative percent difference larger than 100%, whereas a positive percent difference greater than 100% is possible.

Upper Energy Level (cm^{-1})	Transition λ (nm)	Intensity (a.u.)	Branching Fraction	Lifetime (ns)	This work's g_kA_{ki} (10^6 s^{-1}) Value	Ryder g_kA_{ki} (10^6 s^{-1}) Value [7]	Kurucz g_kA_{ki} (10^6 s^{-1}) Value [18]	Gorshkov g_kA_{ki} (10^6 s^{-1}) Value [4]
18741.337	533.432	6425	0.179 ± 0.015	81	19.9 ± 1.92	14.47 ± 1.66	15.8	155.13
	567.596	29479	0.821 ± 0.049	81	91.2 ± 7.12	102.43 ± 10.82	119.68	70.02
19209.262	520.437	8800	0.635 ± 0.052	229	24.9 ± 2.40		42.08	76.34
	552.907	5067	0.365 ± 0.030	229	14.4 ± 1.38		22.01	110.49
19700.856	507.451	5129	0.719 ± 0.059	300b	26.4 ± 3.09		26.67	105.29
	576.732	2001	0.281 ± 0.023	300b	10.3 ± 1.21		32.7	0
20360.673	491.006	17142	0.723 ± 0.043	81.3	80.0 ± 6.24		84.66	128.42
	519.805	6583	0.277 ± 0.023	81.3	30.7 ± 2.96		63	160.96
20541.833	486.676	33181	0.840 ± 0.050	77.8	118.7 ± 9.27	136.75 ± 13.87	80.78	159.39
	514.955	6340	0.160 ± 0.013	77.8	22.7 ± 2.18	4.64 ± 2.39	83.05	174.08
20839.206	507.186	6432	0.360 ± 0.030	127	36.8 ± 3.55		72.45	160.12
	541.192	4483	0.251 ± 0.021	127	25.7 ± 2.47		25.53	0
	582.674	6957	0.389 ± 0.032	127	39.8 ± 3.84		67.95	116.4
21314.254	495.250	8383	0.447 ± 0.037	101	57.5 ± 5.54	19.44 ± 7.82	75.98	167.93
	566.975	10387	0.553 ± 0.046	101	71.2 ± 6.86	109.27 ± 11.54	179.4	183.02
21314.439	469.034	18267	0.685 ± 0.041	69.9	88.3 ± 6.89	102.49 ± 10.82	114.66	198.61
	495.245	8383	0.315 ± 0.026	69.9	40.5 ± 3.90	26.27 ± 3.01	109.75	0
21543.326	489.693	38478	0.755 ± 0.045	16	613.5 ± 47.89	528.98 ± 55.85	646.36	431.37
	521.320	12485	0.245 ± 0.015	16	199.0 ± 15.54	283.52 ± 29.94	245.31	0
21558.796	463.718	8990	0.384 ± 0.032	74.6	56.6 ± 5.45	34.84 ± 3.99	31.93	126.09
	489.322	14420	0.616 ± 0.037	74.6	90.8 ± 7.09	112.61 ± 11.89	119.35	192.79
22010.34	454.205	12152	0.609 ± 0.037	95.2	57.6 ± 4.49		69.72	166.09
	478.741	7799	0.391 ± 0.032	95.2	37.0 ± 3.56		39.16	111.53
22049.736	477.840	5262	0.478 ± 0.039	173	35.9 ± 3.46		35.03	125.46
	507.908	5741	0.522 ± 0.043	173	39.2 ± 3.78		115.43	0

Upper Energy Level (cm^{-1})	Transition λ (nm)	Intensity (a.u.)	Branching Fraction	Lifetime (ns)	This work's g_kA_{ki} (10^6 s^{-1}) Value	Ryder g_kA_{ki} (10^6 s^{-1}) Value [7]	Kurucz g_kA_{ki} (10^6 s^{-1}) Value [18]	Gorshkov g_kA_{ki} (10^6 s^{-1}) Value [4]
22736.693	462.648	9749	0.529 ± 0.044	82c	71.0 ± 9.06	18.48 ± 2.62	82.29	174.66
	490.779	8670	0.471 ± 0.039	82c	63.1 ± 8.06	115.66 ± 15.59	101.08	0
25746.414	526.663	2336	0.171 ± 0.014	29.2	76.2 ± 7.34		126.13	
	529.166	8539	0.626 ± 0.052	29.2	278.7 ± 26.85		506	
	589.946	2765	0.203 ± 0.017	29.2	90.3 ± 8.69		123.67	
26333.118	557.550	5548	0.362 ± 0.030	28.6	215.1 ± 20.72	313.25 ± 33.08	222.3	
	600.765	9152	0.597 ± 0.049	28.6	354.7 ± 34.17	273.51 ± 28.88	289.8	
	642.984	634	0.041 ± 0.010	28.6	24.6 ± 6.36	7.64 ± 6.07	47.58	
27785.804	560.191	7150	0.503 ± 0.041	17.2	439.0 ± 42.28		464.7	
	599.475	5203	0.366 ± 0.030	17.2	319.4 ± 30.77		320.71	
	635.593	1852	0.130 ± 0.011	17.2	113.7 ± 10.95		106.55	

Table 6.1 Radiative parameters for Nd I. Lifetimes adopted from Den Hartog et al. [6] unless noted.
b lifetime from Gorshkov et al. [4]
c lifetime from Biemont et al. [5]

Upper Energy Level (cm^{-1})	Transition λ (nm)	Intensity (a.u.)	Branching Fraction	Lifetime (ns)	This work's g_kA_{ki} (10^6 s^{-1}) Value	Ryder g_kA_{ki} (10^6 s^{-1}) Value [7]	Li et al. g_kA_{ki} (10^6 s^{-1}) Value [16]	Hartog et al. g_kA_{ki} (10^6 s^{-1}) Value [14]
22696.885	450.659	11014	0.256 ± 0.021	80.6	38.11 ± 3.14	37.73 ± 2.75	27.52 ± 2.60	29.76 ± 1.68
	470.971	10550	0.245 ± 0.020	80.6	36.50 ± 3.01	43.09 ± 3.15	28.79 ± 2.72	32.40 ± 1.80
	475.002	0	0.000 ± 0.000	80.6		42.34 ± 4.78	9.10 ± 0.93	10.92 ± 0.72
	497.092	3140	0.073 ± 0.006	80.6	10.87 ± 0.89	1.65 ± 0.12	55.29 ± 4.59	63.48 ± 3.24
	509.280	14783	0.344 ± 0.021	80.6	51.15 ± 3.07		0.95 ± 0.22	
	547.514	0	0.000 ± 0.000	80.6		14.24 ± 1.61	5.24 ± 0.58	3.84 ± 0.72
	580.923	1414	0.033 ± 0.003	80.6	4.89 ± 0.40			
	634.139	2127	0.049 ± 0.004	80.6	7.36 ± 0.61	9.83 ± 1.11	3.44 ± 0.52	3.18 ± 0.31
	700.257	0	0.000 ± 0.000	80.6			2.24 ± 0.81	
	749.478	0	0.000 ± 0.000	80.6			1.53 ± 0.69	
	779.835	0	0.000 ± 0.000	80.6			6.46 ± 2.58	
	808.854	0	0.000 ± 0.000	80.6			2.15 ± 1.03	
	850.478	0	0.000 ± 0.000	80.6			6.17 ± 3.46	1.91 ± 0.25
22850.552	437.503	24958	0.612 ± 0.037	85.6	57.18 ± 3.43	55.28 ± 4.04	26.27 ± 1.62	27.84 ± 1.68
	447.558	3725	0.091 ± 0.008	85.6	8.54 ± 0.70	9.58 ± 1.08	6.11 ± 0.48	
	471.559	11451	0.281 ± 0.017	85.6	26.23 ± 1.57	27.65 ± 2.02	29.82 ± 1.75	37.92 ± 2.00
	593.474	0	0.000 ± 0.000	85.6			4.65 ± 0.39	
	652.314	480	0.012 ± 0.003	85.6	1.10 ± 0.28	0.94 ± 0.26	6.74 ± 0.57	
	692.799	0	0.000 ± 0.000	85.6			3.36 ± 0.39	
	711.336	16	0.000 ± 0.000	85.6	0.04 ± 0.01		0.39 ± 0.07	
	732.284	0	0.000 ± 0.000	85.6			1.15 ± 0.17	
	758.764	0	0.000 ± 0.000	85.6			3.77 ± 0.53	
	772.472	163	0.004 ± 0.001	85.6	0.37 ± 0.09		1.82 ± 0.34	
	820.539	0	0.000 ± 0.000	85.6			5.14 ± 0.72	
	835.660	0	0.000 ± 0.000	85.6			4.25 ± 0.63	
23229.991	430.357	55182	0.551 ± 0.033	13.3	414.55 ± 24.85	464.05 ± 33.88	453.73 ± 20.09	437.00 ± 23.00
	440.082	12008	0.120 ± 0.007	13.3	90.21 ± 5.41	82.06 ± 5.99	71.05 ± 6.07	86.00 ± 5.00
	463.267	1849	0.018 ± 0.002	13.3	13.89 ± 1.14	9.32 ± 1.05	10.82 ± 1.18	9.40 ± 0.70
	495.814	3106	0.031 ± 0.003	13.3	23.33 ± 1.92	15.58 ± 1.76	14.68 ± 1.35	15.50 ± 1.00
	531.982	20257	0.202 ± 0.012	13.3	152.17 ± 9.12	137.47 ± 10.04	144.20 ± 11.29	172.00 ± 13.00
	580.400	7064	0.071 ± 0.006	13.3	53.06 ± 4.37	39.70 ± 2.90	42.72 ± 3.72	59.00 ± 5.00
	613.396	0	0.000 ± 0.000	13.3			3.91 ± 0.48	
	636.554	621	0.006 ± 0.002	13.3	4.66 ± 1.18	3.70 ± 1.02	10.77 ± 1.08	10.30 ± 1.20

Upper Energy Level (cm^{-1})	Transition λ (nm)	Intensity (a.u.)	Branching Fraction	Lifetime (ns)	This work's g_kA_{ki} (10^6 s^{-1}) Value	Ryder g_kA_{ki} (10^6 s^{-1}) Value [7]	Li et al. g_kA_{ki} (10^6 s^{-1}) Value [16]	Hartog et al. g_kA_{ki} (10^6 s^{-1}) Value [14]
23397.385	427.278	13896	0.313 ± 0.019	66.6	37.54 ± 2.25	34.22 ± 2.50	22.16 ± 1.56	26.48 ± 1.36
	436.863	17619	0.396 ± 0.024	66.6	47.60 ± 2.85	49.88 ± 3.64	45.59 ± 2.48	54.40 ± 2.40
	459.701	9074	0.204 ± 0.017	66.6	24.51 ± 2.02	24.63 ± 1.80	18.82 ± 1.38	22.56 ± 1.20
	574.814	1175	0.026 ± 0.002	66.6	3.17 ± 0.26	3.76 ± 0.43	8.04 ± 0.65	
	629.841	870	0.020 ± 0.005	66.6	2.35 ± 0.60	2.99 ± 0.34	9.51 ± 1.43	6.32 ± 0.56
	684.696	1742	0.039 ± 0.003	66.6	4.71 ± 0.39	4.29 ± 0.48	5.60 ± 0.96	
	704.083	15	0.000 ± 0.000	66.6	0.04 ± 0.01	0.13 ± 0.04	1.63 ± 0.17	
	728.528	73	0.002 ± 0.000	66.6	0.20 ± 0.05	0.22 ± 0.06	6.04 ± 1.15	
	741.156	0	0.000 ± 0.000	66.6			1.36 ± 0.16	
	798.878	0	0.000 ± 0.000	66.6			1.37 ± 0.22	
	799.133	0	0.000 ± 0.000	66.6				
23357.387	424.737	18085	0.311 ± 0.019	26.6	116.99 ± 7.01	144.40 ± 10.54	190.55 ± 9.00	227.00 ± 12.00
	434.206	11655	0.201 ± 0.012	26.6	75.40 ± 4.52	63.23 ± 4.62	20.67 ± 1.75	23.20 ± 1.60
	453.033	2792	0.048 ± 0.004	26.6	18.06 ± 1.49	21.75 ± 2.46	7.10 ± 0.69	
	456.761	4317	0.074 ± 0.006	26.6	27.93 ± 2.30	35.52 ± 2.59	15.07 ± 1.33	15.80 ± 1.00
	488.369	4178	0.072 ± 0.006	26.6	27.03 ± 2.23	5.94 ± 0.43	5.92 ± 0.61	
	523.419	12104	0.208 ± 0.012	26.6	78.30 ± 4.69	73.26 ± 5.35	64.72 ± 5.05	74.00 ± 5.00
	570.244	4982	0.086 ± 0.007	26.6	32.23 ± 2.65	31.85 ± 3.60	27.50 ± 2.45	27.30 ± 2.10
	624.334	0	0.000 ± 0.000	26.6			9.60 ± 1.35	3.50 ± 0.40
	697.207	0	0.000 ± 0.000	26.6			2.82 ± 0.69	
	731.852	0	0.000 ± 0.000	26.6			2.39 ± 0.70	
	733.542	0	0.000 ± 0.000	26.6				
	790.039	0	0.000 ± 0.000	26.6				
	845.236	0	0.000 ± 0.000	26.6				
23857.278	428.257	31912	0.427 ± 0.026	66.1	77.57 ± 4.65	23.07 ± 1.68	23.08 ± 1.82	22.32 ± 1.68
	446.560	10332	0.138 ± 0.011	66.1	25.11 ± 2.07	39.31 ± 2.87	27.27 ± 2.12	26.64 ± 1.92
	450.181	20555	0.275 ± 0.016	66.1	49.96 ± 2.99	72.36 ± 5.28	60.15 ± 3.86	68.40 ± 4.80
	516.792	2482	0.033 ± 0.003	66.1	6.03 ± 0.50	7.57 ± 0.86	19.68 ± 1.71	16.44 ± 1.56
	544.226	6849	0.092 ± 0.008	66.1	16.65 ± 1.37	28.52 ± 2.08	27.66 ± 2.28	
	590.662	2194	0.029 ± 0.002	66.1	5.33 ± 0.44	9.30 ± 1.05	15.80 ± 1.48	
	647.618	363	0.005 ± 0.001	66.1	0.88 ± 0.22	1.41 ± 0.39	4.77 ± 0.93	
	715.106	0	0.000 ± 0.000	66.1			3.13 ± 0.74	
24053.354	415.626	49447	0.590 ± 0.035	74.3	79.47 ± 4.76			

Upper Energy Level (cm^{-1})	Transition λ (nm)	Intensity (a.u.)	Branching Fraction	Lifetime (ns)	This work's g_kA_{ki} (10^6 s^{-1}) Value	Ryder g_kA_{ki} (10^6 s^{-1}) Value [7]	Li et al. g_kA_{ki} (10^6 s^{-1}) Value [16]	Hartog et al. g_kA_{ki} (10^6 s^{-1}) Value [14]
	424.689	3248	0.039 ± 0.003	74.3	5.22 ± 0.43			
	442.682	2050	0.024 ± 0.002	74.3	3.29 ± 0.27			
	446.241	11561	0.138 ± 0.008	74.3	18.58 ± 1.11			
	476.362	11875	0.142 ± 0.009	74.3	19.09 ± 1.14			
	509.652	3011	0.036 ± 0.003	74.3	4.84 ± 0.40			
	553.922	1505	0.018 ± 0.001	74.3	2.42 ± 0.20			
	583.898	470	0.006 ± 0.001	74.3	0.76 ± 0.19			
	604.845	392	0.005 ± 0.001	74.3	0.63 ± 0.16			
	639.495	0	0.000 ± 0.000	74.3				
	705.214	140	0.002 ± 0.000	74.3	0.22 ± 0.06			
	746.813	44	0.001 ± 0.000	74.3	0.07 ± 0.02			
	749.810	0	0.000 ± 0.000	74.3				
	762.489	0	0.000 ± 0.000	74.3				
	809.906	0	0.000 ± 0.000	74.3				
	830.899	0	0.000 ± 0.000	74.3				
	835.459	0	0.000 ± 0.000	74.3				
	844.994	0	0.000 ± 0.000	74.3				
	845.745	0	0.000 ± 0.000	74.3				
	848.871	0	0.000 ± 0.000	74.3				
24134.095	423.237	18616	0.204 ± 0.012	24.6	99.50 ± 5.96	107.31 ± 7.83	109.13 ± 7.51	126.00 ± 10.80
	441.105	19264	0.211 ± 0.013	24.6	102.97 ± 6.17	90.30 ± 6.59	75.87 ± 5.61	86.40 ± 7.20
	444.638	31888	0.349 ± 0.021	24.6	170.44 ± 10.22	177.52 ± 12.96	142.54 ± 9.07	150.00 ± 12.00
	463.937	4170	0.046 ± 0.004	24.6	22.29 ± 1.83	23.22 ± 2.62	12.83 ± 1.42	11.52 ± 0.96
	507.562	1018	0.011 ± 0.003	24.6	5.44 ± 1.38	4.10 ± 1.13	5.39 ± 1.07	
	536.147	11415	0.125 ± 0.007	24.6	61.01 ± 3.66	59.69 ± 4.36	81.71 ± 8.91	
	551.455	0	0.000 ± 0.000	24.6			2.76 ± 0.93	
	581.157	3870	0.042 ± 0.003	24.6	20.68 ± 1.70	18.67 ± 2.11	27.87 ± 3.86	27.24 ± 3.12
	636.209	1020	0.011 ± 0.003	24.6	5.45 ± 1.38	6.99 ± 0.79	12.25 ± 2.60	
	724.597	5	0.000 ± 0.000	24.6	0.03 ± 0.01		17.43 ± 6.19	
24321.262	411.047	16690	0.259 ± 0.016	51.7	50.18 ± 3.01	40.01 ± 2.92	60.25 ± 9.08	77.00 ± 4.00
	419.910	5122	0.080 ± 0.007	51.7	15.40 ± 1.27	15.89 ± 1.80	11.96 ± 2.10	11.40 ± 0.80
	437.492	24958	0.388 ± 0.023	51.7	75.04 ± 4.50	71.14 ± 5.19	28.83 ± 4.72	29.30 ± 1.70
	470.357	12173	0.189 ± 0.011	51.7	36.60 ± 2.19	41.65 ± 3.04	30.88 ± 5.16	30.50 ± 1.90
	502.785	3033	0.047 ± 0.004	51.7	9.12 ± 0.75	10.38 ± 1.17	15.79 ± 2.54	17.20 ± 1.30

Upper Energy Level (cm^{-1})	Transition λ (nm)	Intensity (a.u.)	Branching Fraction	Lifetime (ns)	This work's g_kA_{ki} (10^6 s^{-1}) Value	Ryder g_kA_{ki} (10^6 s^{-1}) Value [7]	Li et al. g_kA_{ki} (10^6 s^{-1}) Value [16]	Hartog et al. g_kA_{ki} (10^6 s^{-1}) Value [14]
	545.820	0	0.000 ± 0.000	51.7		4.49 ± 1.23	4.50 ± 0.85	
	574.820	1175	0.018 ± 0.002	51.7	3.53 ± 0.29	4.45 ± 0.50	9.21 ± 1.58	7.90 ± 0.80
	628.721	1058	0.016 ± 0.004	51.7	3.18 ± 0.81	5.26 ± 0.59	6.99 ± 1.40	4.50 ± 0.50
	693.646	0	0.000 ± 0.000	51.7			9.56 ± 2.23	4.30 ± 0.60
	732.160	124	0.002 ± 0.000	51.7	0.37 ± 0.09	0.16 ± 0.05	2.57 ± 0.85	
	735.041	0	0.000 ± 0.000	51.7				
	826.283	0	0.000 ± 0.000	51.7				
24445.389	417.732	30277	0.252 ± 0.015	15.62	193.27 ± 11.58	188.39 ± 13.75	280.30 ± 14.84	302.40 ± 16.80
	435.128	38191	0.317 ± 0.019	15.62	243.78 ± 14.61	215.16 ± 15.71	91.19 ± 6.67	86.40 ± 6.00
	438.566	27693	0.230 ± 0.014	15.62	176.77 ± 10.60	211.45 ± 15.44	180.48 ± 11.59	175.20 ± 10.80
	499.665	1607	0.013 ± 0.001	15.62	10.26 ± 0.84	8.24 ± 0.93	10.55 ± 1.41	
	527.343	9253	0.077 ± 0.006	15.62	59.07 ± 4.86	71.12 ± 5.19	132.10 ± 9.57	157.20 ± 12.00
	542.146	4653	0.039 ± 0.003	15.62	29.70 ± 2.45	24.82 ± 2.80	7.00 ± 1.49	
	570.827	8680	0.072 ± 0.006	15.62	55.41 ± 4.56	49.07 ± 3.58	50.52 ± 4.48	
	623.850	0	0.000 ± 0.000	15.62			16.10 ± 2.94	
25080.880	406.927	19562	0.213 ± 0.013	39.5	64.67 ± 3.88	92.66 ± 6.76	111.90 ± 9.08	106.80 ± 10.80
	423.417	15077	0.164 ± 0.010	39.5	49.85 ± 2.99	4.31 ± 0.31	4.31 ± 0.60	
	426.671	14852	0.162 ± 0.010	39.5	49.10 ± 2.94	70.42 ± 5.14	45.81 ± 4.29	39.60 ± 3.60
	444.411	5459	0.059 ± 0.005	39.5	18.05 ± 1.49	20.82 ± 2.35	4.17 ± 1.18	3.17 ± 0.36
	454.127	14539	0.158 ± 0.009	39.5	48.07 ± 2.88	64.02 ± 4.67	72.43 ± 6.72	58.80 ± 6.00
	484.284	290	0.003 ± 0.001	39.5	0.96 ± 0.24	1.13 ± 0.31	3.52 ± 0.60	
	486.048	0	0.000 ± 0.000	39.5				
	510.239	20466	0.223 ± 0.013	39.5	67.66 ± 4.06	42.18 ± 3.08	47.07 ± 4.54	
	550.840	1647	0.018 ± 0.001	39.5	5.44 ± 0.45	8.25 ± 0.93	14.58 ± 1.66	
25389.217	393.757	949	0.019 ± 0.005	35.1	5.32 ± 1.35	2.44 ± 0.67	11.48 ± 0.95	12.40 ± 0.70
	401.882	8198	0.161 ± 0.013	35.1	45.94 ± 3.78	41.82 ± 3.05	56.68 ± 3.95	59.00 ± 3.00
	417.958	13118	0.258 ± 0.015	35.1	73.52 ± 4.41	68.06 ± 4.97	96.36 ± 5.62	87.00 ± 4.00
	421.129	19078	0.375 ± 0.022	35.1	106.92 ± 6.41	116.53 ± 8.51	57.45 ± 3.99	52.30 ± 2.70
	447.854	993	0.020 ± 0.005	35.1	5.57 ± 1.41	6.15 ± 1.69	5.27 ± 0.51	4.70 ± 0.30
	541.637	4434	0.087 ± 0.007	35.1	24.85 ± 2.05	24.45 ± 2.76	22.44 ± 1.97	
	559.615	1555	0.031 ± 0.003	35.1	8.71 ± 0.72	8.71 ± 0.98	1.25 ± 0.31	
	589.151	1915	0.038 ± 0.003	35.1	10.73 ± 0.88	12.82 ± 1.45	18.88 ± 1.85	
	617.464	114	0.002 ± 0.001	35.1	0.64 ± 0.16	0.25 ± 0.07	2.05 ± 0.36	

Upper Energy Level (cm^{-1})	Transition λ (nm)	Intensity (a.u.)	Branching Fraction	Lifetime (ns)	This work's g_kA_{ki} (10^6 s^{-1}) Value	Ryder g_kA_{ki} (10^6 s^{-1}) Value [7]	Li et al. g_kA_{ki} (10^6 s^{-1}) Value [16]	Hartog et al. g_kA_{ki} (10^6 s^{-1}) Value [14]
	644.483	0	0.000 ± 0.000	35.1		0.16 ± 0.05	4.48 ± 0.64	
	645.793	456	0.009 ± 0.002	35.1	2.55 ± 0.65	2.86 ± 0.79		
	651.923	27	0.001 ± 0.000	35.1	0.15 ± 0.04	0.65 ± 0.18		
	679.049	0	0.000 ± 0.000	35.1			8.56 ± 1.07	
	681.526	0	0.000 ± 0.000	35.1				
25524.485	415.608	49678	0.259 ± 0.016	8.79	412.78 ± 24.74			
	435.816	40450	0.211 ± 0.013	8.79	336.11 ± 20.15			
	445.156	51094	0.267 ± 0.016	8.79	424.55 ± 25.45			
	460.222	1755	0.009 ± 0.001	8.79	14.58 ± 1.20			
	498.942	11218	0.059 ± 0.005	8.79	93.21 ± 7.67			
	529.316	25435	0.133 ± 0.008	8.79	211.35 ± 12.67			
	568.852	10235	0.053 ± 0.004	8.79	85.04 ± 7.00			
	618.390	1816	0.009 ± 0.001	8.79	15.09 ± 1.24			
26274.095	388.077	18498	0.235 ± 0.014	19.7	143.14 ± 8.58	182.13 ± 50.09	182.25 ± 22.50	214.80 ± 10.80
	403.047	12498	0.159 ± 0.010	19.7	96.71 ± 5.80	71.88 ± 5.25	71.84 ± 10.23	82.80 ± 4.80
	405.995	18872	0.240 ± 0.014	19.7	146.04 ± 8.75	153.11 ± 11.18	118.60 ± 15.65	123.60 ± 7.20
	422.025	7901	0.100 ± 0.008	19.7	61.14 ± 5.03	126.75 ± 9.25	60.38 ± 8.77	60.00 ± 3.60
	430.777	10663	0.135 ± 0.011	19.7	82.51 ± 6.79	41.05 ± 4.64	43.27 ± 6.71	43.56 ± 3.24
	545.580	6763	0.086 ± 0.007	19.7	52.33 ± 4.31	8.58 ± 2.36	38.52 ± 5.64	40.80 ± 3.60
	590.986	1868	0.024 ± 0.002	19.7	14.45 ± 1.19	24.43 ± 2.76	26.55 ± 4.10	
	649.558	372	0.005 ± 0.001	19.7	2.88 ± 0.73		10.62 ± 2.65	
	680.398	1105	0.014 ± 0.001	19.7	8.55 ± 0.70		37.47 ± 6.62	
	701.426	149	0.002 ± 0.000	19.7	1.15 ± 0.29	1.22 ± 0.33	6.44 ± 2.37	
	701.776	32	0.000 ± 0.000	19.7	0.25 ± 0.06			
	714.197	0	0.000 ± 0.000	19.7			13.19 ± 3.48	
	788.661	0		0.000	19.7			
27816.793	396.221	11137	0.323 ± 0.027	55.8	92.54 ± 7.62	106.26 ± 7.76	120.23 ± 7.29	113.60 ± 6.40
	439.801	4866	0.141 ± 0.012	55.8	40.44 ± 3.33	8.46 ± 0.62	8.47 ± 1.08	
	457.931	13147	0.381 ± 0.023	55.8	109.24 ± 6.55	119.30 ± 8.71	104.43 ± 6.83	104.00 ± 6.40
	501.167	3451	0.100 ± 0.008	55.8	28.68 ± 2.36	31.49 ± 3.56	34.10 ± 2.99	27.36 ± 2.24
	532.503	580	0.017 ± 0.004	55.8	4.82 ± 1.22	5.56 ± 1.53	9.46 ± 1.54	6.24 ± 0.96
	571.934	1326	0.038 ± 0.003	55.8	11.02 ± 0.91	15.67 ± 1.77	10.04 ± 1.92	

Upper Energy Level (cm^{-1})	Transition λ (nm)	Intensity (a.u.)	Branching Fraction	Lifetime (ns)	This work's g_kA_{ki} (10^6 s^{-1}) Value	Ryder g_kA_{ki} (10^6 s^{-1}) Value [7]	Li et al. g_kA_{ki} (10^6 s^{-1}) Value [16]	Hartog et al. g_kA_{ki} (10^6 s^{-1}) Value [14]
27993.254	413.255	13003	0.291 ± 0.017	60.6	86.32 ± 5.17	81.98 ± 5.98	23.70 ± 3.68	31.68 ± 2.70
	436.414	9686	0.216 ± 0.018	60.6	64.30 ± 5.29	64.26 ± 4.69	50.70 ± 7.61	56.34 ± 3.42
	454.260	18971	0.424 ± 0.025	60.6	125.93 ± 7.55	130.91 ± 9.56	162.25 ± 22.06	171.00 ± 9.00
	531.004	1919	0.043 ± 0.004	60.6	12.74 ± 1.05	12.87 ± 1.45	25.22 ± 3.97	24.66 ± 2.16
	561.692	608	0.014 ± 0.003	60.6	4.03 ± 1.02	2.33 ± 0.64	10.36 ± 2.01	
	602.205	340	0.008 ± 0.002	60.6	2.26 ± 0.57	3.79 ± 1.04	10.43 ± 2.31	
	643.603	219	0.005 ± 0.001	60.6	1.45 ± 0.37	0.88 ± 0.24	14.38 ± 3.24	
28418.965	406.108	59627	0.360 ± 0.022	7.15	905.94 ± 54.30	1091.14 ± 79.65	1188.97 ± 54.84	1440.00 ± 72.00
	428.451	41544	0.251 ± 0.015	7.15	631.19 ± 37.83	541.03 ± 39.50	259.13 ± 20.56	246.60 ± 18.00
	445.639	22798	0.138 ± 0.008	7.15	346.38 ± 20.76	332.89 ± 24.30	216.29 ± 17.71	187.20 ± 14.40
	486.481	2147	0.013 ± 0.001	7.15	32.62 ± 2.69	26.67 ± 3.01	54.91 ± 7.57	25.56 ± 2.34
	519.261	24830	0.150 ± 0.009	7.15	377.25 ± 22.61	337.19 ± 24.61	455.45 ± 33.36	457.20 ± 37.80
	548.570	12214	0.074 ± 0.004	7.15	185.57 ± 11.12	160.96 ± 11.75	244.33 ± 20.76	169.20 ± 18.00
	586.503	2316	0.014 ± 0.001	7.15	35.18 ± 2.90	24.03 ± 2.72	98.39 ± 13.88	
	626.433	220	0.001 ± 0.000	7.15	3.34 ± 0.85	3.57 ± 0.98		
28856.898	380.534	56173	0.387 ± 0.023	12.4	499.56 ± 29.94	469.63 ± 34.28	312.05 ± 32.89	248.00 ± 14.40
	399.010	37989	0.262 ± 0.016	12.4	337.85 ± 20.25	368.22 ± 26.88	525.95 ± 50.02	571.20 ± 30.40
	410.656	13150	0.091 ± 0.005	12.4	116.95 ± 7.01	94.46 ± 6.90	42.13 ± 6.41	35.20 ± 2.08
	420.558	18791	0.130 ± 0.008	12.4	167.11 ± 10.02	185.23 ± 13.52	139.09 ± 15.86	105.60 ± 6.40
	437.106	2484	0.017 ± 0.001	12.4	22.09 ± 1.82	15.83 ± 1.79	17.21 ± 4.84	
	476.330	0	0.000 ± 0.000	12.4			13.04 ± 5.44	10.24 ± 1.28
	478.180	0	0.000 ± 0.000	12.4		0.81 ± 0.22		
	479.550	417	0.003 ± 0.001	12.4	3.70 ± 0.94	4.20 ± 1.16		
	535.697	8240	0.057 ± 0.005	12.4	73.28 ± 6.03	78.21 ± 5.71	155.07 ± 18.27	120.00 ± 11.20
	571.812	6689	0.046 ± 0.004	12.4	59.48 ± 4.90	62.51 ± 4.56	85.78 ± 12.60	81.60 ± 8.00
	642.578	1157	0.008 ± 0.001	12.4	10.29 ± 0.85	11.23 ± 1.27		31.36 ± 4.32
29027.543	396.311	26081	0.292 ± 0.017	12.3	426.85 ± 25.59	558.02 ± 40.74	588.74 ± 35.92	716.40 ± 36.00
	417.560	12178	0.136 ± 0.008	12.3	199.31 ± 11.95	187.62 ± 13.70	187.45 ± 15.35	219.60 ± 12.60
	433.869	29317	0.328 ± 0.020	12.3	479.81 ± 28.76	468.44 ± 34.20	234.49 ± 18.68	288.00 ± 18.00
	472.489	2611	0.029 ± 0.002	12.3	42.74 ± 3.52		14.44 ± 3.34	
	503.351	6087	0.068 ± 0.006	12.3	99.63 ± 8.20	99.22 ± 7.24	92.65 ± 8.71	88.20 ± 7.20
	530.843	2919	0.033 ± 0.003	12.3	47.78 ± 3.93	30.83 ± 3.48	31.83 ± 5.00	
	566.886	6923	0.077 ± 0.006	12.3	113.31 ± 9.33	73.78 ± 8.34	103.87 ± 10.28	100.80 ± 9.00

Upper Energy Level (cm^{-1})	Transition λ (nm)	Intensity (a.u.)	Branching Fraction	Lifetime (ns)	This work's g_kA_{ki} (10^6 s^{-1}) Value	Ryder g_kA_{ki} (10^6 s^{-1}) Value [7]	Li et al. g_kA_{ki} (10^6 s^{-1}) Value [16]	Hartog et al. g_kA_{ki} (10^6 s^{-1}) Value [14]
	603.423	2676	0.030 ± 0.002	12.3	43.80 ± 3.61	34.84 ± 3.94	79.52 ± 9.98	
	678.896	12	0.000 ± 0.000	12.3	0.19 ± 0.05		5.13 ± 4.29	
	687.305	384	0.004 ± 0.001	12.3	6.28 ± 1.59	6.99 ± 1.92	15.58 ± 10.87	
	752.900	227	0.003 ± 0.001	12.3	3.71 ± 0.94	3.68 ± 1.01	33.92 ± 20.24	45.00 ± 7.20
	805.127	0	0.000 ± 0.000	12.3				

Table 6.2 Radiative parameters for Nd II. Lifetimes adopted from Pincuic et al. [11].

Upper Energy Level (cm-1)	Transition λ (nm)	Intensity (a.u.)	Branching Fraction	Lifetime (ns)	This work's g_kA_{ki} (10^6 s^{-1}) Value	Ryder g_kA_{ki} (10^6 s^{-1}) Value [7]
18883.700	462.499	0	0.000 ± 0.000			
	492.757	8795	0.968 ± 0.080			
	528.676	291	0.032 ± 0.008			
24003.200	462.499	1011	0.121 ± 0.031			
	492.757	5661	0.679 ± 0.056			
	528.676	1663	0.200 ± 0.016			
28745.300	347.783	1131	0.077 ± 0.006	170	4.08 ± 0.46	3.5 ± 0.86
	362.117	13552	0.923 ± 0.055	170	48.86 ± 4.77	49.4 ± 5.97
32832.600	328.367	8941	0.556 ± 0.046	87	95.87 ± 10.81	
	343.335	622	0.039 ± 0.010	87	6.67 ± 1.77	
	360.397	6516	0.405 ± 0.033	87	69.87 ± 7.88	

Table 6.3 Radiative parameters for Nd III. Lifetimes adopted from Zhang et al. [17].

References

[1] Corliss, C. H., & Bozman, W. R. (1962). Experimental transition probabilities for spectral lines of seventy elements; derived from the NBS Tables of spectral-line intensities. *NBS Monograph, Washington: US Department of Commerce, National Bureau of Standards.*

[2] Penkin, N. P. and Komarovskii, V. A. (1973). Relative values oscillator strengths of Nd I spectral lines, *Optics and Spectroscopy, 35,* 4-8.

[3] Marek, J., & Stahnke, H. J. (1980). Radiative lifetimes of optical levels of neutral erbium, gadolinium and neodymium. *Zeitschrift für Physik A Atoms and Nuclei*, *298*(2), 81-82.

[4] Gorshkov, V. N., Komarovskii, V. A., Osherovich, A. L., & Penkin, N. P. (1982). Lifetimes of excited levels of Nd I and Nd II. Oscillator strengths of the spectral lines of Nd I. *Astrophysics*, *17*(4), 437-441.

[5] Biémont, E., Quinet, P., Svanberg, S., & Xu, H. L. (2004). Experimental lifetime determination in neutral praseodymium (Pr I) and neodymium (Nd I). *Journal of Physics B: Atomic, Molecular and Optical Physics*, *37*(7), 1381.

[6] Den Hartog, E. A., Fittante, A. J., & Lawler, J. E. (2011). Radiative lifetimes of neutral neodymium. *Journal of Physics B: Atomic, Molecular and Optical Physics*, *44*(22), 225001.

[7] Ryder, C. A. (2012). Oscillator strength measurements in singly-ionized, doubly-ionized, and neutral lanthanides and transition elements (Sm, Nd, Pr, Gd, Cu, and Fe) using laser-induced breakdown.

[8] Maier, R. S., & Whaling, W. (1977). Transition probabilities in Nd (II) and the solar neodymium abundance. *Journal of Quantitative Spectroscopy and Radiative Transfer*, *18*(5), 501-507.

[9] Andersen, T., Poulsen, O., Ramanujam, P. S., & Petkov, A. P. (1975). Lifetimes of some excited states in the rare earths: La II, Ce II, Pr II, ND II, Sm II, Yb I, Yb II, and Lu II. *Solar Physics*, *44*(2), 257-267.

[10] Ward, L., Vogel, O., Arnesen, A., Hallin, R., & Wännström, A. (1985). Accurate experimental lifetimes of excited levels in Nd II. *Physica Scripta*, *31*(3), 161.

[11] Pinciuc, C. M., Rivest, R. C., Izawa, M. R., Holt, R. A., Rosner, S. D., & Scholl, T. J. (2001). Measurement of radiative lifetimes in Nd II. *Canadian Journal of Physics*, *79*(9), 1159-1167.

[12] Scholl, T. J., Holt, R. A., Masterman, D., Rivest, R. C., Rosner, S. D., & Sharikova, A. (2002). Measurement of radiative lifetimes in Pr II and Nd II. *Canadian journal of physics*, *80*(7), 713-722.

[13] Xu, H. L., Svanberg, S., Cowan, R. D., Lefebvre, P. H., Quinet, P., & Biémont, E. (2003). Theoretical and experimental lifetime and oscillator strength determination in singly ionized neodymium (Nd ii). *Monthly Notices of the Royal Astronomical Society*, *346*(2), 433-440.

[14] Den Hartog, E. A., Lawler, J. E., Sneden, C., & Cowan, J. J. (2003). Improved laboratory transition probabilities for Nd II and application to the neodymium abundances of the Sun and three metal-poor stars. *The Astrophysical Journal Supplement Series*, *148*(2), 543.

[15] Biémont, É., Ellmann, A., Lundin, P., Mannervik, S., Norlin, L. O., Palmeri, P., ... & Schef, P. (2007). Decay of metastable states in Nd II. *The European Physical Journal D-Atomic, Molecular, Optical and Plasma Physics*, *41*(2), 211-219.

[16] Li, R., Rehse, S. J., Scholl, T. J., Sharikova, A., Chatelain, R., Holt, R. A., & Rosner, S. D. (2007). Fast-ion-beam laser-induced-fluorescence measurements of branching fractions and oscillator strengths in Nd II. *Canadian Journal of Physics*, *85*(12), 1343-1379.

[17] Zhang, Z., Svanberg, S., Palmeri, P., Quinet, P., & Biémont, E. (2002). Measurement of lifetimes by laser-induced fluorescence and determination of transition probabilities of astrophysical interest in NdIII. *Astronomy & Astrophysics*, *385*(2), 724-732.

[18] Kurucz, R. L. & Bell, B. (1995). *Atomic Line Data. Kurucz CD-ROM No. 23.* Cambridge, Mass.: Smithsonian Astrophysical Observatory.

CHAPTER 7: Laser-Induced Breakdown Spectroscopy – Laser-Induced Fluorescence for Atomic Measurements

Laser-induced breakdown spectroscopy – laser-induced fluorescence (LIBS-LIF) is a hyphenated technique that uses a high-energy laser as a source for a laser-induced plasma and a second resonant excitation laser to specifically populate an upper energy level of an atom or ion in the plasma. LIBS-LIF is typically used for trace element detection in samples such as trace metal in biospecimens [1-4]. The resonant excitation laser, in our case an OPO (discussed in Chapter 3), is tuned to a specific wavelength of a transition from an upper energy level of interest. At a desired time after plasma formation (interpulse delay) the resonant excitation laser is incident on the plasma. Assuming there is a non-zero population in the lower energy level of the transition (which there is in a thermally populated distribution), the upper energy level is resonantly excited (pumped) which then increases the population of atoms in the upper energy level. This increases the spontaneous emission on all transitions exiting the energy level. Increasing the emission will result in larger observed emission lines in our spectra that may be brought above the background and noise levels. This is advantageous when the limiting factor in trace elemental detection is a small signal that is below the noise and/or background.

Fluorescence, emitted light due to absorbed light, is observed in tens of nanoseconds after resonant excitation of an upper energy level. This is very different from LIBS where emission is observed over microseconds after formation of the plasma as discussed in Chapter 2. In order to observe an increase in emission the observation time of the plasma needs to be accurate and precise so that it immediately follows the resonant excitation pulse.

We have proposed LIBS-LIF as a technique to alleviate problem energy levels with blended and small emission lines. When emission lines are blended and/or small, branching fractions cannot be calculated due to some transitions from the upper energy level being unmeasurable. Using LIBS-LIF on problem energy levels, emission from one of the blended lines can be increased so that the blending of lines

becomes insignificant. This makes the emission line measurable. The increased emission from an upper energy level will also result in bringing small emission lines above the noise. This technique will be used to make new emission line measurements possible and increase the accuracy of the measurements by increasing the SNR and SBR on all transitions from an upper energy level of interest.

This chapter will discuss the implementation of a LIBS-LIF experiment for use in our atomic measurement apparatus.

7.1 Implementation and Results

In our LIBS-LIF experiment we used a tuneable OPO laser for resonant excitation of the plasma and the same Nd:YAG laser firing at its fundamental frequency that was used for the LIBS measurements for production of the plasma (for more information on the experimental apparatus see Section 3.4).

The 23229.991 cm^{-1} upper energy level in singly-ionized neodymium was selected for investigation in our LIBS-LIF implementation experiments. This upper energy level was chosen since it is a well-characterized level with good-accuracy data for comparison [5]. The transitions in this upper energy level were advantageous since all were in the tuneable range of our OPO laser allowing us to pump on any of the transitions exiting the upper energy level. Any upper energy level could be chosen as long as it contained at least one transition in our OPO laser's wavelength range so that it could be resonantly excited. Initial proof-of-concept experiments used the transition from the 23229.991 cm^{-1} upper energy level ending in the ground level for singly-ionized neodymium (Figure 7.1) as the pumping transition. This transition wavelength was 430.357 nm. Because we do not have a calibrated wavemeter, the OPO wavelength was matched to the transition using our Échelle spectrometer by overlaying spectra that contained the Nd II 430.357 nm emission line and only the OPO pulse. The OPO wavelength was adjusted until the OPO pulse spectrally overlapped the Nd II emission line (Figure 7.2). This Nd II upper energy level was a good choice due to its strong and weak transitions allowing a wide range of results to be observed.

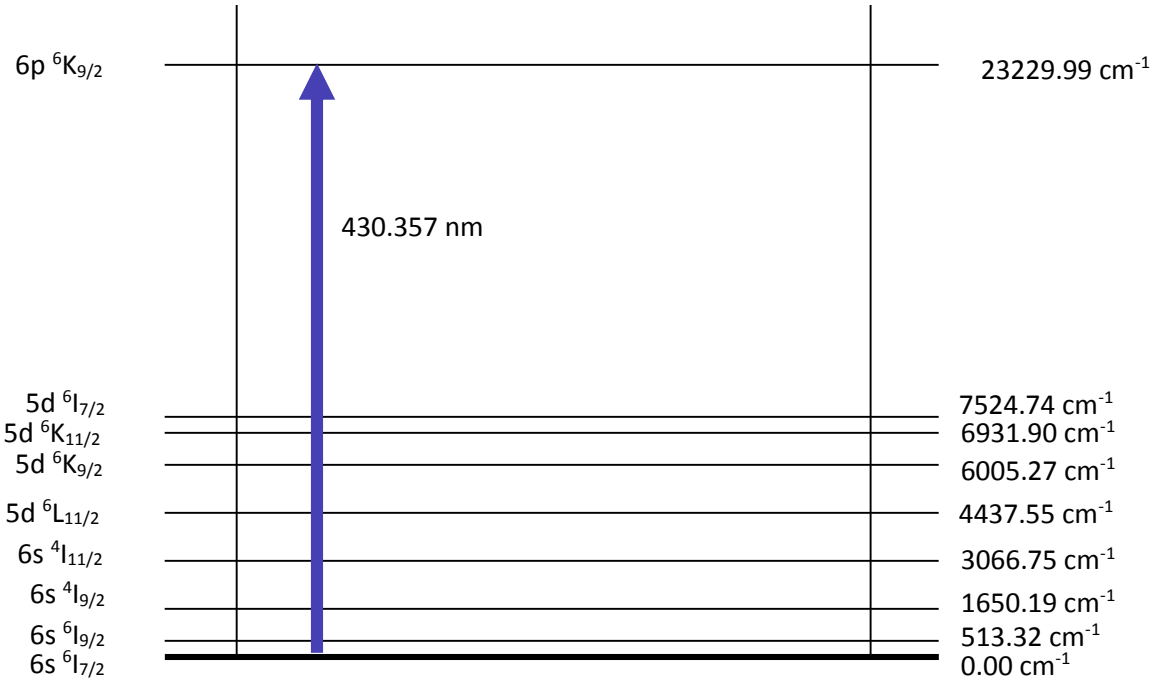

Figure 7.1 Singly-ionized neodymium energy level diagram showing the eight lower energy levels which have allowed spontaneous emission transitions from the 6p $^6K_{9/2}$ upper energy level at 23229.99 cm^{-1}. The transition from the ground state, 0.00 cm^{-1}, was used for initial pumping experiments (430.357 nm).

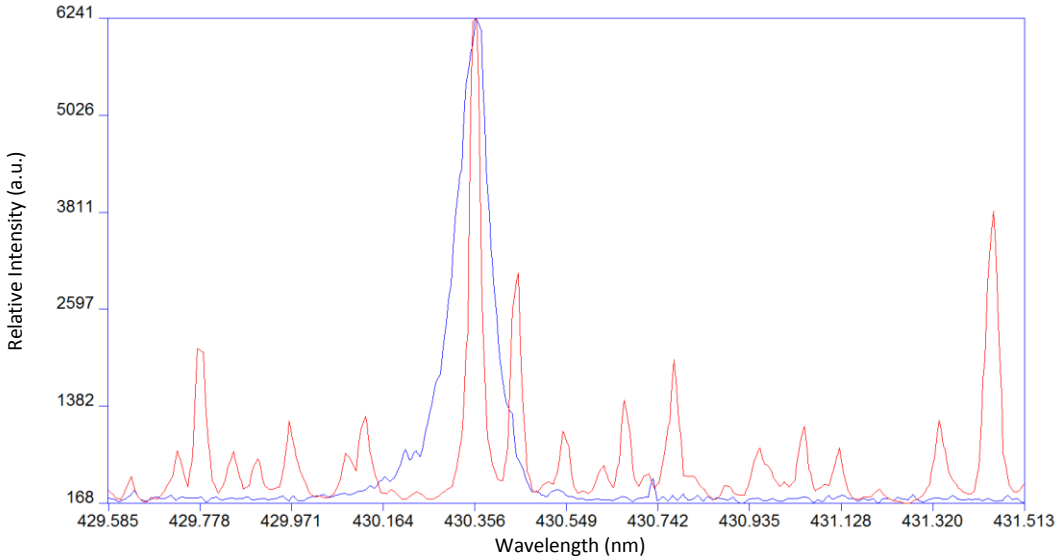

Figure 7.2 A LIBS emission spectrum of Nd optimized for singly-ionized species (red) with a second overlapped spectrum of the OPO pulse tuned to the 430.357 nm transition in Nd II with no LIBS spectrum (blue). The blue spectrum was obtained by positioning the spectrometer observation window at the time of the OPO pulse and capturing reflected/scattered OPO light off the Nd target in the vacuum chamber.

The timing for the LIBS-LIF experiment was different than the regular LIBS spectra. Because LIF only lasts for tens of nanoseconds after the excitation by the 5 ns OPO pulse, the plasma observation window needed to be extremely short (nanoseconds) in order to observe an effective increase in emission above normal. The normal longer observation time was microseconds. The increase in emission that was observed with LIF when the normal microseconds-long window was used was negligible in comparison to the normal observation time LIBS spectrum. As expected though, the increase in emission was substantial when the timing window was optimized to only observe a range when LIF was occurring, which thus minimized the normal LIBS plasma emission. With the extremely short observation time MCP amplification was increased drastically over the normal LIBS spectrum due to the drastic decrease in total photons captured. Specific results will be shown in following sections.

Various OPO beam diameters were explored for LIBS-LIF. Resonant excitation, and thus fluorescence, was not observed when the OPO excitation laser beam size was less than half a millimetre in diameter. At this beam size the energy fluence of the OPO beam was sufficient to cause breakdown. Instead of a resonant excitation pulse it was a secondary breakdown pulse. The size of the OPO beam needed to be on the order of the plasma size (at the current pulse energy), which was a few millimetres in diameter in order to not cause a secondary breakdown. It is common for investigators to intentionally create a secondary breakdown pulse in the initial plasma in a technique known as dual-pulse LIBS [1]. This dual-pulse LIBS was not the intent of our current investigation. For optimal coupling of photons from the resonant excitation pulse into the plasma the resonant excitation pulse should be approximately the size of the plasma, increasing the overlap with the plasma. This allows excitation of more atoms in the plasma. With a larger beam size, resonant excitation was observed in the plasma as shown by increased emission on transitions exiting the upper energy level. The OPO beam size was optimized with the defocusing lens as shown in Figure 3.10 to be as close to the size of the plasma as possible, which was 1 by 3 mm. All other parameters were preliminary in the aforementioned studies for the implementation of the LIBS-LIF setup.

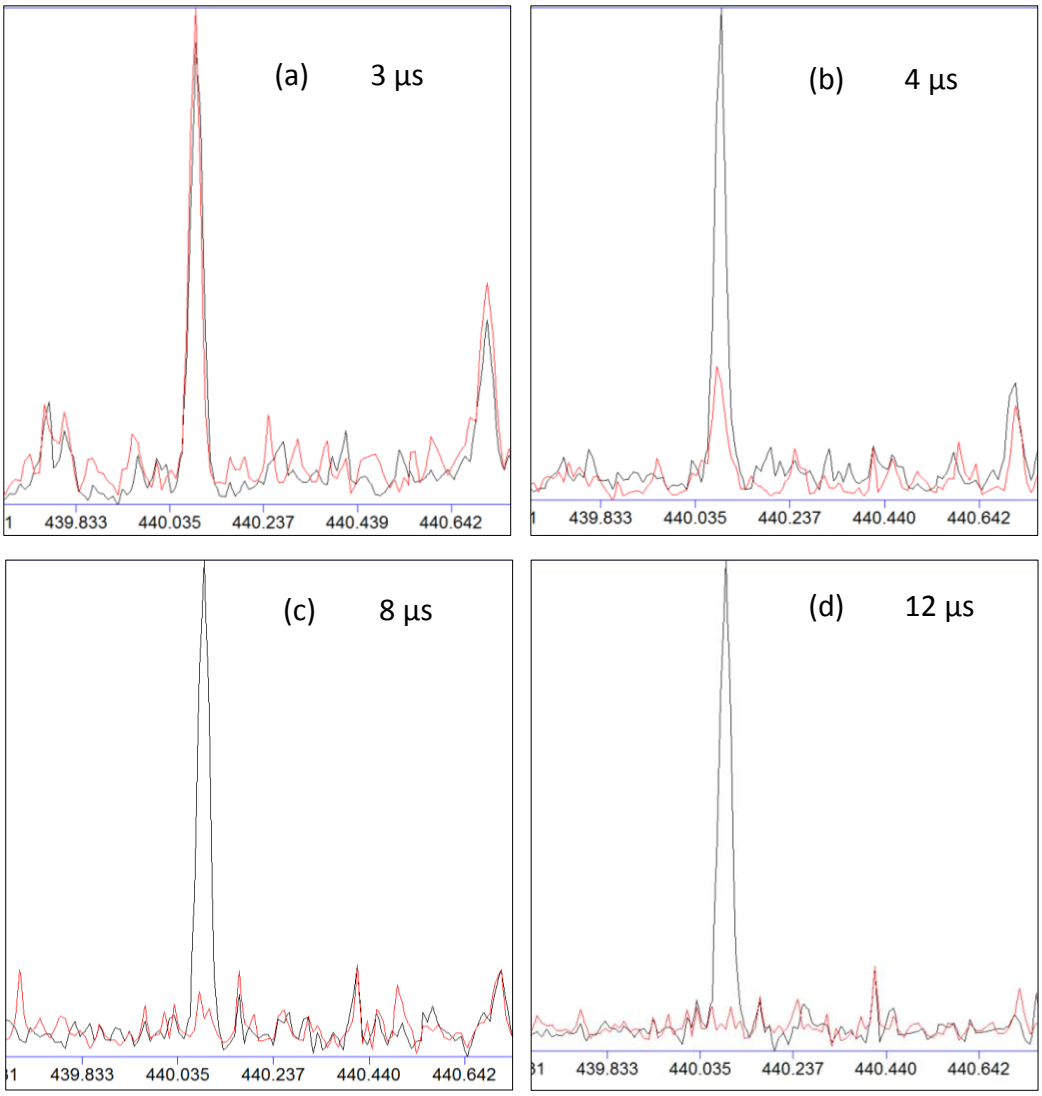

Figure 7.3 LIBS-LIF at various interpulse delay times showing an increase in LIF in comparison to normal LIBS emission at longer delay times after plasma formation (and thus longer interpulse delay times). (a) LIBS (red) and LIBS-LIF (black) spectra showing no noticeable increase in emission with LIF at a 3 µs interpulse delay. (b) LIBS (red) and LIBS-LIF (black) spectra showing noticeable increase in emission with LIF but still substantial normal LIBS emission at a 4 µs interpulse delay. (c) LIBS (red) and LIBS-LIF (black) spectra showing great increase in emission with LIF with near no normal LIBS emission at an 8 µs interpulse delay. (d) LIBS (red) and LIBS-LIF (black) spectra showing tremendous increase in emission with LIF with no normal LIBS emission at a 12 µs interpulse delay. In all spectra, the resonant laser wavelength was 430.357 nm, which is not shown in this spectral range. The y-axis is intensity in arbitrary units and the x-axis is wavelength in nanometres.

As mentioned in Section 4.1, fluorescence takes place over tens of nanoseconds. The ESAWIN spectrometer imaging system had a response of approximately 60 ns that made it impossible to separate the LIF observation and OPO pulse in time and only capture fluorescence without the pumping pulse. The activation and deactivation of the image intensifier was not precise enough for the nanosecond timing required and thus less-than-desirable results were achieved due to the OPO pulse observation in every LIF spectrum. From this I concluded that the LLA ESA spectrometer imaging system did not have the nanosecond response that is required for optimal LIBS-LIF measurements, since the plasma has to be observed nanoseconds after the resonant excitation pulse. When investigating the timing for observation, fluorescence was only ever observed when the OPO was also observed, which was a result of the response of the imaging system. Our (new) secondary spectrometer, an LTB Aryelle, did have nanosecond response and was able to separate the OPO pulse and the LIF in time. This showed great promise for use in our LIBS-LIF setup but due to the fact that the new spectrometer was not fully implemented in the laboratory it could not be used for the LIBS-LIF preliminary studies.

Using the delay generator, various interpulse delays were explored to determine when the emission from the resonantly excited upper energy level was maximized. This was done by pumping the 23229.991 cm^{-1} level with an OPO wavelength of 430.357 nm (Figure 7.1) and then observing LIF on the different decay branches ranging from 440 nm (transition from the 23229.991 cm^{-1} to 513.32 cm^{-1} energy level) to 636 nm (transition from the 23229.991 cm^{-1} to 7524.74 cm^{-1} energy level). In this way, the presence of the OPO pulse in the ESA spectrometer gate window did not affect the measurement. With an argon pressure of 1 Torr, fluorescence diminished at interpulse times shorter than 4 microseconds in comparison to background (normal) LIBS emission over the same observation time. Using an interpulse delay of 4 microseconds fluorescence was observed and increased at interpulse delay times longer than 4 microseconds (Figure 7.3). With an interpulse delay of 12 microseconds nearly all background LIBS emission was gone and the only observed peaks were from the resonantly pumped upper energy level. A

comparison between nominal LIBS emission for Nd II (delay time and observation time of 1 microsecond) and LIBS-LIF with interpulse delay of 12 microseconds is seen in Figure 7.4. This technique showed great promise for eliminating shouldered/blended peaks as seen in Figure 7.4 where all of the LIBS Nd emission has decreased to be unobservable except for transitions originating in the pumped upper energy level. The optimal interpulse delay was not completely determined as other parameters currently still need to be explored in these preliminary implementation studies.

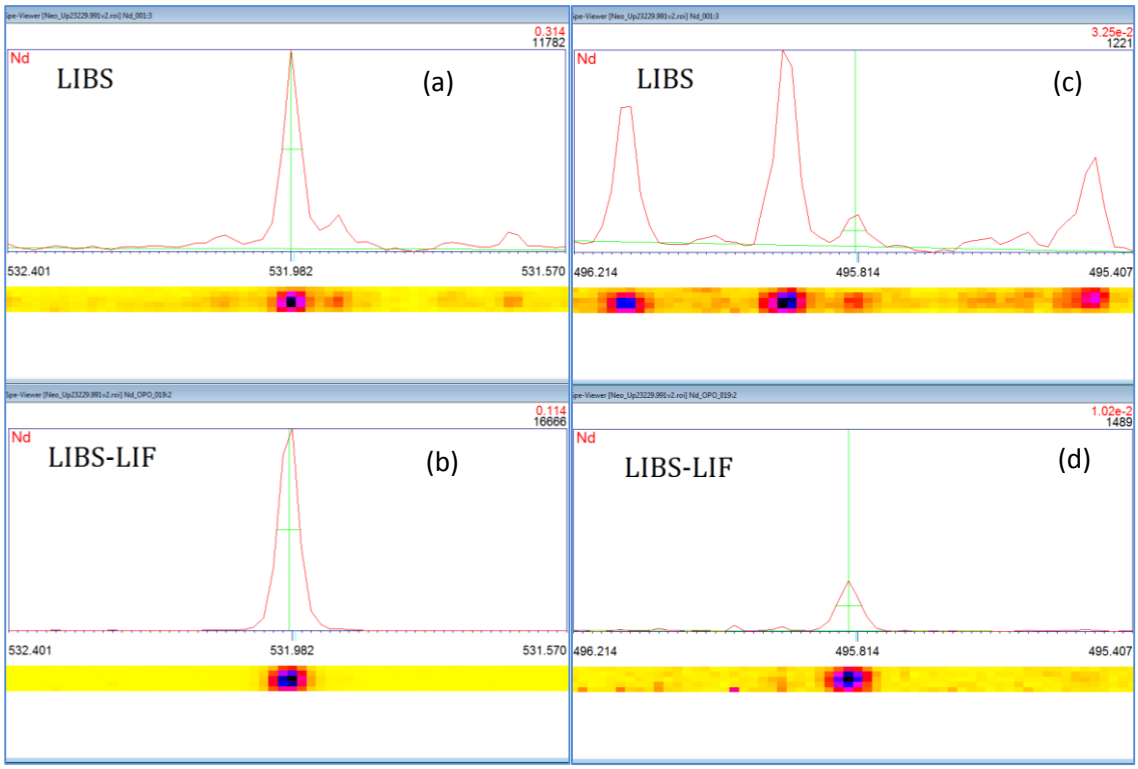

Figure 7.4 Comparison between a nominal LIBS spectrum optimized for Nd II and a LIBS-LIF spectrum with a 12 μs interpulse delay pumping the upper energy level 23229.991 cm^{-1} in Nd II. (a) and (b)show the fluorescence on the 531.982 nm branch. (c) and (d) show the fluorescence on the much smaller 495.82 nm branch. (b) and (d) both show a noticeable decrease in all other non-pumped Nd emission and thus the only peaks observed originate in the energy level of interest. The slight shoulder to the 531.982 nm peak in (a) is gone in (b) using LIBS-LIF and the interpulse delay of 12 μs. The y-axis is intensity in arbitrary units and the x-axis is wavelength in nanometres.

Various OPO laser energies were explored, from nanojoules to hundreds of microjoules. With the current alignment and spectrometer response no increase in emission was observed using nanojoules of energy with a beam size of a few millimetres. Increase in emission was observed using microjoules and above. Emission from the upper energy level increased with up to hundreds of microjoules per OPO pulse (Figure 7.5). The energy could not be increased above this due to current limitations with the response of the LLA ESA spectrometer, which led to saturation of the imaging system. Specifically, this unavoidable saturation occurred because of the inability to select a short observation window immediately after the OPO pulse. Thus, scattered photons from the incident OPO pulse were also observed in the LIF spectrum and were much greater than emission from the plasma. The OPO pulse energy could not be increased above a few microjoules without increasing this image saturation, which is detrimental to the imaging camera. It is hoped that this will be addressed in future work.

LIF emission enhancement was compared when different transitions were used to pump the upper energy level. The lower the energy level of the transition to be pumped the larger the increase in LIF emission observed when all other parameters were kept constant (50 μJ/pulse), as expected (Figure 7.6). The largest increase in LIF emission was observed when pumping from the lowest energy level, the ground state in singly-ionized neodymium. The smallest increase was observed when pumping the transitions from the higher energy levels (Figure 7.6). Various other resonant excitation laser / ablation laser geometries (e.g. perpendicular beam or “side-pumping”) were not explored in this study.

7.2 Conclusions and Future Work

Using both the LLA ESA and LTB Aryelle spectrometers enhancement of signal was observed on transitions from a pumped upper energy level, thus proving that I was indeed resonantly exciting a specific energy level within the laser-induced plasma. Optical pumping of the level was also demonstrated on multiple transitions, although most efficient excitation was observed when utilizing the strongest transition (which had a ground state as its lower energy level), as expected. The ESA

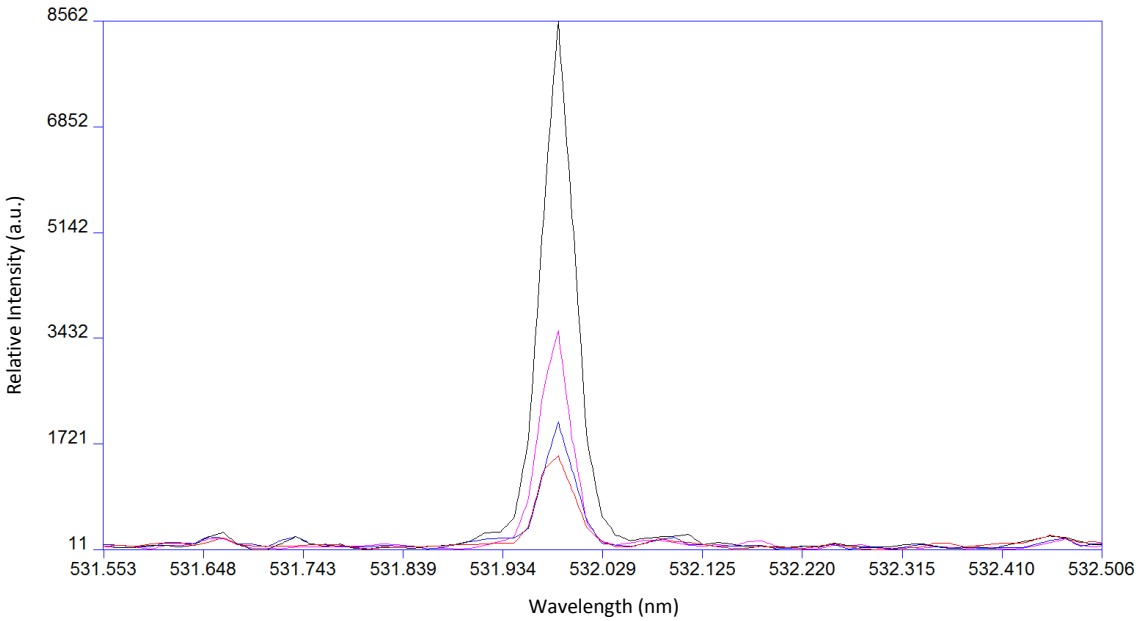

Figure 7.5 LIBS-LIF at various OPO laser pulse energies. The 23229.991 cm^{-1} level was resonantly pumped at 430.357 nm while fluorescence was observed on the 531.982 line. The smallest peak (red) was excited with 100 nJ/pulse. An increase in LIF was observed with increasing power up to the largest increase in LIF at 0.5 mJ/pulse (black). The OPO pulse was saturating the detector system at 0.5 mJ/pulse and thus I was not able to increase the energy further.

spectrometer possessed a few problematic timing limitations that could be overcome with use of the Aryelle spectrometer. The LIBS-LIF experimental apparatus and geometry was designed, setup, and preliminary timing/control tests showed great promise for future LIBS-LIF experiments such as the enhancement of trace-metal signals in biospecimens (which is of particular interest to our group.) Future students will be continuing with LIBS-LIF work to optimize the interpulse delay (delay between ablation and resonant excitation pulses) as well as optimal laser energy for increase in emission from specific transitions in targets of interest since these parameters are expected to change for different transitions and for different elements.

Even given the current limitations with the spectrometer system, enhancement of the smaller emission lines brought them sufficiently above noise levels to make measurements possible, as well eliminated emission line blends (Figure 7.5) by eliminating all other Nd LIBS emission and reducing the background

noise with a longer interpulse delay time. However, the main drawback of the LIBS-LIF technique as implemented here was the plasma observation time. LIBS-LIF observation was nanoseconds in length to observe LIF enhancement, but then the total emission (including florescence) was comparable to our normal LIBS spectra seen in Chapter 4 and thus small emission lines did not greatly increase in intensity. Further studies will be conducted to investigate the technique for measurement of blended emission lines as well as the possibility of new measurements of smaller emission lines with the LTB Aryelle spectrometer.

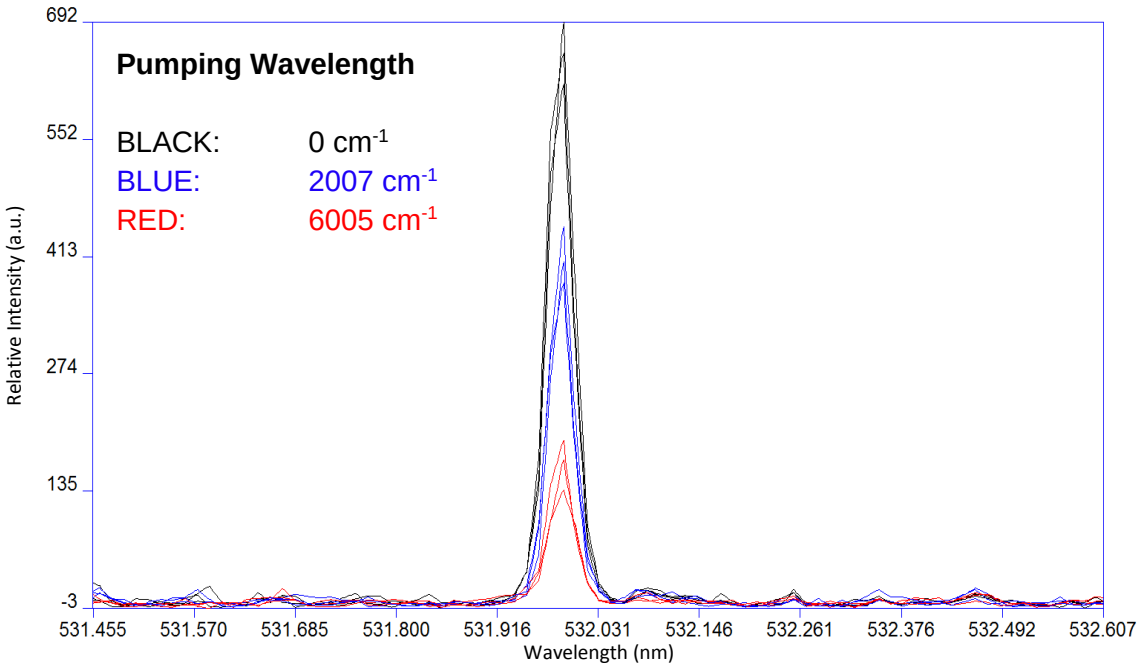

Figure 7.6 LIF comparison when pumping on various transitions to populate the upper energy level of 23229.991 cm^{-1} in singly-ionized neodymium. The largest increase was observed when pumping the transition from the ground state in singly ionized neodymium (0 cm^{-1}, black spectra). Smaller increases were observed when pumping the transitions from the higher energy levels such as the 2007 cm^{-1} energy level (blue spectra) and 6005 cm^{-1} energy level (red spectra). All pumping was done using the same energy of 50 μJ/pulse.

References

[1] Singh, J. P., & Thakur, S. N. (Eds.). (2007). *Laser-induced breakdown spectroscopy*. Elsevier.

[2] Miziolek, A. W., Palleschi, V., & Schechter, I. (Eds.). (2006). *Laser-induced breakdown spectroscopy (LIBS)* (pp. 127-136). Cambridge: Cambridge University Press.

[3] Cremers, D. A., Yueh, F. Y., Singh, J. P., & Zhang, H. (2006). *Laser-Induced Breakdown Spectroscopy, Elemental Analysis*. John Wiley & Sons, Ltd.

[4] Radziemski, L. J., & Cremers, D. A. (1989). Laser-induced plasmas and applications.

[5] Ryder, C. A. (2012). Oscillator strength measurements in singly-ionized, doubly-ionized, and neutral lanthanides and transition elements (Sm, Nd, Pr, Gd, Cu, and Fe) using laser-induced breakdown.

CHAPTER 8: Conclusion

8.1 Conclusion

The goal of this work was to improve the experimental apparatus for atomic measurements utilizing laser-induced breakdown spectroscopy, improve the accuracy of current measurements in the lanthanide system of elements, and make new measurements if the improvements were substantial enough to allow them. The new components designed and implemented in the experimental apparatus substantially increased light collection from the plasma. This resulted in improved accuracy in the atomic measurements from Nd II and observation of previously unobservable emission lines in Nd I and Nd III. A careful experimental parameter optimization increased the accuracy of our measurements and allowed the measurement of more upper energy levels by tailoring the experiment for specific ionization states. This resulted in new transition probability measurements in neutral and doubly-ionized neodymium (reported in Chapter 6) and reduced the uncertainties on all measurements.

8.2 Future Work

During the course of this work, emission spectra were optimized and recorded for three other lanthanides: Gd, Sm, and Pr. This data was recorded but has not yet been analyzed. Due to the high spectral line density as discussed in Chapter 4 careful analysis and examination of the data must be performed. This data will be analyzed and examined by a future student to produce newer improved results on these lanthanides. It is expected that the overall improvement of these results will be near identical to that of the neodymium results reported in this thesis. That is to say, there will be new measurements reported for the neutral and doubly-ionized species with an overall increase in accuracy of the transition probabilities.

As a result of this work, a LIBS radiative lifetime experiment is also ready for a future student to begin making lifetime measurements, most likely on gallium, as discussed in Chapter 1. This experimental apparatus was implemented, tested, and documented for a future student. The experiment is not currently operational, but is

ready to be reassembled and for measurements to begin. In obtaining radiative lifetime measurements using LIBS, the measurements could be combined with our branching fraction measurements so that previously determined radiative lifetimes do not need to be used to obtain transition probabilities.

LIBS-LIF has been demonstrated using a new pulsed OPO laser system and has shown great promise in its ability to improve accuracy and alleviate problems associated with our typical LIBS atomic measurements as discussed in Chapter 7. This two-laser method will continue to be explored and optimized for making new measurements. This was the first implementation of the LIBS-LIF system in our laboratory and the experience gained in developing this system will also be applied to other LIBS projects that are ongoing in our laboratory.

APPENDICES

Appendix A MATLAB Code

A.1 Dat File Data to Excel File

The following code is a MATLAB script that takes the .dat files I saved with our ESAWIN software and places the integrated areas under each peak and corresponding wavelength into an Excel file in the same folder that contained the .dat files. This resulted in an Excel file for each upper energy level under investigation containing the pertinent information for my branching fraction calculations.

```
tic
format long g;


NumDatFiles = input('how many .dat files are stored in each EUp to be
analyzed into final_data?: ' );


ElementSymbl = input('what element is it? input answer as the element
symbol (Iron = Fe): ','s');


 [filenameEUps,pathnameEUps]= uigetfile({'*.txt','Text files (*.txt)';
'*.dat', 'Data files (*.dat)'; '*.*','All Files (*.*)'},'select the
file with the list of Upper Energies to input.. Ex: Nd II EUps.txt');
fileLocationEUps = strcat(pathnameEUps,filenameEUps);
fidEUps = fopen(fileLocationEUps);
EUpsList = textscan(fidEUps,'%s'); fclose(fidEUps);
EUpsList = EUpsList{:};
EUpsListNum = str2double(EUpsList);


disp('got to 34')

count = 0;
filenameHeaders = [];
filenameExcl = [];

clear ii
for ii = 1:(length(EUpsList))
    count = count + 1
```

```
    if ii==1

        [filenameDat,pathnameDat]= uigetfile({'*.dat','Data files
(*.dat)'; '*.*','All Files (*.*)'},'select the 1st .dat file from the
1st EUp Ex: 042711_001.dat');
        fileLocationDat = strcat(pathnameDat,filenameDat);
        pathnameDat2 = pathnameDat;

    else

        AA=length(EUpsList{ii});
        pathnameDatBegin = pathnameDat2(1:(end-10));
        EUpIndx = char(EUpsList{ii});
        pathnameDat = strcat(pathnameDatBegin, EUpIndx, '\')

    end



clear jj;
    for jj = 1:NumDatFiles



        if ((jj>0) && (jj <= 9))
            filenameDatStart = filenameDat(1:end-5);
            filenameDatStart = char(filenameDatStart);
            Ending = int2str(jj);
            Ending2 = char(Ending);
            filenameDatStartIter = [filenameDatStart, Ending2];
            FileNameEnd = strcat(filenameDatStartIter  ,'.dat');
            fileLocationDat = strcat(pathnameDat,FileNameEnd);
        elseif ((jj>9) && (jj <=99))
            filenameDatStart = filenameDat(1:end-6);
            filenameDatStart = char(filenameDatStart);
            Ending = int2str(jj);
            Ending2 = char(Ending);
            filenameDatStartIter = [filenameDatStart, Ending2];
            FileNameEnd = strcat(filenameDatStartIter  ,'.dat');
            fileLocationDat = strcat(pathnameDat,FileNameEnd);
        elseif ((jj>99) && (jj<=999))
            filenameDatStart = filenameDat(1:end-7);
            filenameDatStart = char(filenameDatStart);
            Ending = int2str(jj);
            Ending2 = char(Ending);
            filenameDatStartIter = [filenameDatStart, Ending2];
            FileNameEnd = strcat(filenameDatStartIter  ,'.dat');
            fileLocationDat = strcat(pathnameDat,FileNameEnd);
        else
            disp('counter of jj is too large')
            error('counter of jj is too large');

        end
```

```
disp('got to 119')
        fidDat = fopen(fileLocationDat);
        EUpsListDat1 = textscan(fidDat,'%s');
        fclose(fidDat);
        EUpsListDat2 = EUpsListDat1{:};
        EUpsListDatNum = str2double(EUpsListDat2);
        disp('got to 125')
        ElementSymbl = char(ElementSymbl);
        EUpsListDat2(strcmpi(EUpsListDat2,ElementSymbl));
        ElemSymblCellLocatnRow =
find(strcmpi(EUpsListDat2,ElementSymbl));
        EUpsListDatCells = EUpsListDatNum(ElemSymblCellLocatnRow + 2);
        EUpsListDatCells(isnan(EUpsListDatCells)) = 0;
        disp('got to 131')
        if jj==1
            finalDataMatrix =
zeros(length(EUpsListDatCells),NumDatFiles);
        end

        finalDataMatrix(:,jj) = EUpsListDatCells;

    end
disp('got to 139')

    finalDataMatrixT = finalDataMatrix';


    disp('got to 148')
    SizefinalDataMatrixT= size(finalDataMatrixT);
    SumfinalDataMatrixT = sum(finalDataMatrixT);
    for uu=1:SizefinalDataMatrixT(2)
        if SumfinalDataMatrixT(1,uu) == 0

            finalDataMatrixT(1,uu) = 1;
            disp('Appended column of zeros in finalDataMatrixT to a
single cell with a 1 in the empty column ')
        end

    end

    pathnameExcl = char(pathnameDat);
    OutPutFileExclName = strcat(pathnameExcl, 'Final_Data.xls')
    xlswrite(OutPutFileExclName, finalDataMatrixT, 'Sorted Data' ,
'A1');
disp('got to 165')
    disp('1 round completed')

    clear finalDataMatrix
    clear finalDataMatrixT
    clear EUpsListDat1
    clear SumfinalDataMatrixT
end
toc
```

A.2 Apply Spectral Calibration to Data

The following code is a MATLAB script that takes each Excel file produced by the script in Appendix A.1 and applies the spectral correction factor, as described in Chapter 5, to each intensity (integrated area under the curve) value. A new Excel file is saved with the applied spectral correction factor in the same folder location.

```
tic
format long g;


disp('Input spec corr list')
[filenameFValues,pathnameFValues]= uigetfile('*.xls')
infile = strcat(pathnameFValues,filenameFValues);
[FValuesDataIn,FValuesTextIn] = xlsread(infile);
FValuesDataIn(isnan(FValuesDataIn)) = 0;
RowsByColsFValue = size(FValuesDataIn);

disp('Get .txt with column of all EUps')
[filenameEUps,pathnameEUps]= uigetfile({'*.txt','Text files (*.txt)';
'*.dat', 'Data files (*.dat)'; '*.*','All Files (*.*)'});
fileLocationEUps = strcat(pathnameEUps,filenameEUps);
fidEUps = fopen(fileLocationEUps);
EUpsList = textscan(fidEUps,'%s');
fclose(fidEUps);
EUpsList = EUpsList{:}; EUpsListNum = str2double(EUpsList);


ElementAbbrv = input('What element is it? (Abbreviate it with symbol
like Sm for Samarium): ', 's');

count = 0;
filenameHeaders = [];
filenameExcl = [];

for i = 1:(length(EUpsList))
    count = count + 1

    filenameHeaders = char(filenameHeaders);
    if isempty(filenameHeaders)

        [filenameHeaders,pathnameHeaders]= uigetfile({'*.roi','Roi
files (*.roi)'; '*.txt','Text files (*.txt)'; '*.dat', 'Data files
(*.dat)'; '*.*','All Files (*.*)'},'select the header file to input -
needs to be a ROI file);
        fileLocationHeaders = strcat(pathnameHeaders,filenameHeaders);

    elseif isequal(filenameHeaders(end-3:end),'.roi')

        filenameHeaders = strcat(EUpsList(i), '.roi');
        ElementAbbrv = char(ElementAbbrv);
```

```
        ElementAbbrv2 = strcat(ElementAbbrv,'_');
        filelocationh = strcat(pathnameHeaders, ElementAbbrv2);
        fileLocationHeaders = strcat(filelocationh,filenameHeaders);

    else

        [filenameHeaders,pathnameHeaders]= uigetfile({'*.roi','Roi
files (*.roi)'; '*.txt','Text files (*.txt)'; '*.dat', 'Data files
(*.dat)'; '*.*','All Files (*.*)'},'select the header file to input -
needs to be a ROI');
        fileLocationHeaders = strcat(pathnameHeaders,filenameHeaders);
    end

    fileLocationHeaders = char(fileLocationHeaders);

    fid = fopen(fileLocationHeaders);

    allstrings = textscan(fid,'%s');
    fclose(fid);

    allstrings = allstrings{:};
    if isempty(filenameExcl)
        disp('Input excel file "Final Data"')
        [filenameExcl,pathnameExcl]= uigetfile({'*.xls','Excel files
(*.xls)'; '*.xlsx', 'Excel_07 files (*.xlsx)'; '*.*','All Files
(*.*)'});
        FileLocationExcl = strcat(pathnameExcl,filenameExcl);

    else

        filenameExcl = char(EUpsList(i));
        pathnameExclFirstPart = pathnameExcl(1:(end-15));
        pathnameExclFirstPart=char(pathnameExclFirstPart);
        pathnameExcl =
strcat(pathnameExclFirstPart,ElementAbbrv2,'Up',EUpsList(i),'\');
        FileLocationExcl = strcat(pathnameExcl,'Final_Data.xls');
        FileLocationExcl = char(FileLocationExcl);

    end

    FileLocationExcl = char(FileLocationExcl);
    ExcelInFile = xlsread(FileLocationExcl , 'Sorted Data');

    ExcelInFile(isnan(ExcelInFile)) = 0;


    filenameHeaders = char(filenameHeaders);
    if isequal((filenameHeaders((end-3):end)),'.dat')

        allNum = str2double(allstrings);
        wavelengths1 = find((0<allNum) & (allNum < 1));
        Wavelengths = allNum((0<allNum)&(allNum<1));
        Wavelengths = 1000*Wavelengths';

    elseif isequal(filenameHeaders(end-3:end),'.roi')
```

```
        allNum = str2double(allstrings);
        wavelengths1 = find((100.000<allNum) & (allNum < 999.999));


        for aa=length(wavelengths1):-1:1
            if
~isequal(ElementAbbrv,char(allstrings(wavelengths1(aa,:)-1)))

                wavelengths1(aa,:)='';
            end

        end


        Wavelengths = allNum(wavelengths1);
        Wavelengths = Wavelengths';


    else
        disp('first file type isnt consistent with program
requirements')
        error('first file type isnt consistent with program
requirements')
    end



    ElemIndex = wavelengths1 - 1;
    for j = 1:(length(ElemIndex))
        ElementSymbols(j) = allstrings(ElemIndex(j));
    end
    ElementSymbols;


    RowByCol = size(ExcelInFile);
    if (RowByCol(2)>length(ElementSymbols)) &&
(RowByCol(2)>length(Wavelengths))
        disp('the excel file "Final Data" matrix has more columns than
the headers')
        for jj = 1:(RowByCol(2) - length(ElementSymbols))
            ElementSymbols = [NaN(1,jj) ElementSymbols];
            Wavelengths = [zeros(1,jj), Wavelengths];
        end
    elseif (RowByCol(2)<length(ElementSymbols)) &&
(RowByCol(2)<length(Wavelengths))
        disp('the excel file "Final Data" matrix has less columns than
the           headers')
        for kk = 1:(length(ElementSymbols) - RowByCol(2))
            ExcelInFile = [zeros(RowByCol(1),kk) , ExcelInFile];
        end
    else

    end


    RowsByColsData = size(ExcelInFile);
    RowsByColsWavelengths = size(Wavelengths);
```

```
    Diff(RowsByColsFValue(1),RowsByColsWavelengths(2)) = 0;

    for mm = 1:RowsByColsWavelengths(2)

        for nn=1:RowsByColsFValue(1)
              Diff(nn,mm) = abs(FValuesDataIn(nn,1) -
Wavelengths(1,mm));

        end

    end

    [C,Indices] = min(Diff);

    MultiplyFactor = FValuesDataIn(Indices,2)';
    SizeMultiplyFactor = size(MultiplyFactor);
    EUpDataInFValue(RowsByColsData(1),RowsByColsData(2)) = 0;


    if SizeMultiplyFactor(2) == RowsByColsWavelengths(2)
        for rr = 1:RowsByColsData(1)
            for cc = 1:RowsByColsData(2)
                EUpDataInFValue(rr,cc) =
ExcelInFile(rr,cc)*MultiplyFactor(1,cc);
            end
        end
    else
        disp('size of MultiplyFactor line 229 and size of Wavelengths
arent equal')
        error('size of MultiplyFactor line 229 and size of Wavelengths
arent equal');
    end

    clear rr
    clear cc

    pathnameExcl = char(pathnameExcl);
    OutPutFileExclName = strcat(pathnameExcl, pathnameExcl((end -
14):(end -                                        1)), '.xls')
    xlswrite(OutPutFileExclName, ElementSymbols, 'sheet1' , 'A1');
    xlswrite(OutPutFileExclName, Wavelengths, 'sheet1' , 'A2');
    xlswrite(OutPutFileExclName, ExcelInFile, 'sheet1' , 'A3');

    xlswrite(OutPutFileExclName, MultiplyFactor, 'WithFValue' , 'A1');
    xlswrite(OutPutFileExclName, ElementSymbols, 'WithFValue' , 'A2');
    xlswrite(OutPutFileExclName, Wavelengths, 'WithFValue' , 'A3');
    xlswrite(OutPutFileExclName, EUpDataInFValue, 'WithFValue' , 'A4');


    clear wavelengths1
    clear Wavelengths
    clear ElementSymbols
    clear MultiplyFactor
    clear EUpTextIn
    clear EUpDataInFValue
    clear Diff
    clear EUpDataInFValueAvg
```

```
    clear EUpDataInFValueStdV
    clear EUpDataInFValueFracStdV
    clear EUpDataInFValueP4
    clear EUpDataInFValueP6
    clear EUpDataInFValueP7_85
    clear EUpDataInFValueP8_3
    clear EUpDataInFValueP8_83


end
toc
```

VITA AUCTORIS

NAME:	Russell Allan Putnam
PLACE OF BIRTH:	Windsor, Ontario
YEAR OF BIRTH:	1991
EDUCATION:	B.Sc. [Honours] Physics and High Technology with Co-op, 2013 University of Windsor, Windsor, Ontario
	M.Sc. Physics, 2014 University of Windsor, Windsor, Ontario